Nanocomposites as Thermoelectric Materials

By

Qing Hao

M.S., Mechanical Engineering (2004)
University of Texas at Austin

B.E., Thermal Engineering (2001)
Tsinghua University, Beijing, China

Submitted to the Department of Mechanical Engineering
in Partial Fulfillment of the Requirements for the Degree of
Doctor of Philosophy in Mechanical Engineering

at the
Massachusetts Institute of Technology
June 2010

Signature of Author.....
Department of Mechanical Engineering
May 22, 2010

Certified by.....
Gang Chen
Carl Richard Soderberg Professor of Power Engineering
Thesis Supervisor

Accepted by.....
David E. Hardt
Chairman, Department Committee on Graduate Students

Nanocomposites as Thermoelectric Materials

by

Qing Hao

Submitted to the Department of Mechanical Engineering on May 22, 2010
in Partial Fulfillment of the Requirements for the Degree of
Doctor of Philosophy in Mechanical Engineering

ABSTRACT

Thermoelectric materials have attractive applications in electric power generation and solid-state cooling. The performance of a thermoelectric device depends on the dimensionless figure of merit (ZT) of the material, defined as $ZT = S^2\sigma T / k$, where S is the Seebeck coefficient, σ is the electrical conductivity, k is the thermal conductivity, and T is the absolute temperature.

In recent years, the idea of using nanotechnology to further improve the figure of merit of conventional thermoelectric materials has triggered active research and led to many exciting results. Most of the reported ZT enhancements are based on thin films and nanowires in which the thermal conductivity reduction plays a central role. We pursue the nanocomposite approach as an alternative to superlattices in the quest for high ZT materials. These nanocomposites are essentially nano-grained bulk materials that are synthesized by hot pressing nanoparticles into a bulk form. The interfaces inside a nanocomposite strongly scatter phonons but only slightly affect the charge carrier transport. Therefore, we can significantly reduce the lattice thermal conductivity and even somewhat increase the power factor $S^2\sigma$, resulting in higher ZT than for bulk materials. Compared with expensive thin-film superlattices, nanocomposites will have significant advantages in mass production, device construction and operation.

This thesis covers my studies on bismuth antimony telluride nanocomposites and some recent work on Co_4Sb_{12}-based nanocomposites. In bismuth antimony telluride nanocomposites, we have achieved a peak ZT of 1.4 at 100 °C, a 40% increase in ZT over the bulk material. This is the first significant ZT increase in this material system in fifty years. The same approach has also yielded a peak ZT around 1.2 in Yb filled Co_4Sb_{12} nanocomposites. During the process, great efforts were dedicated to assuring accurate and dependable property measurements of thermoelectric nanocomposites. In addition to comparing measurement results between the commercial setups and a home-built measurement system, the high ZT obtained in bismuth antimony telluride nanocomposites was further confirmed by a device cooling test.

To better understand the measured thermoelectric properties of nanocomposites, theoretical analysis based on the Boltzmann transport equation was performed. Furthermore, frequency-dependent Monte Carlo simulations of the phonon transport were conducted on 2D periodic porous silicon and 3D silicon nanocomposites. In the thermoelectrics field, the latter one provided the first accurate prediction for phonon size effects in a given nanocomposite. For charge carriers in thermoelectric nanocomposites,

their transport can be significantly affected by the interfacial electronic states. To address this, impedance measurements were conducted on nanocomposites to determine the electronic barrier height at the grain interfaces, which is critical for the detailed theoretical analysis of the interfacial charge transport and energy conversion processes. Although large amount of work has been done using this technique to understand the defect states and the barrier height on the grain boundaries of polycrystalline silicon or oxides, this method has not been applied to thermoelectric materials. Along another line, a simple bandgap measurement technique with nanopowders was developed based on the Fourier Transform Infrared Spectroscopy. This provided a convenient way to quickly check the bandgaps of various thermoelectric nanocomposites, which is also crucial for theoretical studies.

Thesis Supervisor: Gang Chen
Title: Carl Richard Soderberg Professor of Power Engineering

Acknowledgements

The process of writing this thesis provided me an opportunity to revisit many of the exciting moments of my Ph.D. studies. During my stay at MIT, I feel deeply grateful for many people who have taught and inspired me in their own ways. Among these, I would first thank my advisor, Prof. Gang Chen, who not only set an example of conducting first-class research but also helped me to improve myself in many aspects. In addition, I highly appreciate the enthusiastic help and support of my other Ph.D. committee members, including Prof. Mildred S. Dresselhaus, Prof. Zhifeng Ren, and Prof. Borivoje B. Mikic. I benefited a lot from their constructive criticisms of my research and encouragement along the way. With this chance, I would acknowledge the support and guidance of my Master's advisor, Prof. Li Shi at the University of Texas at Austin, who led me into the nanotechnology field from a traditional thermal engineering background. I am also indebted to Prof. Yinping Zhang at Tsinghua University for his advice over the years.

Over the past six years, I was fortunate to work with many brilliant and diligent students and visiting scholars in both Boston College and MIT. Among many ex- and current MIT/BC members, I would especially thank the follows for their friendship and many useful discussions: Mr. Austin Minnich, Dr. Taofang Zeng, Dr. Bed Poudel, Dr. Yi Ma, Mr. Andrew Muto, Dr. Shuo Chen, Dr. Bhaskaran Muralidharan, Dr. Yucheng Lan, Dr. Mona Zebarjadi, Mr. Jian Yang, Mr. Bo Yu, Mr. Xiao Yan, Ms. Xiaoting Jia, Mr. Daniel Kraemer, Prof. Qinyu He, Mr. Gaohua Zhu, Dr. Céline Nathalie Hin, Dr. Dezhi Wang, Prof. Daryoosh Vashaee, Dr. Xiaoyuan Chen, Dr. Xiaowei Wang, Ms. Yanjia Zuo, Mr. Yi He, Prof. Aaron Schmidt, Prof. Ronggui Yang, Dr. Lu Hu, Prof. Arvind Narayanaswamy, Prof. Chris Dames, Prof. Hohyun Lee, Dr. Sheng Shen, Dr. Weitao Dai, Dr. Tony Feng, Mr. Sangyeop Lee, Dr. Jae Sik Jin, Prof. Ruiting Zheng, Mr. Jinwei Gao, Mr. Poetro Sambegoro, Ms. Kimberlee Collins, Ms. Maria Luckyanova, Mr. Kenneth McEnaney, Ms. Zhiting Tian, Dr. Anastassios Mavrokefalos, Dr. Nitin Shukla, Dr. Nuo Yang, Mr. Yiqun Zhang, Ms. Christine Junior, Prof. Huanxin Chen, Dr. Ming-Shan Jeng, Prof. Dongsheng Zhu, Prof. Jinbo Wang, Prof. Ase Henry, Mr. Jivtesh Garg, Mr. Jack Ma, Dr. Min Gao, and all others. I thank Dr. Gregory McMahon at Boston College and Dr. Yumeng Shi from Prof. Jing Kong's group for their help in measurements.

I would also thank Boris Kozinsky and Daehyun Wee at the Bosch Research and Technology Center, and members in Prof. Nicola Marzari's group who collaborated with me in the Bosch-MIT project. I am grateful for the financial support from DOE, NSF, NASA, Robert Bosch LLC, Intel Corporation, and Toyota Corporation.

Finally, I thank the continuous support and encouragement from my parents, my elder sister, and my long-term friends, including Bill Qu, Yi Lu, Yuan Shen, Wener Lv, Xiaogeng Song, Xiaochuan Yang, Enying Zheng, and many others.

Table of Contents

Abstract 3
Acknowledgements 5
Table of Contents 7
List of Figures 11
List of Tables 14

Chapter 1. Introduction 15
1.1 Introduction to Thermoelectrics 15
1.2 Thermoelectric Nanocomposites 16
1.3 Fundamental Studies of TE Nanocomposites 17
1.4 The Scope and Organization of this Thesis....19
1.5 References 20

Chapter 2. Material Synthesis, Characterization, and Device Cooling Test 23
2.1 Brief Review of Thermoelectric Nanocomposite 23
2.2 Material Synthesis....24
2.3 Material Characterization....28
2.3.1 Review of Thermoelectric Property Measurements 28
2.3.2 Home-Built Measurement System 31
Thermal Diffusivity Measurements 33
Electrical Conductivity Measurements....35
Seebeck Coefficient Measurements 37
2.3.3 Commercial Measurement Systems 37
2.4 High-ZT Nanocomposites 38
2.4.1 P-Type Bismuth Antimony Telluride Nanocomposites 39
Nanopowder Preparation by High Energy Ball Milling 39
Thermoelectric Properties of BiSbTe Nanocomposites 41
Structure Studies of BiSbTe Nanocomposites 45
2.4.2 Co_4Sb_{12}-Based Nanocomposites 47
$Yb_xCo_4Sb_{12}$ Nanopowder and Hot-Pressed Nanocomposites....48
Thermoelectric Properties of $Yb_xCo_4Sb_{12}$ Nanocomposites....49
2.5 Device Cooling Test 52
2.5.1 Principle of the Cooling Test 52
2.5.2 Experimental Setup 53
2.5.3 Temperature Profile Calculation 55
2.5.4 Thermoelectric Compatibility 56
2.5.5 Cooling Test Results and Discussion 58
2.6 Annealing Effects on ZT of BiSbTe nanocomposites 61
2.7 Conclusions 63
2.8 References 64

Chapter 3. Theoretical Analysis Based on the Boltzmann Transport Equation 67
3.1 Boltzmann Transport Equation under the Relaxation Time Approximation ..67
3.2 Macroscopic Electrical Properties 68
3.2.1 Expressions of Different Electrical Properties 69
Effective Mass of Charge Carriers.....69
Expressions for the Electrical Properties 71
Multi-band Calculations 71
3.2.2 Scattering Mechanisms of Charge Carriers 73
Acoustic Deformation Potential Scattering 74
Ionized Impurity Scattering.....75
Polar Optical Phonon Scattering 76
3.3 Macroscopic Lattice Thermal Conductivity 76
3.3.1 Callaway's Model.....76
3.3.2 Scattering Mechanisms of Phonons 78
Phonon-Phonon Scattering 78
Electron-Phonon Scattering 79
Point-Defect Scattering 80
Grain Boundary Scattering.....81
3.4 Results and Discussions.....82
3.4.1 BiSbTe Nanocomposites.....82
3.4.2 Bulk $CoSb_3$ Analysis.....85
3.5 Conclusions.....89
3.6 References.....90

Chapter 4. Frequency-Dependent Monte Carlo Simulations of Phonon Transport and ZT Predictions of Nano-Grained Bulk Silicon 93
4.1 Introduction 93
4.2 Basic Simulation Procedure 94
4.3 Phonon Scattering Treatment 99
4.3.1 Internal Scattering Treatment 100
4.3.2 Interface Scattering Treatment 103
4.4 Boundary Condition 103
4.4.1 Cold Wall Emission 105
4.4.2 Hot Wall Emission 106
4.4.3 Periodic Heat Flux with a Constant Virtual Wall Temperature Boundary Condition 107
4.5 Results and Discussion 107
4.5.1 Employed Models for Different Scattering Mechanisms 108
4.5.2 Calibration for Bulk Silicon 110
4.5.3 Two-Dimensional Porous Silicon with Aligned Pores 112
4.5.4 Silicon Nanocomposites 117
4.6 Transient Phonon Monte Carlo Simulations 123
4.7 Summary 127
4.8 References 129

Chapter 5. Measurements on Grain Interface Barrier Height and Nanopowder Bandgap 132
5.1 Interface Studies of Nanograin Boundaries using Novel Capacitance Technique 132
5.1.1 Concept of Interface Capacitance Measurement 133
5.1.2 Interface Admittance Model 135
5.1.3 Measurements on Bulk Samples 138
5.1.4 Data Analysis with the Brick Layer Model 140
5.2 Nanopowder Bandgap Measurement 142
5.3 References.....147

Chapter 6. Future Research Directions 150
6.1 Annealing Effects on ZT of PbTe nanocomposites 150
6.2 N-type Bi_2Te_3-Based Nanocomposites 151
6.3 Nanocomposites for Low Temperature Applications 152
6.4 Single Grain Interface Impedance Measurements 152
6.5 Electrostatic Force Spectroscopy 155
6.6 Other Recommended Research Directions 156
6.7 References 158

List of Figures

Figure 1.1 Two basic operation modes of a TE device 16

Figure 2.1 Seebeck coefficients as a function of Te percentage for selected Bi_2Te_3 nanocomposites, with nanoparticles prepared by wet chemistry..... 25
Figure 2.2 Temperature-dependent Seebeck coefficient of Sample "Bi_2Te_3 050406 with H_2 reduction" in Fig. 2.1 26
Figure 2.3 Plasma Pressure Compaction (P^2C) hot press setup 27
Figure 2.4 Furnace heating hot press setup 28
Figure 2.5 ZT of various TiO_x samples 29
Figure 2.6 Hot pressed disk-shaped samples and bars diced along the in-plane direction of disks 32
Figure 2.7 Experimental setup of temperature-dependent property measurements 32
Figure 2.8 Photo of the real experiment setup 33
Figure 2.9 Temperature variations of two separated points along a bar sample 34
Figure 2.10 XRD (A), SEM (B), low- (C) and high- (D) magnification TEM images of an as-ball-milled nanopowder from ingots 40
Figure 2.11 (A) XRD pattern of the nanopowders after ball milling, (B) SEM, (C) bright-field TEM image, and (D) HRTEM image of the mechanically alloyed nanopowders from elements 40
Figure 2.12 Thermal diffusivities in the disk axial direction (measured by the laser flash setup) and disk-plane direction (by my home-built system) 41
Figure 2.13 Comparison of thermoelectric properties of a SOA ingot, nanocomposites from commercial ingots and element chunks 43, 44
Figure 2.14 The thermal conductivity of BiSbTe nanocomposites from ingots 45
Figure 2.15 TEM images showing the microstructures of a BiSbTe nanocomposite from ingots 46
Figure 2.16 SEM images at (a) low- and (b) high-magnification and TEM images at (c) low- and (d) high-magnification of P^2C hot pressed skutterudite $Yb_{0.35}Co_4Sb_{12}$ bulk samples, showing the high crystallinity, clean grain boundaries, and larger angle grain boundary 49
Figure 2.17 Room temperature carrier concentration and Hall mobility of $Yb_xCo_4Sb_{12}$ bulk samples with x = 0.3, 0.35, 0.4, and 0.5 50
Figure 2.18 Temperature-dependent electrical conductivity (a), Seebeck coefficient (b), thermal conductivity (c), and ZT (d) of DC hot pressed skutterudite $Yb_xCo_4Sb_{12}$ bulk samples with x = 0.3, 0.35, 0.4, 0.5, and 1.0 51
Figure 2.19 Experimental setup of the device cooling test 54
Figure 2.20 Reduced efficiency as a function of $u = J / k\nabla T$ 58
Figure 2.21 Cooling test results with the hot side fixed at 100 °C for a unicouple using a nanocomposite p leg and a commercial n leg 59
Figure 2.22 Thermoelectric properties of the commercial n leg 60
Figure 2.23 Comparison of ΔT_{max} of two unicouples with hot-side temperatures set at 50°, 100°, and 150 °C 60

Figure 2.24 Properties of a $Bi_{0.4}Sb_{1.6}Te_3$ nanocomposite sample before and after 250 °C annealing under an Ar flow 62
Figure 2.25 Phase diagram of the $Bi_{0.25}Sb_{0.75}Te$ composition 62

Figure 3.1 Phonon traveling distance between grain interfaces inside a spherical grain..81
Figure 3.2 Fitting results of the SOA ingot and the BiSbTe nanocomposite from ingots: (A) electrical conductivity, (B) Seebeck coefficient, (C) thermal conductivity, (D) ZT...83
Figure 3.3 Theoretical fitting of S, σ, k and ZT for a Te-doped single-crystal $CoSb_3$ sample in Ref. 48 of Chap. 3 87
Figure 3.4 Seebeck coefficients predicted for bandgaps different from E_g = 0.24 eV used in Fig. 3.3A 87
Figure 3.5 Band structure of $CoSb_3$, computed by our collaborators at the Bosch Research and Technology Center (unpublished) 89

Figure 4.1 Calibration of the reset methods for scattered phonons 102
Figure 4.2 Distribution functions on the domain boundaries described by the periodic heat flux boundary condition 104
Figure 4.3 The time history of subcell temperatures for a pure silicon computational domain 111
Figure 4.4 a) Structure of the simulated porous silicon film. b) Top view of the film, with details of the computational domain 113
Figure 4.5 (a) Normalized temperature contour for a 200 nm period. (b) Temperature distribution along the x direction for typical y locations 115
Figure 4.6 Normalized in-plane lattice thermal conductivities of porous silicon films as a function of period size 116
Figure 4.7 Lattice thermal conductivities of pure silicon, measured silicon nanocomposite, calculated heavily doped bulk silicon with electron concentration fixed at $n = 3.93\times10^{20}$ cm^{-3}, and phonon-impurity scattering coefficient $A = 1.0\times10^{-43}$ s^3, and simulated 200-nm-grain-size nanocomposite with the same n, A values 119
Figure 4.8 Room-temperature accumulated thermal conductivity of heavily doped bulk silicon, with electron concentration fixed at $n = 3.93\times10^{20}$ cm^{-3}, and phonon-impurity scattering coefficient $A = 1.0\times10^{-43}$ s^3 120
Figure 4.9 Grain size dependence of room-temperature lattice thermal conductivities for silicon nanocomposites with $n = 3.93\times10^{20}$ cm^{-3}, $A = 1.0\times10^{-43}$ s^3 121
Figure 4.10 (a) Predicted thermal conductivities of a silicon nanocomposite with 10 nm grain sizes. (b) Power factors predicted by the model developed in Ref. 52 of Chap. 4. (c) Predicted thermoelectric figure of merit (ZT) for above two cases and corresponding heavily doped bulk silicon 122
Figure 4.11 Simulated temperature decay at location x=0.....125
Figure 4.12 Temperature profile evolution of the simulation domain.....126

Figure 5.1 Energy-band diagram and charge distribution at a grain boundary 134
Figure 5.2 (A) Energy-band diagram and (B) charge distribution on a grain interface..137
Figure 5.3 A) Real and imaginary parts of the measured impedance Z with a primitive shielding provided by thin copper pieces. The improved experimental setup is drawn in the inset. B) The ratio between the real and imaginary parts of Z 139

Figure 5.4 Equivalent circuit of a grain in the brick layer model 141
Figure 5.5 Fitting the ratio between the imaginary and real parts of the measured impedance Z.....142
Figure 5.6 Transmissivity of a typical single-crystal KBr slice, compared with that for a cold pressed KBr disc.....145
Figure 5.7 A) Transmissivity of a KBr slice with/without nanopowders. B) Ratio between KBr transmissivity with/without nanopowders in Fig. 5.7A 145
Figure 5.8 Absorption coefficient of bulk Si 146
Figure 5.9 Absorption pattern extracted for PbTe nanopowder 147

Figure 6.1 Property change of a typical PbSe nanocomposite during high-temperature measurements 150
Figure 6.2 Schematic diagram of a traveling voltage probe setup to measure the capacitance and resistance across a single grain interface.....154
Figure 6.3 An SEM image of the real setup 154
Figure 6.4 A) Four-probe electrical measurements under a SEM. B) Two tungsten probes loaded onto a sample under a SEM.....155
Figure 6.5 Concept of the Electrostatic Force Spectroscopy (EFS) measurement 156

List of Tables

Table 3.1 Dielectric constants for bulk Sb_2Te_3 and Bi_2Te_3 84
Table 3.2 Major parameters used in analyzing both the SOA ingot and the BiSbTe nanocomposites.....84
Table 3.3 Parameters used in analyzing the Te-doped single-crystal $CoSb_3$ sample in Ref. 48 of Chap. 3.....88

Table 4.1 Parameters used for silicon nanocomposites 118

Table 5.1 Parameters used for p-type PbTe.....141
Table 5.2 Parameters determined by the theoretical fitting in Fig. 5.5.....142

Chapter 1. Introduction

To meet emerging energy challenges, significant contributions can be made by revolutionary technologies that can effectively harvest waste heat, which accounts for roughly two-thirds of the total consumed energy in the modern era [1]. Solid-state thermoelectric (TE) devices can be potentially utilized for large-scale waste heat recovery, with attractive features such as absence of moving parts, high reliability, and environmental friendliness [2-4]. Currently, TE power generators have been developed to potentially produce electricity from the waste heat in car exhaust gas [5], drive a wristwatch by converting body heat into the electrical power [6], and harvest heat for low power applications such as wireless sensor networks, mobile devices, and even medical applications [7]. On the other hand, TE devices can also be operated in the refrigeration mode and commercial products are available on the market. The applications can be found in dormitory and small refrigerators, coolers for laser systems, car seat cooler/heaters, and chip-scale coolers for photonics and microelectronics [8].

1.1 Introduction to Thermoelectrics

Thermoelectric devices are based on the Seebeck effect (for power generation) and the Peltier effect (for refrigeration), both of which were discovered in the 1800s [2]. In the power generation mode (Fig. 1.1B), a temperature difference is applied across a TE device so that hot-side charge carriers (electrons or holes) would diffuse to the cold side. Under the open-circuit condition, the cold side will end up with a higher charge carrier concentration. An internal electric field is eventually built up inside each leg to counter further thermal diffusion of charge carriers. For each leg, the negative of the built up voltage ΔV over the applied temperature difference ΔT yields its Seebeck coefficient, defined as $S = -\Delta V / \Delta T$. If we connect a TE device with an external circuit, an electrical current will be driven by the internal electrical field and electrical power is harvested from the device. For the refrigeration or cooling mode (Fig. 1.1A), an electrical current is passed through a TE device and charge carriers will carry heat from one side to the other, creating a temperature difference across the device. One advantage

of TE devices in these applications is that we can easily switch the hot and cold sides by reversing the current direction. Therefore, a TE device can be used as either a heat pump or a cooler for the same setup, which brings tremendous convenience for temperature-control applications.

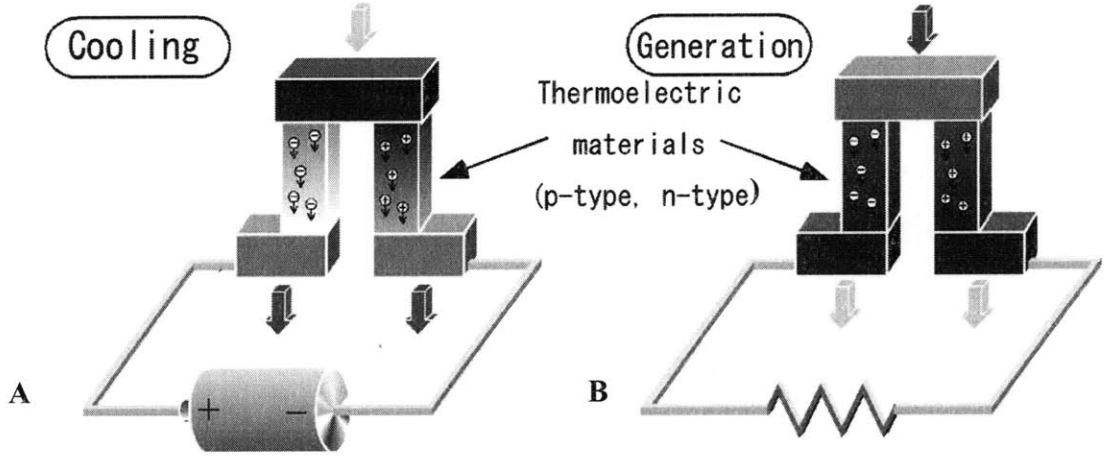

Figure 1.1 Two basic operation modes of a TE device.

The performance of a thermoelectric device, including power generators and refrigerators, depends on the dimensionless figure of merit (ZT) of the material, defined as $ZT = S^2\sigma T / k$, where S is the Seebeck coefficient, σ is the electrical conductivity, k is the thermal conductivity, and T is the absolute temperature. Since the 1950s, persistent efforts were dedicated to improve ZT values of TE materials, but the maximum ZT of commercially available materials still remained at 1. As a result, the efficiencies of TE devices are still much lower than that of a traditional mechanical cycle, which significantly limits the applications of TE technologies [9].

1.2 Thermoelectric Nanocomposites

In recent years, the idea of using nanotechnology to further improve the figure of merit of conventional TE materials has triggered active research and yielded many exciting results. Over the last decade, several groups have reported enhanced ZT in superlattices such as Bi_2Te_3/Sb_2Te_3 [10] and $PbSe_{0.98}Te_{0.02}/PbTe$ [11], and new bulk

materials, such as silver antimony lead telluride (LAST) and its alloys [12], and skutterudites [13]. In most of the reported ZT enhancements, thermal conductivity reduction plays a central role. Based on previous studies, the significant thermal conductivity reductions observed in superlattices can be mainly attributed to phonon diffuse scattering from internal interfaces, and the periodicity of superlattices is not a necessary condition [14-16]. This conclusion motivates us to pursue the nanocomposite approach as an alternative to superlattices in the quest for high ZT materials. By hot pressing nanoparticles into a bulk form, the nanocomposite approach provides a cost-effective way to obtain high ZT bulk materials, which will have significant advantages in mass production, device construction and operation compared with the thin-film superlattice structures. The interfaces inside a nanocomposite will strongly scatter phonons but slightly affect the charge carrier transport. Therefore, we can significantly reduce the lattice thermal conductivity k_L and even somewhat increase the power factor $S^2\sigma$, resulting in higher ZT than for bulk materials.

As a successful demonstration of the nanocomposite approach, we have achieved a peak ZT of 1.4 at 100 °C in our nanostructured bismuth antimony telluride (BiSbTe) bulk alloys (also called BiSbTe nanocomposites in literature) [17], a 40% increase in ZT over the bulk material. This is the first significant ZT increase in this material system in fifty years. These nanocomposites are made by hot pressing nanopowders formed from high energy ball milling commercial ingots. To avoid the ingot formation step, we synthesized nanocomposites starting from ball milling elemental chunks (bismuth, antimony, and tellurium) and obtained a peak ZT about 1.3 [18]. In addition to bismuth antimony telluride nanocomposites, we also applied the same approach to skutterudites, in which a peak ZT around 1.2 is achieved in Yb filled $CoSb_3$ nanocomposites [19]. Other successful examples of this approach can be found in nanostructured bulk silicon or silicon germanium alloys [20-23].

1.3 Fundamental Studies of TE Nanocomposites

In addition to material synthesis and characterization, I also dedicated tremendous efforts to the fundamental studies of TE nanocomposites. As an overview of the

following chapters, the background information of a few important topics is first given here.

Theoretical Analysis Based on the Boltzmann Transport Equation. Despite the advancement in high thermoelectric performance materials, detailed theoretical studies are still required to better understand the electron and phonon transport inside nanocomposites. Based on the Boltzmann transport equation (BTE) under the relaxation time approximation, I carried out detailed theoretical analysis on the measured TE properties of our nanocomposites. Such analysis provides important guidance of engineering phonon and electron transport inside nanocomposites and can be extremely useful for the future development of TE nanocomposites.

Frequency-dependent Monte Carlo simulations of Phonon Transport. For phonon transport inside nanocomposites, theoretical analysis based on the BTE provides a good starting point but it is not expected to be very accurate. The geometry of a calculated nanocomposite is only reflected on the scattering rate term v/l, where v is the phonon group velocity and l is the averaged grain size. The exact geometry of the structure, even the interface density (interface area per unit volume [24,25]), cannot be exactly treated in the analysis. To take the exact geometry into account, the lattice thermal conductivities of various periodic structures were computed by either numerically solving the BTE [26-31] or Monte Carlo (MC) simulations [24,32]. However, all these calculations were based on the gray medium approximation, i.e., a frequency-independent phonon mean free path (MFP). This approximation could lead to a significant underestimation of phonon size effects inside micro- to nano-structured bulk materials. To obtain more accurate thermal conductivity predictions, I have conducted Monte Carlo simulations on 2D periodic porous silicon [33] and 3D silicon nanocomposites [34]. In the past, very few papers performed frequency-dependent MC simulations on thin films [35], nanowires [36-38], or 1D transient phonon transport [39]. My work is the first attempt to apply the Monte Carlo method to more complicated geometries with inclusion of frequency-dependent phonon scattering. It should be noted that my Monte Carlo simulation code can also be extended to transient cases, which is discussed at the end of Chap. 4.

Interface Studies of Nano-grain Boundaries. Electron transport in nanostructured TE materials can be significantly affected by the interfacial electronic states [40]. To better understand the charge carrier transport process across the grain interfaces, I have conducted interface capacitance measurements to find out the electronic barrier height at the interfaces, which is critical for the detailed theoretical analysis of the interfacial charge transport and energy conversion processes. Although large amount of work has been done using the technique to understand the defect states and the barrier height of polycrystalline silicon grain boundaries [41-45], this method has not been applied to TE materials. Challenges associated with application of the capacitance measurement technique to TE materials will be discussed in Chap. 5.

Bandgap Measurement of Nanopowders. In theoretical analysis of charge carrier transport, one important parameter is the band gap of a material. For TE nanocomposites, in some cases the optimized composition diverges a lot from that for their bulk counterparts. One example can be our $Yb_xCo_4Sb_{12}$ nanocomposites [19], in which the optimized x value (0.35) is even higher than the highest reported x value (0.29) for bulk samples [46]. Such a contrast in compositions may lead to a non-negligible difference in band gaps. Other factors, including local composition/structure variations inside nanocomposites, could also affect their band gaps. Keeping these in mind, it is important for us to develop a simple measurement technique to quickly check the band gaps of various TE nanocomposites. In Chap. 5, Fourier Transform Infrared Spectroscopy (FTIR) is applied to ball milled nanopowders to obtain their absorption pattern, from which the band gap can possibly be extracted. This attempt may introduce a new characterization tool to future TE research.

1.4 The Scope and Organization of this Thesis

As a summary of my work on TE nanocomposites, I try to keep a good balance between theories and experiments in this thesis, and better connect the fundamental physics with material synthesis. All discussions are focused on two types of nanocomposites: nanostructured BiSbTe bulk alloys [17,18] and $Yb_xCo_4Sb_{12}$ nanocomposites [19]. The thesis is organized as following:

In Chap. 2, major experimental aspects of TE nanocomposites are introduced in detail, including material synthesis, characterization, and device cooling test. Concerns and challenges are discussed for each topic. These nanocrystalline bulk materials were made by hot-pressing nanopowders obtained from high energy ball milling either commercial ingots [17] or element chunks [18,19]. Tremendous efforts were dedicated to assuring accurate and dependable measurements of their TE properties. In addition to comparing measurement results between commercial setups and my home-built measurement system, a device cooling test was also conducted to confirm the high ZT obtained in our nanostructured BiSbTe bulk alloys.

In Chap. 3, detailed theoretical analysis based on the BTE under the relaxation time approximation is carried out on measured thermal and electrical properties of nanocomposites. Such analysis is important for us to understand the fundamental physics of TE nanocomposites, and thus provide useful guidance for future improvement on their properties.

To obtain more accurate lattice thermal conductivity predictions, in Chap. 4 frequency-dependent MC simulations of phonon transport are conducted on 2D periodic porous silicon and 3D silicon nanocomposites. In the TE field, the latter one provides the first accurate prediction for phonon size effects in specified nanocomposites. With more accurate information on phonon MFPs in other materials, frequency-dependent MC simulations of phonon transport can also be conducted for their nanocomposites to provide useful guidance for material synthesis.

In Chap. 5, bandgap measurements of nanopowders and grain-interface capacitance measurements on nanocomposites are discussed in detail. Finally, Chap. 6 concludes the thesis with recommended research directions. Continued work on these topics can be important for the future development of TE nanocomposites.

1.5 References

[1] R. F. Service, *Science* **306**, 806 (2004).

[2] H. J. Goldsmid, *Thermoelectric Refrigeration* (Plenum, New York, 1964).

[3] T. M. Tritt, Ed. *Semiconductors and Semimetals, Recent Trends in Thermoelectric Materials research: Part One to Three* (Academic, San Diego, CA, 2001), vol. 69 to 71.
[4] D. M. Rowe, Ed. *CRC Handbook of Thermoelectrics* (CRC, Boca Raton, FL, 1995).
[5] J. H. Yang, *Proc. 24th Int. Conf. Thermoelectrics*, South Carolina, USA (2005).
[6] M. Kishi, H. Nemoto, T. Hamao, M. Yamamoto, S. Sudou, M. Mandai, and S. Yamamoto, *Proc. 18th Int. Conf. Thermoelectrics*, Maryland, USA (1999).
[7] J. A. Paradiso and T. Starner, *IEEE Pervasive Computing* **4**, 18 (2005).
[8] Ihtesham Chowdhury, Ravi Prasher, Kelly Lofgreen, Gregory Chrysler, Sridhar Narasimhan, Ravi Mahajan, David Koester, Randall Alley, and Rama Venkatasubramanian, *Nature Nanotech.* **4**, 235 (2008).
[9] Cronin B. Vining, *Nature Mater.* **8**, 83 (2009).
[10] R. Venkatasubramanian, E. Siivola, T. Colpitts, and B. O'Quinn, *Nature* **413**, 597 (2001).
[11] T. C. Harman, P. J. Taylor, M. P. Walsh, and B. E. LaForge, *Science* **297**, 2229 (2002).
[12] K. F. Hsu, S. Loo, F. Guo, W. Chen, J. S. Dyck, C. Uher, T. Hogan, E. K. Polychroniadis, and M. G. Kanatzidis, *Science* **303**, 818 (2004).
[13] J. P. Fluerial, T. Caillat, and A. Borshchevsky, *Proc. 13rd Int. Conf. Thermoelectrics,* Kansas, USA (1994).
[14] G. Chen, *Phys. Rev. B* **57**, 14958 (1998).
[15] M. S. Dresselhaus, G. Chen, M. Y. Tang, R. G. Yang, H. Lee, D. Z. Wang, Z. F. Ren, J.-P. Fleurial, P. Gogna, *Adv. Mater.* **19**, 1043 (2007).
[16] G. Chen and R.G. Yang, *Materials Integration*, special issue, Vol. 18, (2005).
[17] B. Poudel, Q. Hao, Y. Ma, Y. C. Lan, A. Minnich, B. Yu, X. Yan, D. Z. Wang, A. Muto, D. Vashaee, X. Y. Chen, J. M. Liu, M. S. Dresselhaus, G. Chen, and Z. F. Ren, *Science* **320**, 634 (2008).
[18] Y. Ma, Q. Hao, B. Poudel, Y. C. Lan, B. Yu, D. Z. Wang, G. Chen, and Z. F. Ren, *Nano Lett.* **8**, 2580 (2008).
[19] J. Yang, Q. Hao, H. Wang, Y. C. Lan, Q. Y. He, A. Minnich, D. Z. Wang, J. A. Harriman, V. M. Varki, M. S. Dresselhaus, G. Chen, and Z. F. Ren, *Phys. Rev. B* **80**, 115329 (2009).
[20] G. H. Zhu, H. Lee, Y.C. Lan, X.W. Wang, G. Joshi, D.Z. Wang, J. Yang, D. Vashaee, H. Guilbert, A. Pillitteri, M.S. Dresselhaus, G. Chen, and Z.F. Ren, *Phys. Rev. Lett.* **102**, 196803 (2009).
[21] S. K. Bux, R. G. Blair, P. K. Gogna, H. Lee, G. Chen, M. S. Dresselhaus, R. B. Kaner, and J. P. Fleurial, *Adv. Fun. Mater.* **19**, 2445 (2009).
[22] G. Joshi, H. Lee, Y. C. Lan, X. W. Wang, G. H. Zhu, D. Z. Wang, R. W. Gould, D. C. Cuff, M. Y. Tang, M. S. Dresselhaus, G. Chen, and Z. F. Ren, *Nano Lett.* **8**, 4670 (2008).
[23] X. W. Wang, H. Lee, Y. C. Lan, G. H. Zhu, G. Joshi, D. Z. Wang, J. Yang, A. J. Muto, M. Y. Tang, J. Klatsky, S. Song, M. S. Dresselhaus, G. Chen, and Z. F. Ren, *Appl. Phys. Lett.* **93**, 193121 (2008).
[24] M. S. Jeng, R. G. Yang, D. Song, and G. Chen, *ASME J. Heat Transfer* **130**, 042410 (1-11) (2008).

[25] A. Minnich, G. Chen, *Appl. Phys. Lett.* **91**, 073105 (2007).
[26] R. G. Yang, G. Chen, *Phys. Rev. B* **69**, 195316 (2004).
[27] R. G. Yang, G. Chen, and M. S. Dresselhaus, *Phys. Rev. B* **72**, 125418 (2005).
[28] R. Prasher, *J. Appl. Phys.* **100**, 034307 (2006).
[29] K. Miyazaki, T. Arashi, D. Makino, and H. Tsukamoto, *IEEE Trans. Comp. Pack. Tech.* **29**, 247 (2006).
[30] A. Pattamattaa and C. K. Madnia, *Int. J. Heat Mass Transfer* **52**, 860 (2009).
[31] J.-D. Chung and M. Kaviany, *Int. J. Heat Mass Transfer* **43**, 521 (2000).
[32] W. X. Tian and R. G. Yang, *J. Appl. Phys.* **101**, 054320 (2007).
[33] Q. Hao, G. Chen, and M. S. Jeng, *J. Appl. Phys.* **106**, 114321 (2009).
[34] Q. Hao, G. Chen, G. H. Zhu, X. W. Wang, A. Minnich, Z. F. Ren, submitted.
[35] S. Mazumder, A. Majumdar, *ASME J. Heat Transfer* **123**, 749 (2001).
[36] Y. F. Chen, D. Y. Li, J. R. Lukes, A. Majumdar, *ASME J. Heat Transfer* **127**, 1129 (2005).
[37] D. Lacroix, K. Joulain, D. Terris, D. Lemonnier, *Appl. Phys. Lett.* **89**, 103104 (2006).
[38] J. Randrianalisoa and D. Baillis, *ASME J. Heat Transfer* **130**, 072404 (2008).
[39] D. Lacroix, K. Joulain, and D. Lemonnier, *Phys. Rev. B* **72**, 064305 (2005).
[40] A. Minnich, M. S. Dresselhaus, Z. F. Ren, and G. Chen, *Energy Environ. Sci.* **2**, 466 (2009).
[41] C. H. Seager, G. E. Pike, *Appl. Phys. Lett.* **35**, 709 (1979).
[42] C. H. Seager, G. E. Pike, *Appl. Phys. Lett.* **37**, 747 (1980).
[43] G. E. Pike, *Phys. Rev. B* **30**, 795 (1984).
[44] C. H. Seager, G. E. Pike, and D. S. Ginley, *Phys. Rev. Lett.* **43**, 532 (1979).
[45] D.V. Lang, *J. Appl. Phys.* **45**, 3023 (1974).
[46] H. Li, X. F. Tang, Q. J. Zhang, and C. Uher, *Appl. Phys. Lett.* **93**, 252109 (2008).

Chapter 2. Material Synthesis, Characterization, and Device Cooling Test

This chapter covers several major experimental aspects of my nanocomposite research, from material synthesis, characterization, to device cooling test. As a collaborating effort, the material synthesis was performed at Boston College, whereas I was mainly responsible for the sample characterization, device testing, and theoretical explanations of all measured properties. Nanocomposites of two important materials systems are discussed here, including p-type bismuth antimony telluride nanocomposites (also called nanostructured $Bi_xSb_{2-x}Te_3$ bulk alloys in the literature) [1-4], and n-type $Yb_xCo_4Sb_{12}$ nanocomposites [5]. These nanocrystalline bulk materials were made by hot-pressing nanopowders obtained from high energy ball milling either commercial ingots [1,3] or element chunks [2,4-6].

2.1 Brief Review of Thermoelectric Nanocomposites

In 1993, Dresselhaus and co-workers first proposed using quantum wells to increase the power factor via quantum confinement of electrons and reduce thermal conductivity via phonon size effects [7]. As a practical implementation of these quantum-well structures, various superlattices were widely studied and enhanced ZT were reported in superlattices such as Bi_2Te_3/Sb_2Te_3 [8] and $PbSe_{0.98}Te_{0.02}/PbTe$ [9]. It has been demonstrated that observed ZT enhancement mainly resulted from the thermal conductivity reduction. Based on previous studies in our group, the significant thermal conductivity reductions observed in superlattices can be mainly attributed to phonon diffuse scattering on the internal interfaces, and the periodicity of superlattices is not a necessary condition [10-12]. This conclusion motivates us to pursue the nanocomposite approach as an alternative to superlattices in the quest for high ZT materials [11-15]. In general, nanocomposites have two forms: 1) nanostructures (e.g., nanoparticles, nanowires) embedded in a host matrix material, 2) a heterostructure geometry with nanoparticles of different materials adjacent to each other. When all nanoparticles are of

the same material, the second form becomes nano-grained bulk materials, which is the case for most of our nanocomposites.

For the nanostructure-in-a-host form, thermal conductivity reduction was achieved by adding BN and B_4C nanoparticles into a SiGe alloy but the net gain in ZT was small due to the electrical conductivity deterioration [16]. This is because the added inert particles possess a large band gap and thus a higher electric potential barrier to scatter electrons in addition to phonons. It was suggested that constituent materials in nanocomposites should have significant differences in lattice properties, but negligible differences in electronic properties [12]. This can be treated as a general rule of choosing suitable nano-inclusions for ZT enhancement. With a hot pressing procedure, the effective thermal conductivity of a Bi_2Te_3 nanocomposite with tubular Bi_2Te_3 nanowire inclusions was reduced, leading to a 25% increase in ZT compared to homogenous bulk materials [17]. Similarly, the thermal conductivity of PbTe was significantly reduced by dispersing Sb or InSb nanocrystals into it but other material properties were not measured for ZT calculations [18]. In other attempts, nanoscale precipitates were induced inside bulk samples by thermal processing techniques. High ZTs have been reported in n-type $AgPbTe_2$/PbTe [19], n-type $Pb_{1-x}Sn_xTe$/PbS [20], and p-type $Na_{1-x}Pb_mSb_yTe_{m+2}$ [21]. With Si precipitates formed in PbTe doped with PbI_2, the mechanical robustness was improved though the optimized ZT was only 0.9 at 675 K [22].

Collaborating with Prof. Zhifeng Ren's group at Boston College, we have carried out research on the second form of a nanocomposite, i.e., nanoparticle composites [1-6]. In BiSbTe nanocomposites, nano-sized precipitates are further induced inside nanograins and contribute to the thermal conductivity reduction. With the same ball mill and hot press techniques, enhanced thermoelectric performance in various nanocomposites was also reported by other groups [23-27].

2.2 Material Synthesis

As mentioned before, the synthesis of nanocomposites has two steps: nanoparticle preparation and hot press [1-6]. At the beginning of this nanocomposite research, we pursued preparing Bi_2Te_3 and other types of nanoparticles (e.g. Bi_2Se_3, Sb_2Te_3) by a wet chemistry method. However, the hot-pressed Bi_2Te_3 nanocomposites were all confirmed

to be n-type by Seebeck coefficient measurements, whereas bulk Bi_2Te_3 samples with the same compositions are expected to be p-type (Fig. 2.1). The low Seebeck coefficients in nanocomposites thus obtained resulted in ZT values much lower than their bulk counterpart. The same problems were also found in nanocomposites hot pressed from Bi_2Te_3 together with Sb_2Te_3 nanoparticles. In the literature, it was found that oxidation of Bi_2Te_3 particles will function as donors and thus change the type of hot-pressed samples [28]. Low Seebeck coefficients are expected due to the cancellation of Seebeck coefficient contributions from electrons and holes. We verified this fact by hot pressing the same commercial Bi_2Te_3 micro-particles with and without hydrogen reduction. In preliminary tests, a sample made from hydrogen reduced Bi_2Te_3 particles (named "Bi_2Te_3 050406 with H_2 reduction" in Fig. 2.1) became p-type, while the comparison sample without hydrogen reduction was still n-type ("Bi_2Te_3 042806 no H_2 reduction"). It should be noted that oxygen was not completely removed by H_2 reduction in Sample "Bi_2Te_3 050406" and its Seebeck coefficient still became negative above 130 °C (Fig. 2.2). The existence of oxygen in earlier hot pressed samples was also confirmed by energy dispersive X-ray spectroscopy (EDX).

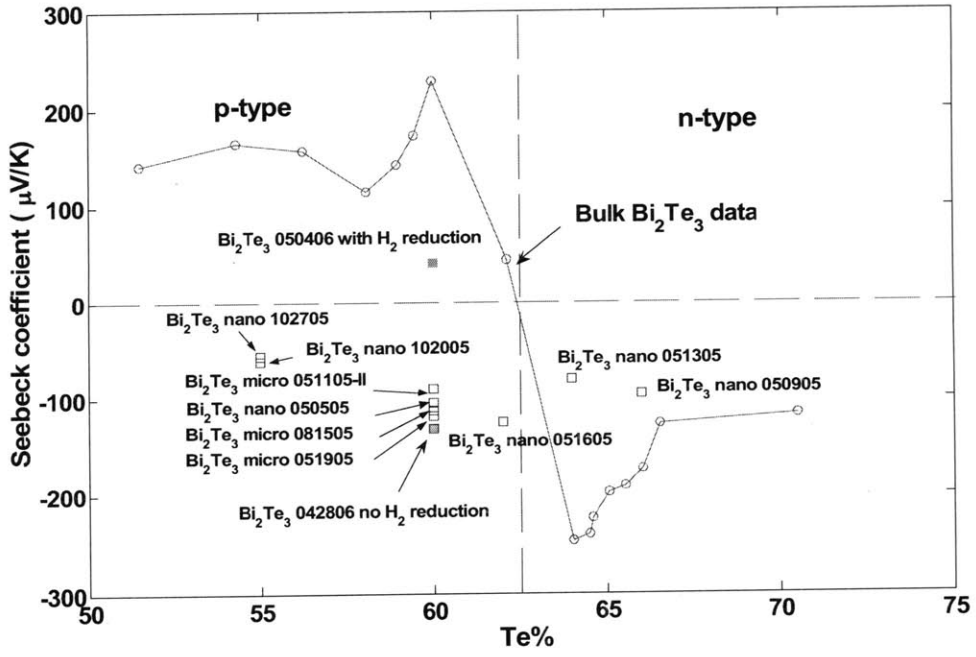

Figure 2.1 Seebeck coefficients as a function of Te percentage for selected Bi_2Te_3 nanocomposites, with nanoparticles prepared by wet chemistry.

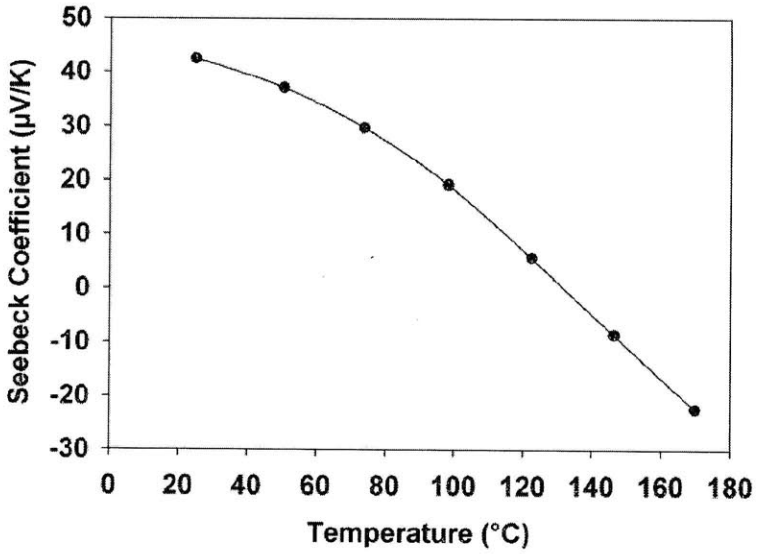

Figure 2.2 Temperature-dependent Seebeck coefficient of Sample "Bi_2Te_3 050406 with H_2 reduction" in Fig. 2.1.

Despite the success in obtaining the right sign of the Seebeck coefficient, its absolute value was still much lower than that for the bulk counterpart. In practice, it was difficult to remove all oxygen inside particles by hydrogen reduction to achieve expected Seebeck coefficients. In addition, the high reaction temperature (~400 °C) could also lead to particle sintering during the hydrogen reduction process and nano-features will be lost in hot-pressed samples. Keeping these in mind, we switched to preparing nanoparticles by high energy ball milling, a simple and cheap physical method. To do this, commercial ingots or element chunks (with the right molar ratio between elements) were cut into centimeter sized pieces and loaded into a zirconia jar inside the glove box in an Ar atmosphere. A few zirconia balls (5-15 mm size) were also added and sealed. The sealed jar was placed into a high energy ball mill. The exact ball milling time was optimized for different nanocomposites and the obtained nanoparticle sizes were mostly below 50 nm. Compared with the wet chemistry method, high energy ball mill with Ar protection eliminates the possibility of oxidation and is more suitable for mass production.

While making nanopowders, our collaborators at Boston College (BC) also constructed two hot press setups, a Plasma Pressure Compaction (P^2C) device (Fig. 2.3) and a furnace heating device (Fig. 2.4). Our BC collaborators did a series of tests with

both setups to find out the optimized conditions for making various TE nanocomposites. In the P^2C device, the high current going through packed nanoparticles creates fast Joule heating while the piston applies high pressure. Nanoparticles are compacted into the bulk form (disk shape) during the process. For the furnace hot press setup, nanoparticles under high pressure are heated inside a furnace to form nanocomposites. Generally speaking, furnace hot press requires longer time (30 min to 1 hr) to form consolidated nanocomposites, while P^2C hot press can be much faster (a few minutes). As a result, nanocomposites synthesized by the P^2C setup have preferred smaller grain sizes because of the much shorter heating period. Compared with furnace hot press, the faster P^2C hot press is also more suitable for mass production. Due to the difference in heating methods, nanocomposites produced by the P^2C device are more uniform in their materials properties, while nanocomposites from the furnace hot press often have apparent property change from the center to edges. Because of its many advantages, the P^2C device was used to synthesize most of our later samples though we started the nanocomposite research with the furnace hot press setup.

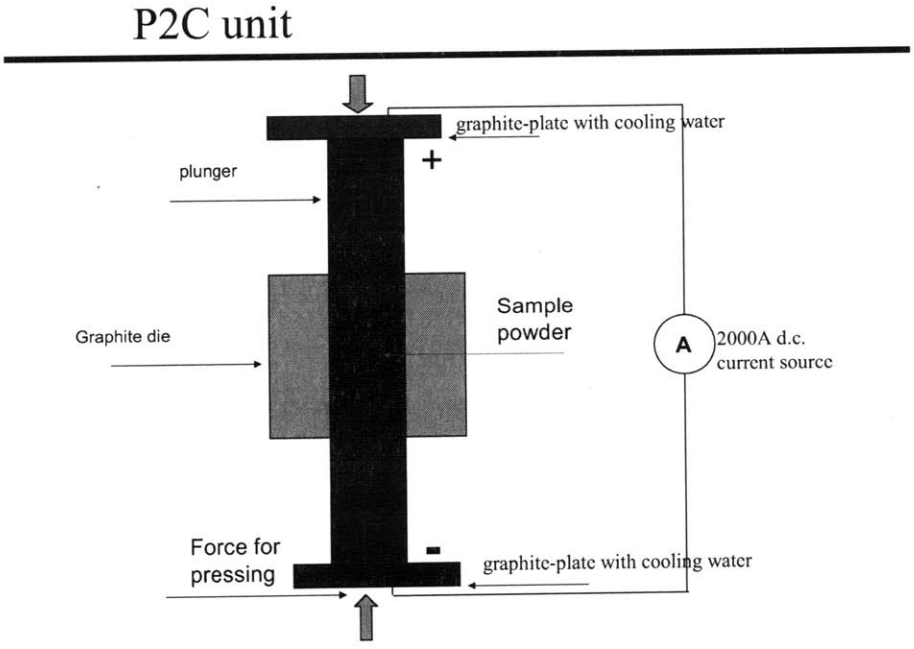

Figure 2.3 Plasma Pressure Compaction (P^2C) hot press setup.

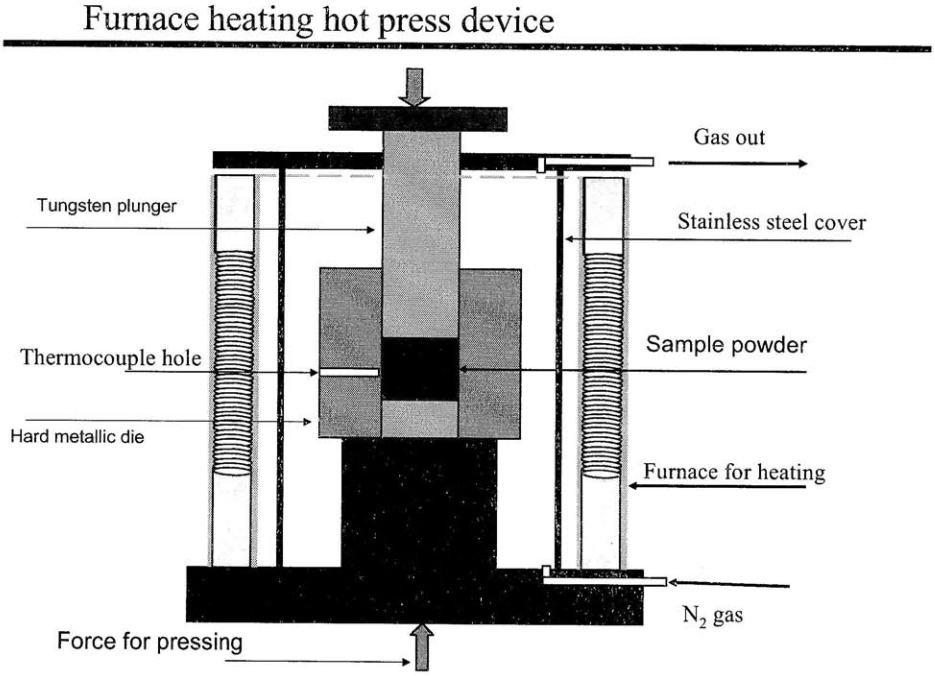

Figure 2.4 Furnace heating hot press setup.

2.3 Material Characterization

2.3.1 Review of Thermoelectric Property Measurements

One of the most important aspects of thermoelectrics research is the materials characterization. For bulk TE materials, a 20% ZT increase is significant. Due to measurement errors in individual properties, ZTs calculated from σ, k, S values can easily have a 10-20% error and thus cause arguments for published high ZT results. For instance, a ZT of 1.64 at 800 °C was reported in $TiO_{1.1}$ [29], which was claimed as the highest ZT value around this temperature. However, this result was never reproduced in our own tests, where the highest ZT was only 0.23 (Fig. 2.5) with optimized x=1.83 in TiO_x ($1 \le x \le 2$) [30]. Such a big contrast in ZT values may be attributed to undependable measurements conducted in Ref. 29. Accurate measurements become more challenging for superlattices and more inconsistencies can be found in the literature. As an example, Harman et al. reported ZT =1.6 at T=300 K for PbTe/PbSe nanodots superlattices (NDSLs) [9]. This ZT value was determined by measuring the maximum temperature change produced by a TE device where one leg of the device was the NDSL

and the other leg was a gold wire. The lattice thermal conductivity was extracted from the *ZT* value and separately measured electrical properties. At room temperature, it was estimated as 0.33 W/m·K, in comparison with 2.01 W/m·K for bulk PbTe. Recently, Cahill and co-workers found that the lattice thermal conductivities of NDSLs were actually similar to $PbTe_{1-x}Se_x$ alloys with the same average composition, without benefit from nanostructuring [31]. Using data for the in-plane power factor $S^2\sigma$ and the through-thickness thermal conductivity, a maximum *ZT* of 0.6 was calculated at 300 K and casted doubts on previously reported ZT values.

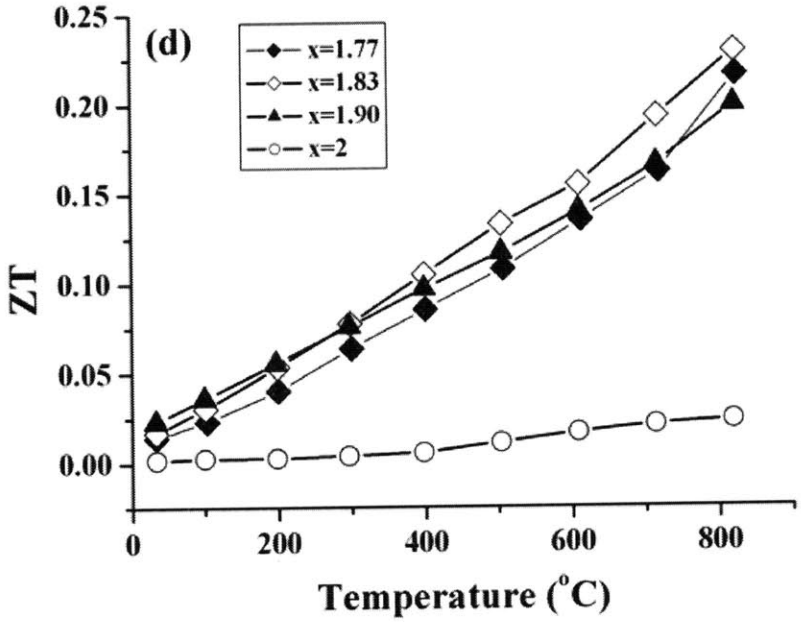

Figure 2.5 ZT of various TiO_x samples [30]. The optimized composition was found to be $TiO_{1.83}$, with ZT~0.23 at 800 °C.

As a general overview, a few important issues in TE property measurements are listed as below:

1) For Bi_2Te_3 and Sb_2Te_3, their bulk materials have layered crystal structures [32] and are strongly anisotropic in transport properties [33,34]. Although they become more isotropic in a composite form with randomized grain crystal orientations, it is still important to verify this in measurements [1,3]. In some studies, electrical properties were typically measured along the in-plane direction of a hot-pressed disc, while the thermal

diffusivity was measured along the out-of-plane direction by a laser flash setup. This may yield significant ZT overestimations in Bi_2Te_3 and Sb_2Te_3 nanocomposites, which could be the case for high ZT values reported in Ref. 35.

2) In high-temperature Seebeck coefficient measurements, we should pay attention to the temperature difference ΔT_r between a sample and a thermocouple, caused by the thermal contact resistance R_c between the two and sample heat leakage Q_l through the thermocouple. Temperature reading errors from ΔT_r become critical for thick thermocouples using pressure contacts. In heat transfer, $\Delta T_r = R_c Q_l$ and ΔT_r can be reduced by decreasing either R_c or Q_l. The former one can be achieved by spark welding or soldering thermocouples onto a sample. To lower Q_l, thinner thermocouples can be used but it is not practical for pressure contacts. In some experimental setups, the middle part of a thermocouple is thermally grounded to a region with a temperature close to the sample surface temperature. Close to the sample, the temperature gradient along a thermocouple is removed and heat leakage Q_l can be eliminated.

3) Cautions should also be taken for possible contaminations between thermocouples and measured materials at high temperatures. For example, thermocouples using platinum are readily contaminated by contact with elements such as lead, zinc, phosphorus, arsenic and silicon [36]. In measurements of SiGe nanocomposites, the type R thermocouple (platinum–rhodium alloy) reading can be significantly changed after such contaminations, resulting in wrongly measured Seebeck coefficients. Although an impervious sheath can be utilized to shield these thermocouples, ΔT_r is increased due to the existence of the sheath. On the other hand, elements in thermocouples can also be toxic to some TE materials and change their properties during measurements. Keeping these in mind, we always need to check the phase diagram between all elements in thermocouples and TE materials before measurements.

2.3.2 Home-Built Measurement System

My measurement efforts are mainly focused on developing a home-built system that can measure all three thermoelectric properties in the same run. This is especially important for samples that change their properties during high-temperature measurements. In this case, measuring individual properties in separated runs may lead to significant errors in the calculated ZT. This measurement setup is based on a commercial cryostat chamber system working from liquid nitrogen temperature up to 500 °C under vacuum. The vacuum level is normally around 6×10^{-5} torr with a mechanical-turbo pump system, and 10^{-3} torr only with a mechanical pump. Due to the usage of soldering for electrical connections, all measurements are limited to temperatures below 300 °C. We can remove this restriction by replacing soldering with conductive glues such as platinum pastes.

Our hot pressed disk-shaped samples are 12.7 mm in diameter and 2 mm in thickness. To measure their properties, bars of about 2×2×12 mm are cut and polished from the pressed disks for thermoelectric properties characterization (Fig. 2.6). Figure 2.7 illustrates the method used for temperature-dependent property measurements and Fig. 2.8 displays the photo of the real setup. The sample is first glued onto a copper or aluminum stand by an alumina paste. The stand will be later screwed onto the cold-finger sample holder inside the cryostat chamber for temperature-dependent measurements. Two 1 mil Pt wires are spark welded onto the middle part of the bar sample as voltage probes for both thermal diffusivity measurements and four-probe electrical conductivity measurements. In addition, two thermocouples are soldered onto both ends of the sample. To do this, both ends of the sample are first plated with nickel with a nickel plating pen. On top of the sample, a heater is glued with alumina pastes, with two current injection wires soldered onto the heater. My setup greatly accelerates the sample-mounting process and also shows good repeatability in systematic tests. Methods to measure the electrical conductivity, thermal diffusivity, and Seebeck coefficient are described below.

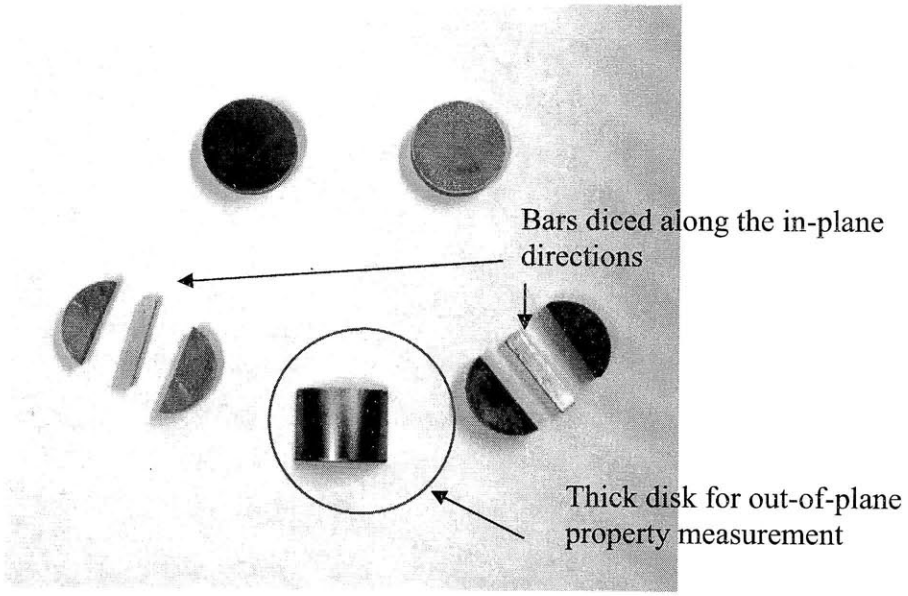

Figure 2.6 Hot pressed disk-shaped samples and bars diced along the in-plane direction of disks. The hot press direction is always along the axial direction (out-of-plane direction) of a disk sample. To check the out-of-plane electrical properties, we also hot pressed very thick disks and diced bars along its axial direction.

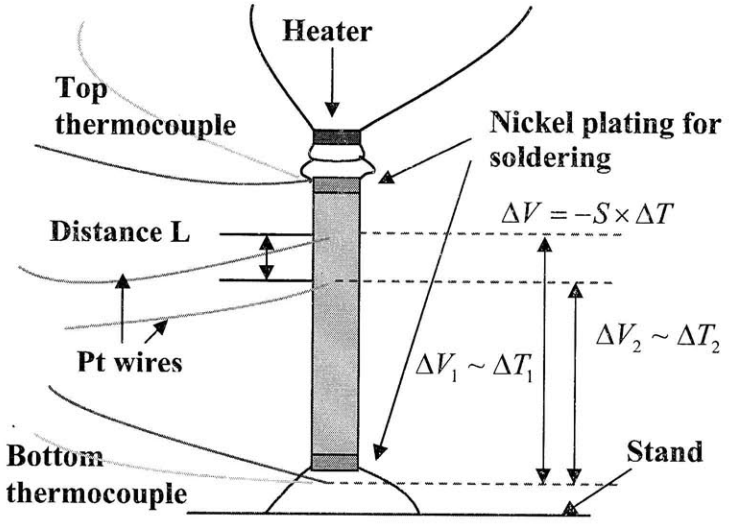

Figure 2.7 Experimental setup of temperature-dependent property measurements.

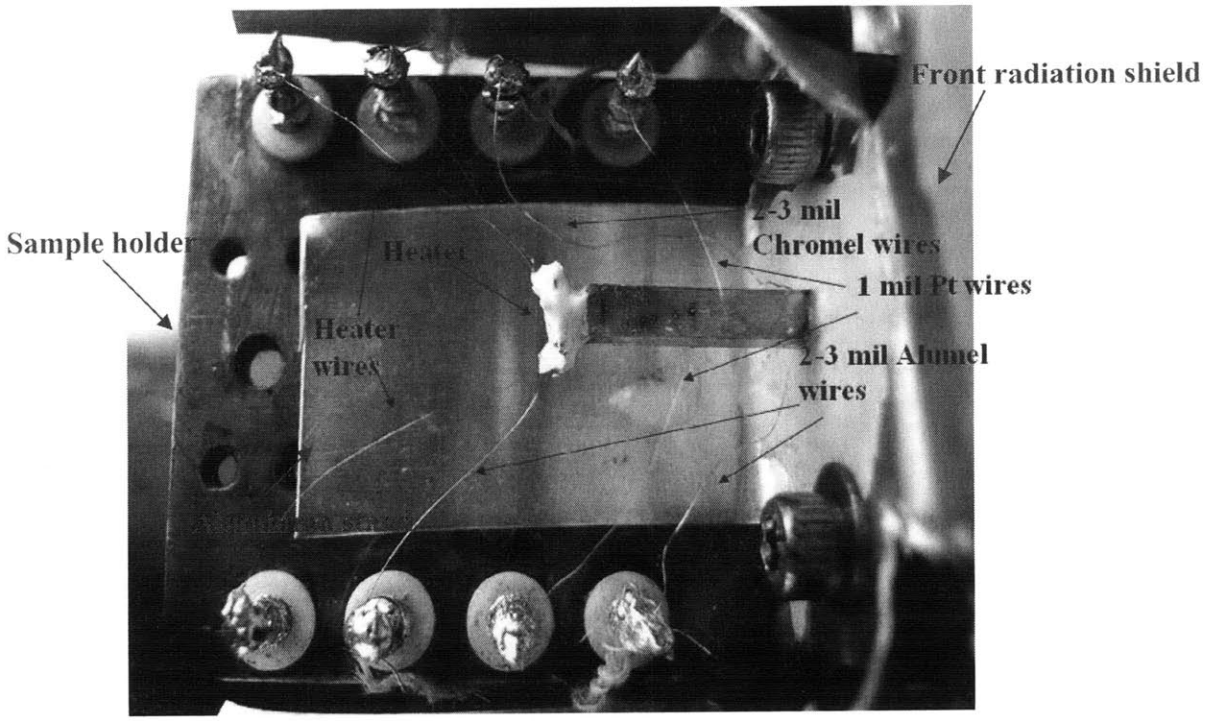

Figure 2.8 Photo of the real experiment setup. The floating ends of all wires are tightly twisted onto thicker extension wires and then fixed by soldering them onto the eight soldering terminals of the sample holder. These extension wires are further connected to feedthroughs of the cryostat chamber to convey signals out of the vacuum. The Al stand will be bent to block the front side of the sample after its mounting.

Thermal Diffusivity Measurements. The simplest thermal conductivity measurement is based on one-dimensional heat conduction along a bar sample in a good vacuum [34]. In the steady state, the amount of heat Q flowing through a sample is related to the temperature difference ΔT developed across the sample by $Q = kA\Delta T / L$, in which A is the sample cross sectional area, L is the sample length, and the thermal conductivity k can thus be calculated from the measured Q and ΔT. Despite its simplicity, the steady-state measurements become inaccurate for TE samples whose thermal conductivities are typically less than 5 W/m·K. In this case, radiation loss along the sample sidewalls can no longer be neglected. As a result, Q significantly decays along the sample and errors will occur in calculations assuming conserved Q. To avoid such inaccuracies, we exploit the Ångström method that is independent of the radiation heat loss on the sample sidewalls [37]. In this measurement, the top of a bar sample is

periodically heated and sinusoidal temperature variations of two separated points along a sample are recorded. Assuming that the radiation heat transfer coefficient remains constant along the sample, Ångström [37] shows that thermal diffusivity α can be calculated by

$$\alpha = \frac{l^2}{2\Delta t \ln \frac{M}{N}}, \tag{2-1}$$

in which l is the distance between two points, M and N are the sinusoidal temperature variations at individual points, and Δt is the phase difference between the two temperature curves (Fig. 2.9). Typically Δt is in the range of 2-20 s for the used ac heating current frequency (25-35 mHz). With measured thermal diffusivity α, the thermal conductivity can be calculated by $k = \rho C \alpha$, in which the specific heat C and sample density ρ are both measured by commercial setups at Boston College.

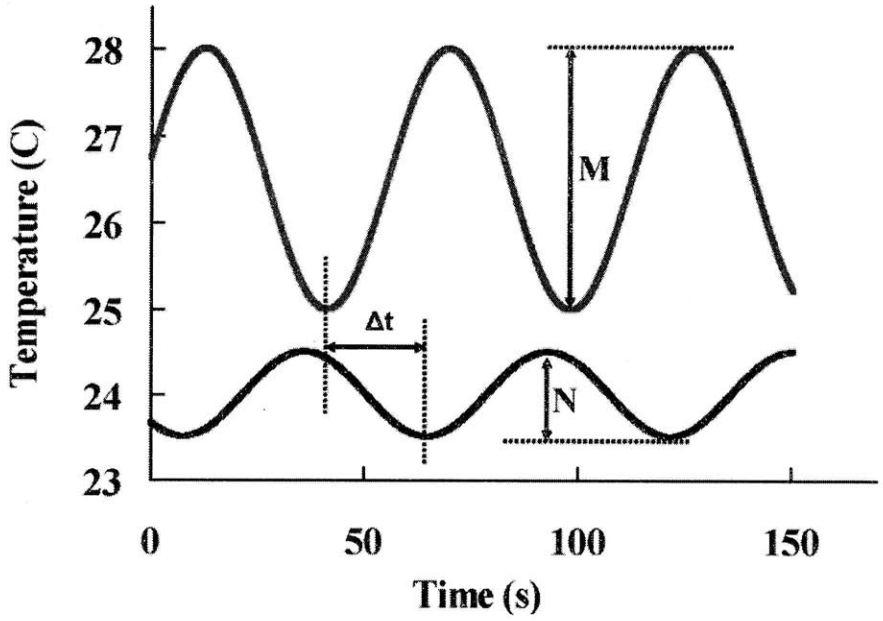

Figure 2.9 Temperature variations of two separated points along a bar sample.

At the beginning, the temperatures of the selected two points are read from thermocouples spark welded onto a sample. However, such a spark welding process was found to be very difficult. To save the time for sample mounting, I changed the setup to

eliminate the need of welding two thermocouples, and instead used a single 1 mil Pt wire at each point [34], as is shown in Figs. 2.7 and 2.8. Because of the much smaller diameter of a single 1 mil wire, it became easier to induce sparks at the wire tip (stronger local electrical field for sharper wires) and the repeatability of spark welding was significantly improved. The new setup takes advantage of the high Seebeck coefficients of TE samples. Neglecting the Seebeck coefficient change along a sample periodically heated on its top, the Seebeck voltage developed between each Pt wire and the bottom alumel leg is proportional to the real temperature drop (see Fig. 2.7). Therefore, we can simply record the voltage signals to extract the amplitude and phase information of the corresponding temperature variations. Because our TE nanocomposites have much higher Seebeck coefficients than thermocouple wires, the voltage signals in the improved setup are stronger and better accuracies can be achieved with an increased signal-to-noise ratio.

Electrical Conductivity Measurements. Because of the low electrical resistance of our TE samples (~ 10 mΩ), four-probe electrical measurements are employed to avoid the influence of the electrical contact resistance in the two-probe electrical conductivity measurements. In this case, alumel legs in the top and bottom thermocouples are used for the current injection, while the two Pt wires are utilized as voltage probes (see Figs. 2.7 and 2.8). To ensure one dimensional current flow, each voltage probe is positioned to be away from it nearest sample end by a distance no shorter than the sample cross section dimension (~2 mm) [38].

With a dc current passing through a TE sample, the measured voltage can be expressed as $V = IR + S\Delta T$, in which I is the current, R is the sample resistance, S is the Seebeck coefficient, and ΔT is the temperature difference between the voltage probes. This ΔT mostly originates from the Peltier heating and cooling at the current injection ends. To eliminate the $S\Delta T$ term, an ac current is used instead in measurements so that a ΔT will not be developed between voltage probes because of alternate heating and cooling on each end [39]. For our low thermal diffusivity samples, the ac temperature oscillations on both current injection ends, caused by Peltier heating/cooling (frequency f) and ac Joule heating (frequency at least $2f$) on soldering junctions, are restricted to a

length on the order of $\sqrt{\alpha / f}$. With a typical thermal diffusivity $\alpha = 1 \times 10^{-6}$ m^2/s and an ac frequency f =250 Hz, we estimate this length to be 0.06 mm, indicating negligible influence on voltage measurement regions.

In a different method called the "dc method", the $S\Delta T$ term can be cancelled out by suddenly switching the current polarization, in which the voltage jump at this instant equals $2IR$ [40]. Similarly, the current I can also be suddenly zeroed and the voltage jump will equal IR in this situation. The assumption here is that the sample temperature changes are much slower than the transient voltage reading speed. For our bulk samples with low thermal diffusivities, the time constant of the temperature changes is on the order of 100 s, which is much larger than the voltage sampling interval (10^{-4} s). In room-temperature tests, the divergence between ac and dc measurements is within 2% for the same sample.

In measurements, the injected ac current is ramped up and down and the corresponding ac voltages are recorded along the way. Special attention should be paid to high-temperature electrical conductivity measurements. Because the top end of the sample is thermally floated, the mounted sample is not thermally symmetric and relatively large ΔT (~2 K) can still be developed across the sample even in ac measurements. We can decompose this ΔT into the dc part and ac part. As discussed before, temperature ac oscillations on both ends will not affect the voltage measurement region. On the other hand, changing the injected current will lead to notable variations in the dc part of ΔT, mainly caused by the Joule heat generated in the current loop and sidewall radiation loss along the sample. After each current adjustment, we need to wait for a long enough time (~100 s) before taking voltage measurements. Otherwise, the unsaturated dc part of ΔT will distort the sinusoidal voltage signals and the amplitude of the measured ac voltage will still change with time. The I-V curves thus obtained will not pass the origin.

The sample resistance R is obtained from the slope of the linear I-V curve. The criteria for a dependable measurement is that the I-V curves for the injection current ramping up and down must overlap each other, pass the origin, and have good linearity (R^2 >0.99). The electrical conductivity σ can then be calculated by $\sigma = L / AR$, in which A is again sample cross section area, the length L is the separation between

voltage probes. In practice, L is read under a microscope equipped with a ruler in one optical lens. Compared with voltage probes glued onto a sample by an epoxy, errors in L can be minimized using spark welded thin wires.

Seebeck Coefficient Measurements. The Seebeck coefficients are measured with the two soldered thermocouples on both ends of a bar sample. The slope method [34] is utilized for Seebeck coefficient measurements, and the alumel legs of the thermocouples are also used as voltage probes. This eliminates the need for additional voltage probes. By ramping up the heating power of the heater, the temperature difference ΔT (2-5 K) across a sample is measured along with the corresponding voltage drop ΔV. The Seebeck coefficient is computed as

$$S = -\frac{d\Delta V}{d\Delta T} + S_{Alumel}, \tag{2-2}$$

where $\frac{d\Delta V}{d\Delta T}$ is the slope of the obtained ΔT vs. ΔV curve, S_{Alumel} is the alumel wire Seebeck coefficient evaluated at the average temperature of the sample.

2.3.3 Commercial Measurement Systems

Due to the temperature limit of the home-built measurement system, we purchased a commercial laser flash [41] system (LFA 457 Nanoflash, Netzsch Instruments, Inc.) for thermal diffusivity measurements from room temperature to 1100 ^{o}C. This system can directly measure thermal diffusivities along the out-of-plane (axial) direction of a disk sample. In contrast, bar sample measurements based on the Ångström's method give thermal diffusivities along the bar direction, i.e., the in-plane direction of a disk sample. For the same sample, we can compare the two measurements to check the thermal conductivity isotropy of TE nanocomposites. In our laser flash setup, up to three samples can be loaded for each run. If we also need to measure the specific heat along with thermal diffusivities, one of the three samples should be a standard reference sample. In this case, nanocomposite disks should have the same thickness as the standard reference disk (1 or 2 mm). The inaccuracies of the specific heat measured by the laser flash system are normally 5%. To be more accurate, we use a

commercial differential scanning calorimeter (DSC 200-F3, Netzsch Instruments, Inc.) for specific heat measurements up to 600 °C.

For Seebeck coefficient and electrical conductivity measurements, our Boston College collaborators purchased a commercial system (ZEM-3, Ulvac, Inc.) that can conduct bar sample measurements up to 1000 °C. The dc current-switching technique mentioned earlier is used for electrical conductivity measurements. For the same bar sample, the electrical properties measured by my home-built system agreed well with the results from the ZEM-3 system. The calculated power factors diverged within 3% (system errors) in the investigated 25-200 °C temperature range.

In addition to the above systems, we also purchased a 7604 Hall Effect System from Lakeshore, which exploits the van der Pauw method [42] to measure electrical conductivities and carrier concentrations from room temperature up to 500 °C for a thin disk sample. To ensure 2D electrical measurements required by data processing, the sample thickness must be at least 12-15 times smaller than its cross-section dimension according to electrical conductivity calibrations. In tests, relative errors were generally within 5% between the electrical conductivities measured with the 7604 system and those measured by the ZEM-3 system. For carrier concentration measurements, the 7604 system worked well for materials such as bismuth antimony telluride nanocomposites, with carrier concentrations on the order of 1×10^{19} cm^{-3}. However, bad repeatability was found for skutterudite nanocomposites (carrier concentrations up to 1×10^{21} cm^{-3}) because of the weak signals for high carrier concentrations. In the future, we may replace the voltmeter in the 7604 system with a nano-voltmeter to achieve better accuracies in carrier concentration measurements.

2.4 High-ZT Nanocomposites

This section is focused on two types of high-ZT nanocomposites. The P^2C device was used to hot press these nanocomposites. For BiSbTe nanocomposites (composition denoted by $Bi_xSb_{2-x}Te_3$), a peak ZT around 1.4 was achieved in samples hot pressed from nanopowders obtained by ball milling commercial BiSbTe ingots [1,3]. In comparison, the peak ZT of the state-of-art (SOA) BiSbTe ingot has remained about 1 for over 50

years. In the following work, we avoided the ingot formation step and prepared nanopowders by ball milling Bi, Sb, and Te element chunks [2,4]. A peak ZT around 1.3 was accomplished in these more cost-effective nanocomposites. The typical operation temperature of BiSbTe nanocomposites ranges from room temperature to 250 °C. For higher operation temperatures, we worked on Co_4Sb_{12}-based nanocomposites [5,6] that are mainly used for the 200-600 °C temperature range. In n-type $Yb_{0.35}Co_4Sb_{12}$ nanocomposites, a peak ZT around 1.2 was obtained at 550 °C [5].

2.4.1 P-Type Bismuth Antimony Telluride Nanocomposites

Nanopowder Preparation by High Energy Ball Milling. Nanopowders obtained by ball milling commercial BiSbTe ingots were studied in detail [1,3]. Figure 2.10 shows the x-ray diffraction (XRD) pattern of the nanopowders after ball milling (Fig. 2.10A), scanning electron microscope (SEM) image (Fig. 2.10B), and low- and high-magnification transmission electron microscope (TEM) images (Figs. 2.10C and 2.10D). The XRD patterns verify that the powder is a single phase and is well matched with those of $Bi_{0.5}Sb_{1.5}Te_3$. The broadened diffraction peaks indicates that the particles are small, which is also confirmed by the SEM image (Fig. 2.10B) and low-magnification TEM image (Fig. 2.10C). The TEM image (Fig. 2.10C) clearly shows that the nanoparticles have sizes of a few to about 50 nm with an average size of about 20 nm. High-resolution TEM (HRTEM) images (Fig. 2.10D) confirm good crystallinity of the nanoparticles and the clean surfaces that are desired for good thermoelectric properties. The inset in Fig. 2.10D also shows that some of the nanoparticles are even smaller than 5 nm.

To reduce the manufacturing cost, we also prepared nanopowders by directly ball milling appropriate amounts of elemental chunks Bi (99.999%), Sb (99.999%), and Te (99.999%) from Alfa Aesar [2,4]. Figure 2.11 shows the XRD pattern (Fig. 2.11A), SEM image (Fig. 2.11B), bright-field TEM image (Fig. 2.11C), and HRTEM image (Fig. 2.11D) of these nanopowders. The XRD pattern verifies that the powders are single phase, indicating that the mechanically assisted reaction during ball milling can make Bi, Sb, and Te element chunks into a single phase alloy. The broadened diffraction peaks indicate small particle sizes, which is also confirmed by the SEM image (Fig. 2.11B) and

low-magnification TEM image (Fig. 2.11C). The latter one shows nanoparticle sizes from 5 to 20 nm with an average value around 10 nm. The HRTEM image (Fig. 2.11D) confirms the good crystallinity of the nanoparticles and clean surfaces.

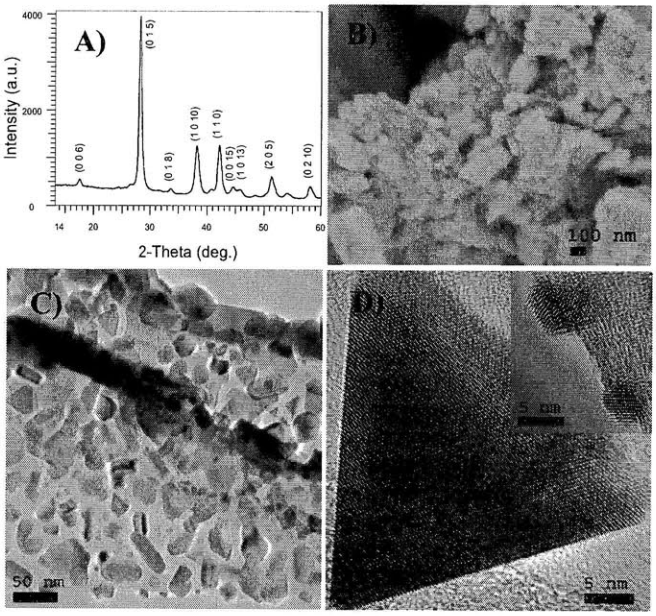

Figure 2.10 XRD (A), SEM (B), low- (C) and high- (D) magnification TEM images of an as-ball-milled nanopowder from ingots [3].

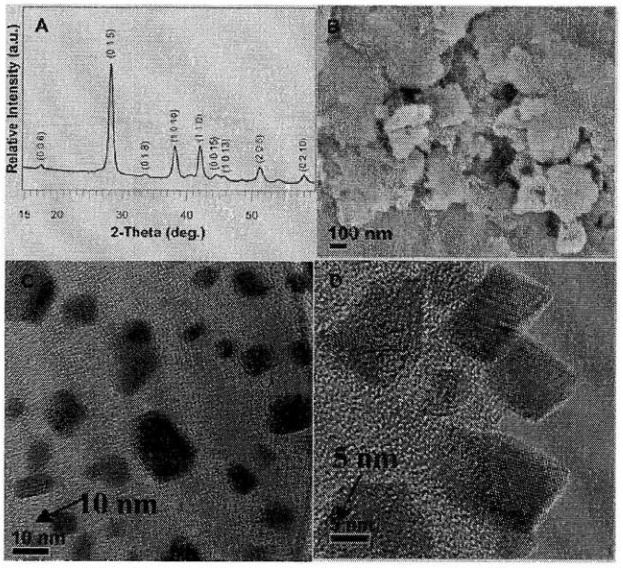

Figure 2.11 (A) XRD pattern of the nanopowders after ball milling, (B) SEM, (C) bright-field TEM image, and (D) HRTEM image of the mechanically alloyed nanopowders from elements [4].

Thermoelectric Properties of BiSbTe Nanocomposites. As mentioned earlier, single-crystal Bi_2Te_3 has a layered crystal structure and is strongly anisotropic in its transport properties [33,34]. In nanocomposites, such an anisotropy is expected to be weak due to the random crystal orientations of the nanograins. However, cautions should still be taken for ZT calculations, which should always be based on properties measured in the same direction.

For all hot-pressed nanocomposite disks, the thermal diffusivity α was first measured using our commercial laser flash system along the disk axial direction, i.e., the press direction. The specific heat C was measured with the DSC 200-F3 system. The thermal conductivity was then calculated as $k = \rho C \alpha$, where ρ is the sample density. After the measurement, bars were diced from the disks and their thermal diffusivities were measured along the bar (disk-plane) direction in my home-built system using the Ångstrom method. For a tested sample hot pressed from commercial ingot nanopowders, the thermal diffusivity values of the bar and of the disk are in agreement within 5% (Fig. 2.12), confirming the thermal isotropy of these nanocomposites [1,3]. Along the other line, samples were also cut from thick hot-pressed disks (Fig. 2.6) so that the out-of-plane direction of a sample was along the in-plane direction of a thick disk. In this way, we were able to check the in-plane-direction thermal diffusivities with the laser flash setup, which again agreed well with the above measurements [1,3].

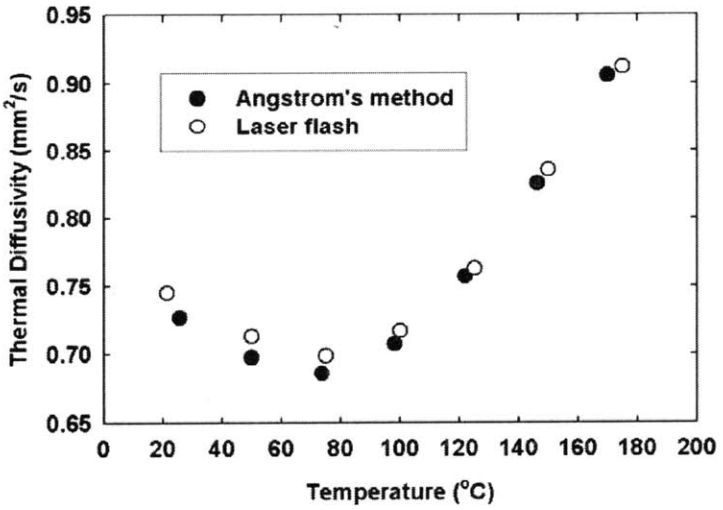

Figure 2.12 Thermal diffusivities in the disk axial direction (measured by the laser flash setup) and disk-plane direction (by my home-built system).

Electrical conductivities and Seebeck coefficients were measured on diced bar samples with the ZEM-3 system, and compared with measurements on my home-built system. The two sets of measurements were within 5% of each other. For BiSbTe nanocomposites from commercial ingots, disks and bars were cut along and perpendicular to the press direction (see Fig. 2.6) and we then performed the measurements to check their property isotropy. Although individual properties may differ by 5% within the two directions, the final ZT values are isotropic. All these measurements are repeated on more than 100 samples and the peak ZT variation is within 5%. For nanocomposites from element chunks, the same systematic measurements were carried out, which confirmed the ZT isotropy and repeatability of these nanocomposites. To test the high-temperature stability of our nanocomposites, the same samples were repeatedly measured up to 250 °C and no significant property degradation was observed. This suggests potential power generation applications may be realized for waste-heat recovery in the reported temperature range.

Figure 2.13 compares the measured thermoelectric properties of a SOA ingot, nanocomposites (NC) from commercial ingots and element chunks. Both nanocomposite samples have higher carrier concentrations (2.5×10^{19}-2.9×10^{19} cm^{-3}) than that of the SOA commercial ingot (1.8×10^{19} cm^{-3}). The behaviors of the two nanocomposites are similar. Both nanocomposites show ZT values significantly enhanced from a SOA ingot. However, the nanocomposite made from ingots systematically has lower thermal conductivities and a higher ZT than the nanocomposite from elements. This could be due to a minor micro-structural difference and lack of some additional impurity elements (Zn, Cd, etc.) [2,4].

In comparing the transport properties of nanocomposites to that of a SOA ingot, one particularly noteworthy aspect is the slow increase in the thermal conductivity above 100 °C (Fig. 2.13D), indicating suppressed bipolar contribution to the thermal conductivity [34] by thermally excited electrons and holes. The suppressed bipolar conduction in nanocomposites can also be observed from the slower decay of their power factors at elevated temperatures (Fig. 2.13C). We explain this reduced bipolar effect by assuming the existence of an interfacial potential that scatters more electrons (minority carriers) than holes [3]. The reduced bipolar effect may also be attributed to the higher

carrier concentrations in BiSbTe nanocomposites, compared with that for SOA ingots. Considering this interfacial potential, we analyzed the measured properties of nanocomposites from ingots based on the Boltzmann transport equation and the relaxation time approximation. The modeling results show that phonon contributions to the lattice thermal conductivity are reduced by a factor of two in nanocomposites from ingots (Fig. 2.14). Experimentally, the interface potential barrier height can possibly be extracted from grain interface capacitance measurements, as demonstrated in polycrystal silicon [45,46]. The extracted barrier height can be compared to the value (~100 meV) estimated from theoretically fitting measured properties. More advanced studies may also consider the charge trapping energy levels associated with grain interfaces [47-49]. Along another line, the lattice thermal conductivity can also be directly measured using a strong magnetic field H to suppress the electronic thermal conductivity k_e ($k_e \sim 1/H^2$) [50, 51].

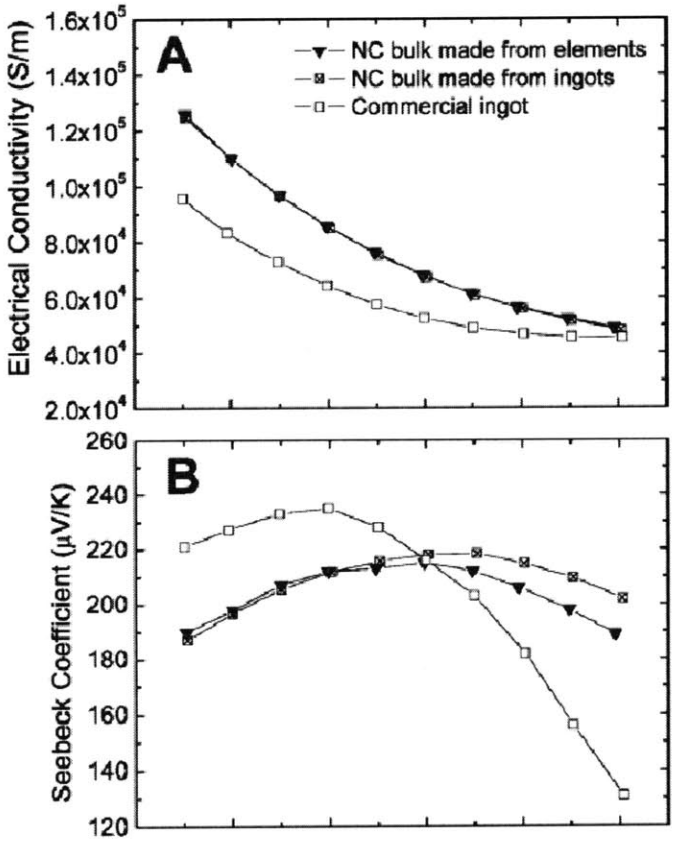

Figure 2.13 Comparison of thermoelectric properties of a SOA ingot, nanocomposites from commercial ingots [3] and element chunks [4] (to be continued).

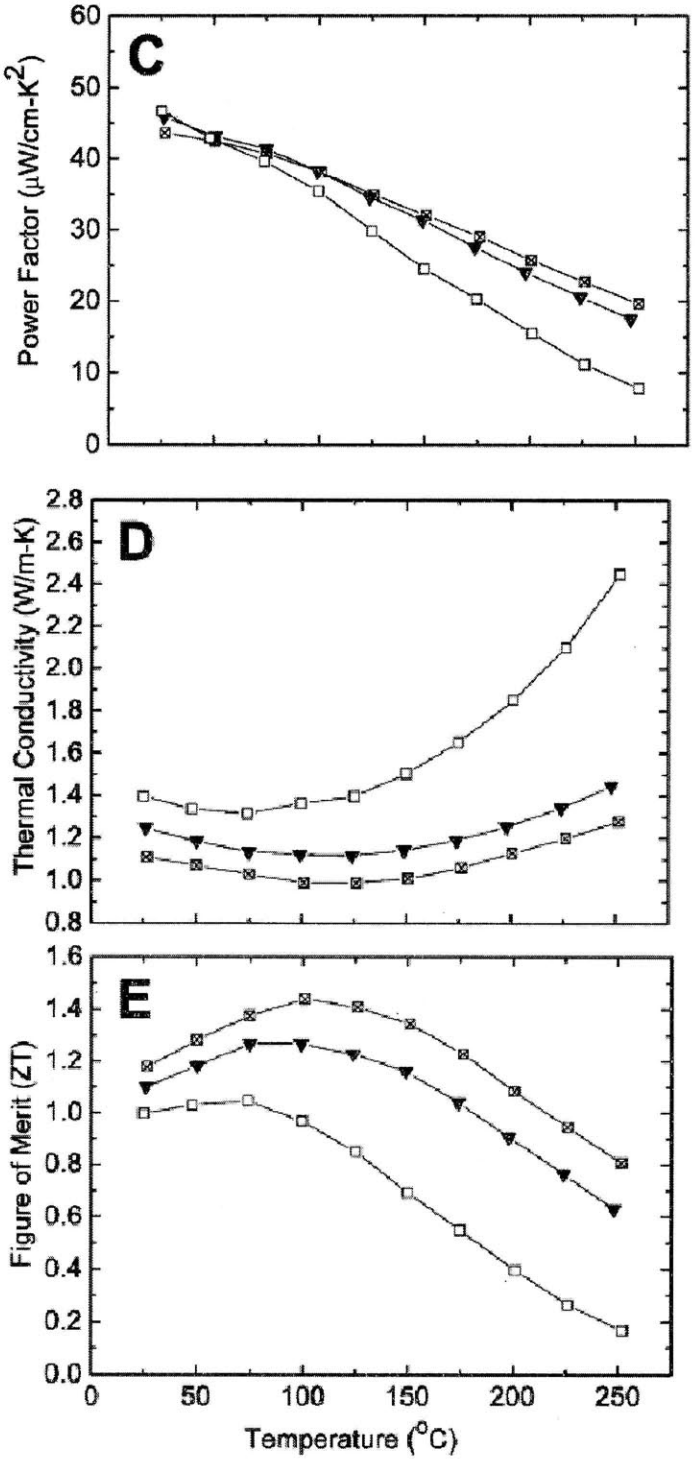

Figure 2.13 Comparison of thermoelectric properties of a SOA ingot, nanocomposites from commercial ingots [3] and element chunks [4].

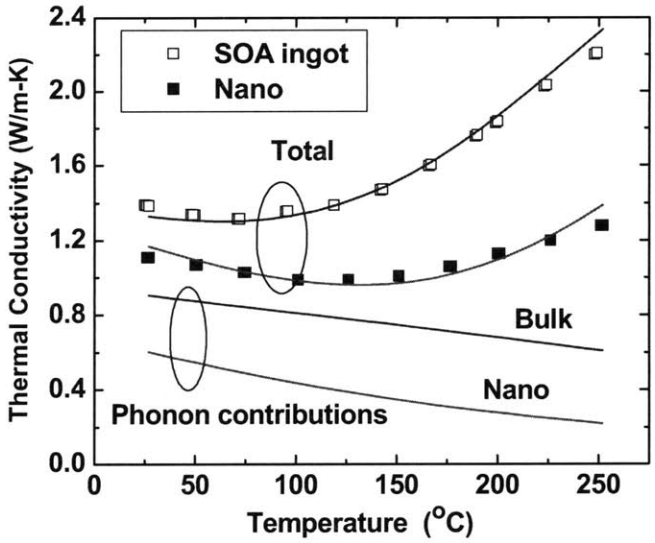

Figure 2.14 The thermal conductivity of BiSbTe nanocomposites from ingots [3]. Solid- and hollow-squares represent the experimental results for a SOA ingot and for our nanocomposites, respectively. Solid lines represent the corresponding calculations of the total and lattice part of the thermal conductivity, respectively.

Structure Studies of BiSbTe Nanocomposites. Detailed microstructure studies by a TEM were carried out on BiSbTe nanocomposites, mostly by Dr. Yucheng Lan at Boston College. Figure 2.15 shows the main structural features we observed for nanocomposites from ingots. In general, we find that most of the grains are nanosized (Figs. 2.15A and 2.15B). Furthermore, these nanograins are highly crystalline, completely random (large angles among lattice planes) with very clean boundaries, and they are very closely packed, consistent with density measurements that suggest full density (Fig. 2.15B). We also observed some larger grains as shown in Fig. 2.15C. However, under HRTEM observation, these grains consist of nanodots 2 to 10 nm in size without boundaries (Fig. 2.15D). Usually, these nanodots are Sb-rich with a typical composition close to Bi: Sb: Te = 8: 44: 48 with Sb substituting for Te. Although some of the nanodots are boundaryless with the matrix (Fig. 2.15D), we also found other nanodots making small angle boundaries with the matrix (Fig. 2.15E). In addition, we also observed pure Te precipitates of 5-30 nm (Fig. 2.15F). The selected angle electron difference (SAED) pattern (inset of Fig. 2.15F) confirms the Te phase. Generally speaking, nanodots can be found within each 50 nm diameter area. We speculate that

these nanodots could be formed during the hot-press heating and cooling processes. Similar types of nanodots have been observed in silver antimony lead telluride (LAST) alloys and were claimed to be responsible for the ZT enhancement in those alloys [19]. However, since there are so many nano interface features in our material, such as nanograins, nanodots may not be the only reason for the strong phonon scattering. We speculate that the larger-sized grains containing nanodots (Fig. 2.15C) resulted from the non-uniform milling of the ingot during ball milling. These large grains may have grown even larger during the hot-press compaction via Oswald Ripening. In this process, small grains formed initially slowly disappear, and act as "fuel" for the growth of bigger grains. More uniform nanograins during ball milling may keep these nanograins from growing during the hot-press.

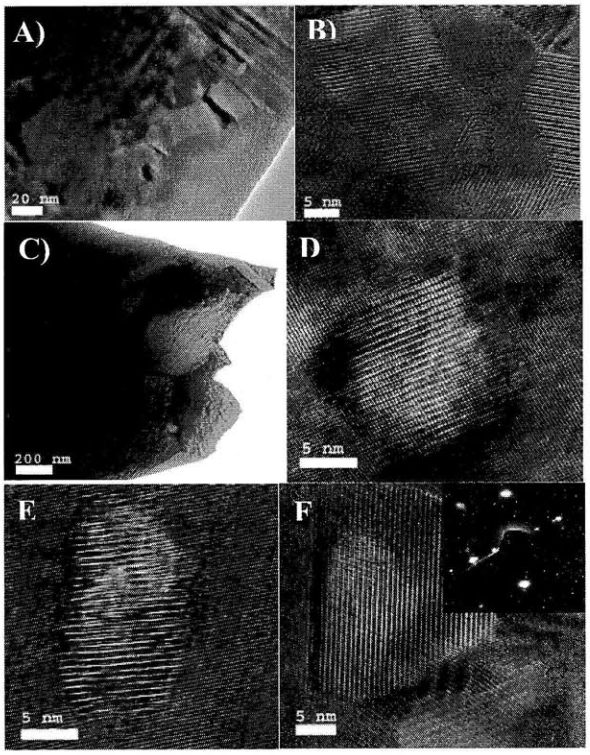

Figure 2.15 TEM images showing the microstructures of a BiSbTe nanocomposite from ingots [3]. (A) low-magnification image showing the nanograins, (B) high-magnification image showing the nanosize, high crystallinity, random orientation, and clean grain boundaries, (C) low-magnification image showing larger grains, (D) high-magnification image showing the nanodots in the matrix without boundaries, (E) high-magnification image showing the nanodots in the matrix with small angle grain boundaries, (F) high-magnification image showing Te precipitate in the matrix. SAED pattern (inset of Fig. 2.15F) shows the Te phase of the precipitated nanodot in the matrix.

A TEM investigation was also carried out for nanocomposites from elemental chunks [4]. Boundaryless nanodots (2-15 nm in sizes) and precipitates were also found in nanograins. Both the wide size distribution and the high dispersion of nanodots are favorable to the scattering of a wide phonon spectrum (mid-to-long wavelength) [52]. Instead of Te precipitates for nanocomposites from ingots (Fig. 2.15F), only Sb precipitates with sizes up to 50 nm were found in nanocomposites from elements. In addition to the possible composition difference in some minor elements (Zn, Cd, etc.), the 10% higher thermal conductivity of nanocomposites from elements may also be attributed to minor structural differences due to different precipitates. The exact cause of such precipitate changes is under investigation. More detailed structure studies of both nanocomposites can also be found elsewhere [53].

2.4.2 Co_4Sb_{12}-Based Nanocomposites

Co_4Sb_{12}-based skutterudites have been widely studied for their promising thermoelectric properties [54-56], and are regarded as potential candidates for next-generation thermoelectric materials for electrical power generation using either a solar source or waste heat. One of the remarkable features of this material is that the cage-like open structure can be filled with foreign atoms acting as phonon rattlers. Without disturbing the power factors, the "rattling" of the filled atoms scatters phonons strongly and drastically reduces the thermal conductivity of the skutterudite compounds [54-56]. Various kinds of atoms (Ce [57], La [58], Ca [59], Ba [60], Yb [61-63]) have been used to fill the cages, thereby resulting in an improved dimensionless thermoelectric figure of merit (ZT). Among these, Yb is one of the ideal filler/rattler species. Nolas *et al.* reported Yb-filled n-type $Yb_{0.19}Co_4Sb_{12}$ with a peak ZT close to 1 at 373 °C [61], and Geng *et al.* reported $Yb_{0.15}Co_4Sb_{12}$ with ZT of about 0.7 at 400 °C [62].

The conventional way of making filled skutterudite samples follows the melting of mixed elements, crystal growth, ball mill, and hot press [56, 61-63]. Similar to BiSbTe nanocomposites, we avoided the first two steps and directly ball milled element chunks into powders used for hot press. This greatly simplifies the materials synthesis process. The nano-features inside the resulting nanocomposites may further lower their thermal conductivities and thus enhance their ZTs.

In the literature for bulk $Yb_xCo_4Sb_{12}$ samples, the Yb concentration was limited to 0.19, the so-called bulk solubility, in samples prepared by melting and slow cooling [56]. However, there is one void for each Co_4Sb_{12} formula. So it should be possible to have Yb with more than 0.19. Recently, a bulk solubility of 0.29 was reported in samples made by melting and fast spin cooling with higher ZT [63], demonstrating that the bulk solubility issue is not settled in Yb-filled skutterudites, and clearly depends on the sample preparation method. In our $Yb_xCo_4Sb_{12}$ nanocomposites, we successfully increased x up to 0.5 without formation of impurity phases, much higher than the reported bulk solubility values. However, when x reaches 1, there is clearly a second phase identified by XRD, which reduces the thermoelectric performance.

$Yb_xCo_4Sb_{12}$ Nanopowder and Hot-Pressed Nanocomposites. Pure elements of Co (99.8%, Alfa Aesar), Sb (99.999%, Chengdu Chemphys Chemical Industry, China), and Yb (99.9%, Alfa Aesar) were mixed according to the stoichiometry $Yb_xCo_4Sb_{12}$ and loaded for ball milling. XRD spectra of the ball milled nanopowders indicated that the majority of the powders were not alloyed after ball milling. After the P^2C hot press, however, the obtained nanocomposite was completely transformed into a single skutterudite phase for x up to 0.5. When x = 1, an unknown second phase showed up [5].

Figure 2.16 shows the SEM images at (a) low- and (b) high-magnification of the P^2C hot pressed $Yb_{0.35}Co_4Sb_{12}$ samples that demonstrated the highest ZT among all the compositions studied. The average grain size is about 200 to 300 nm, with some big grains as large as about 1 μm. The grain growth from less than 50 nm to 200-300 nm is significant. With such large grain sizes, we do not expect a strong scattering of phonons with a mean free path shorter than 200-300 nm. Figure 2.16c shows a low magnification TEM image of a sample with the same composition $Yb_{0.35}Co_4Sb_{12}$, further indicating that the grain is about several hundred nanometers in size, consistent with the SEM observation. The high resolution TEM image shown in Fig. 2.16d confirms the excellent crystallinity, clean grain boundary, and a large angle grain boundary. The excellent crystallinity and clean grain boundaries are needed for achieving good electrical transport properties, whereas the large angle grain boundary can potentially benefit phonon scattering.

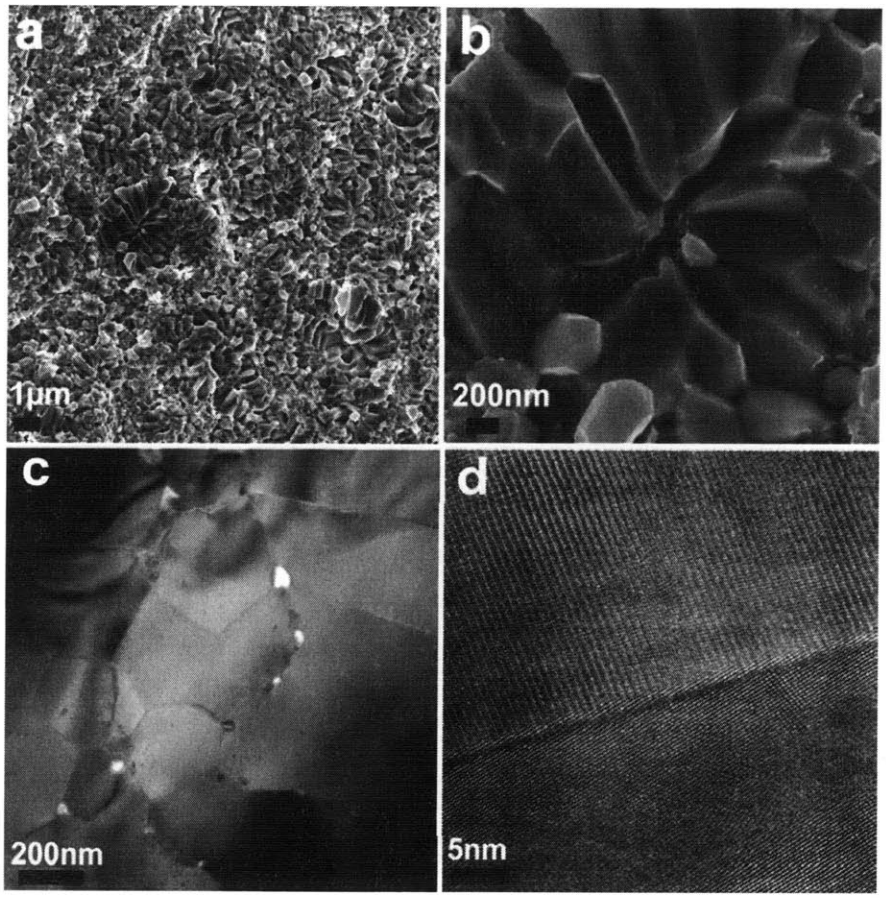

Figure 2.16 SEM images at (a) low- and (b) high-magnification and TEM images at (c) low- and (d) high-magnification of P^2C hot pressed skutterudite $Yb_{0.35}Co_4Sb_{12}$ bulk samples, showing the high crystallinity, clean grain boundaries, and larger angle grain boundary [5].

Thermoelectric Properties of $Yb_xCo_4Sb_{12}$ Nanocomposites. As BiSbTe nanocomposites, disks and bars were cut and polished for thermoelectric property characterization. Figure 2.17 shows the carrier concentrations and Hall mobilities of samples with x up to 0.5 at room temperature as a function of Yb content. The carrier concentration for $Yb_xCo_4Sb_{12}$ shows a linear relation with the Yb filling fraction x. The Hall mobilities drop with higher Yb filling fraction, which could be due to the increased electron-electron and electron-phonon scattering by higher electron concentrations. However, the carrier concentration increase is much larger that the carrier mobility decrease, which is why the electrical conductivity increases with Yb content.

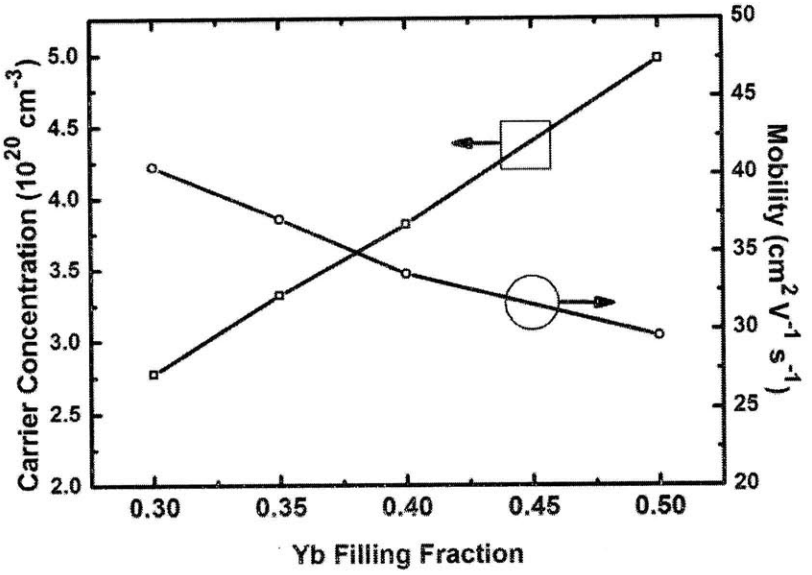

Figure 2.17 Room temperature carrier concentration and Hall mobility of $Yb_xCo_4Sb_{12}$ bulk samples with x = 0.3, 0.35, 0.4, and 0.5 [5].

The temperature dependent thermoelectric properties of $Yb_xCo_4Sb_{12}$ are plotted in Fig. 2.18. Fig. 2.18a shows that the electrical conductivity σ of all samples decreases with an increase in temperature T. Also σ increases with increased Yb content. The negative Seebeck coefficients (Fig. 2.18b) indicate that electrons are the dominant carriers. Samples with different Yb content show a similar T dependence trend for the Seebeck coefficient from room temperature to 550 °C, with the maximum Seebeck coefficient occurring at 550 °C. The absolute value of the Seebeck coefficient decreases with increasing x at the same temperature, consistent with the electrical conductivity increase with increasing x. This behavior may be due to the increase in the electron concentration.

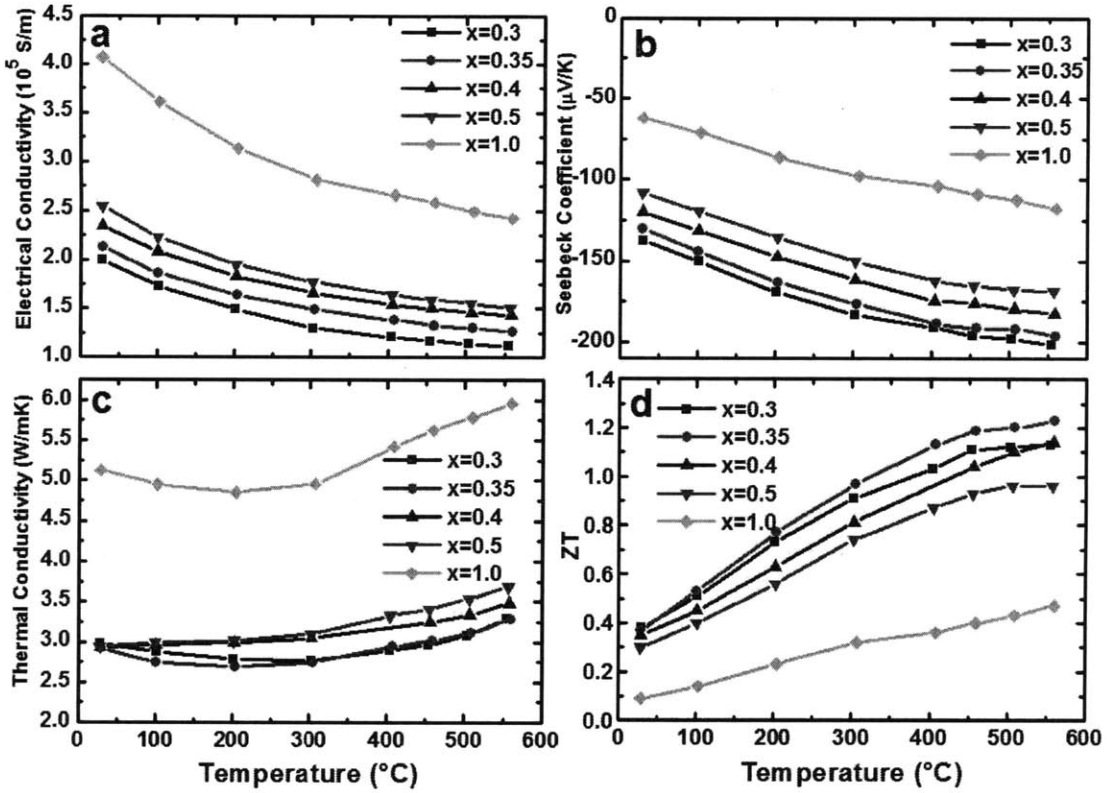

Figure 2.18 Temperature-dependent electrical conductivity (a), Seebeck coefficient (b), thermal conductivity (c), and ZT (d) of DC hot pressed skutterudite $Yb_xCo_4Sb_{12}$ bulk samples with x = 0.3, 0.35, 0.4, 0.5, and 1.0 [5].

The thermal conductivity of the samples is shown in Fig. 2.18c. For the samples with x = 0.3 and 0.35, the thermal conductivity values decrease with increasing T and reach a minimum at 300 °C and then k increases rapidly with increasing T due to bipolar effect that is mentioned for Figs. 2.13 and 2.14, and will be explained in Eq. (3-25). For the samples with x = 0.4 and 0.5, the thermal conductivity keeps rising all the way from room temperature to 550 °C, which can be attributed to the significant increase of k_e at elevated temperatures. Although higher Yb concentrations increase the electron contribution to the total thermal conductivity, Yb can also decrease the lattice contribution by the rattling effect. In our tests, $Yb_{0.35}Co_4Sb_{12}$ has an optimized lowest thermal conductivity with a minimum of 2.7 W/m·K, which leads to the highest observed ZT value among all the samples studied.

Figure 2.18d shows the temperature dependent ZT from room temperature to 550 °C. ZT increases with temperature and reaches a maximum at around 550 °C. The highest ZT is observed for the $Yb_{0.35}Co_4Sb_{12}$ sample with its maximum value of about 1.2 occurring at 550 °C. This is one of the highest ZT values reported for n-type filled skutterudites made by first ingot formation followed by grinding and hot pressing [61-65].

2.5 Device Cooling Test

As mentioned before, ZTs calculated from measured σ, k, S values can easily have a 10-20% error due to measurement errors in individual properties. As an independent checking method, direct ZT evaluation using Harman's technique [34] also has an inaccuracy around 20% [66]. Because of uncertainties in the above measurements, device performance test is regarded as the most dependable way of confirming high ZT values. It is also an important step towards real-world applications.

To verify the high ZT achieved in BiSbTe nanocomposites from ingots, device cooling tests were conducted on home-made unicouples [3]. With identical commercial n legs, the p leg of one unicouple used a nanocomposite sample, while the other comparison unicouple used a commercial p leg. For hot side temperatures fixed at 50, 100, and 150 °C, the unicouple with a nanocomposite p leg always yielded better cooling performance and the results were consistent with the theoretical prediction based on measured temperature-dependent thermoelectric properties of both legs.

2.5.1 Principle of the Cooling Test

For a TE device, the dimensions of both legs should be matched to maximize the effective ZT of the device. Assuming temperature-independent material properties, the Z value averaged over both legs is maximized as [34]

$$\langle Z \rangle = \frac{(S_h - S_e)^2}{\left[(k_h \rho_h)^{1/2} + (k_e \rho_e)^{1/2} \right]^2}, \tag{2-3}$$

when the dimensions satisfy

$$\frac{L_e A_h}{L_h A_e} = \sqrt{\frac{\rho_h k_e}{\rho_e k_h}}, \tag{2-4}$$

in which L is leg length, A is its cross sectional area, S is again the Seebeck coefficient, k is the thermal conductivity, ρ is the electrical resistivity, and subscripts h and e indicate the p leg and the n leg, respectively.

Under the cooling mode (see Chap. 1), the current injection can be optimized to achieve a maximum temperature difference for a fixed hot side temperature T_h. At a current of $I_{opt} = (S_h - S_e)T_c / R$, ΔT reaches it maximum value at [34]

$$\Delta T_{\max} = T_h - T_c = \frac{1}{2}\langle Z \rangle T_c^2, \tag{2-5}$$

where R is the total electrical resistance of both legs, and the minimum cold side temperature T_c can be solved assuming a given T_h. It is evident that $\Delta T_{\max}$ monotonically increases with $\langle Z \rangle$. For cases with a large ΔT, we can no longer assume constant material properties and temperature-dependent properties for both legs must be included into the calculations. Nevertheless, a larger $\Delta T_{\max}$ always indicates a higher effective ZT of a TE device. In our tests, $\Delta T_{\max}$ is normally at least tens of degrees centigrade, while typical reading inaccuracies of thermocouples are less than 1 °C. The measurement error in $\Delta T_{\max}$ is clearly negligible for ZT confirmation purposes, and this is why device cooling tests are regarded as one of the most dependable methods to verify ZT values and check the property measurements.

2.5.2 Experimental Setup

Figure 2.19 shows the experiment setup of the device cooling test [3]. A pair of p- and n-type legs is soldered onto two 6.5-mm-thick copper blocks. On the top, the two TE legs are electrically connected by a thin copper plate with soldering. In all measurements, the copper blocks are used as the hot side and their temperatures are stabilized by controlling the temperature of the cold finger in the commercial cryostat chamber. For T_h and T_c readings, thermocouples are soldered into holes drilled on two copper blocks and the top copper plate. In tests, currents up to 10 A will pass the device

and this may introduce a dc voltage drop added to thermocouple Seebeck voltages. To avoid possible temperature reading errors, all thermocouples are positioned to be away from the current path, indicated by the arrows in Fig. 2.19.

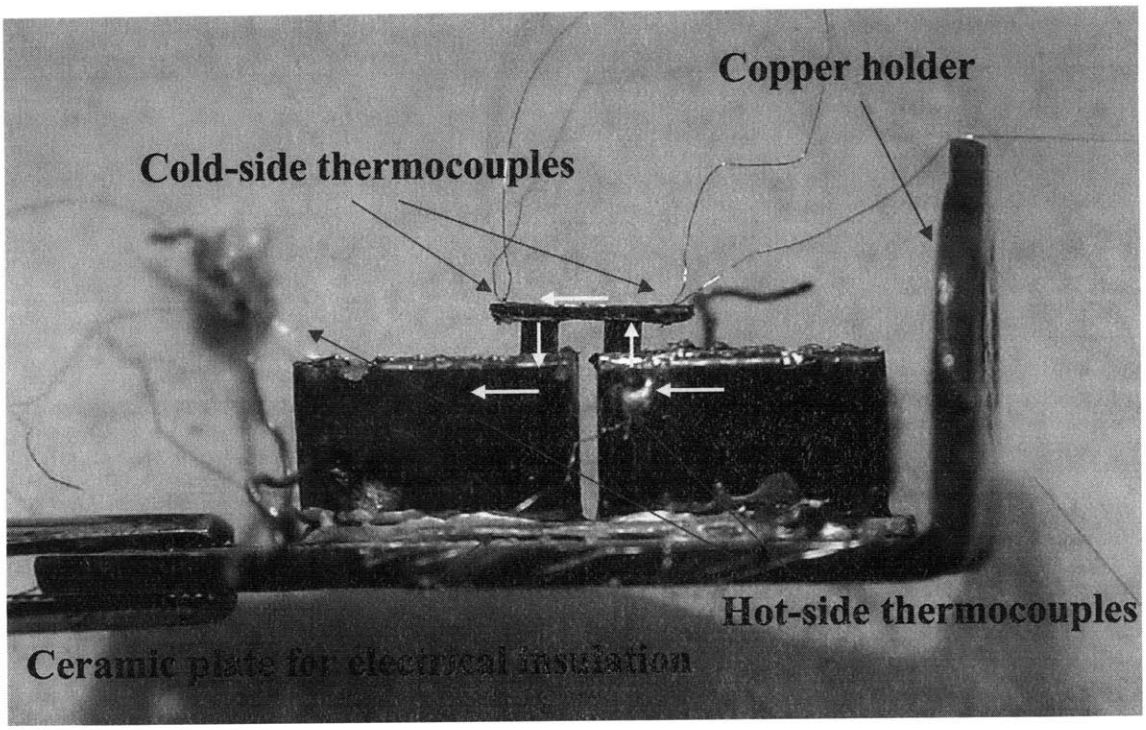

Figure 2.19 Experimental setup of the device cooling test [3]. Two thermoelectric legs (p leg on the left, n leg on the right) were soldered onto 6.5-mm-thick copper blocks and then bridged by a top copper plate. Two cold-side thermocouples were soldered into small holes drilled on both ends of the top copper plate. Hot-side thermocouples were soldered on the edge of each copper block. The injected current direction is indicated by arrows. The unicouple is glued onto a ceramic plate that is further glued onto a copper holder. In measurements, the copper holder will be screwed onto the cold finger inside a commercial cryostat chamber.

For TE device construction, one challenge is to get good electrical contacts on soldered junctions on the cold and hot sides. Otherwise, Joule heating generated on these junctions will significantly deteriate the device performance. For commercial Bi_2Te_3-based legs, a nickel layer is electrolessly plated as a metallization for soldering. The nickel layer not only functions as a diffusion barrier to prevent solder contamination but also ensures small electrical contact resistance for junction soldering. Although the same technique may be applied to nanocomposites, we succeeded in hot pressing nanopowders

sandwiched by two nickel thin films so that the hot-pressed disk will have nickel layers on its top and bottom surfaces before cutting into legs. In tests, similar electrical contacts can be obtained by this simple approach, but cautions should be taken for nickel film oxidation during hot press. For currently developed n-type $Bi_2Se_xTe_{3-x}$ samples, we should also pay attention to leg property changes due to nickel diffusion into $Bi_2Se_xTe_{3-x}$ [67] at high hot press temperatures. Along the other line, nickel layers with even better adhesion were obtained by chemical mechanical polishing of a disk plus nickel deposition by sputtering.

2.5.3 Temperature Profile Calculation

As the temperature difference across a TE device becomes large, the usual assumption of temperature-independent properties will not be valid. In analysis we have to consider temperature-dependent properties of both legs. Assuming 1D current flow, the governing equations include the definition of heat flux [34]

$$q(x) = -k(x)\frac{dT}{dx} + J \cdot S(x) \cdot T, \tag{2-6}$$

and the Domenicali's equation of energy balance

$$\frac{d}{dx}\left(k(x)\frac{dT}{dx}\right) = -Q'''(x) = JT\frac{dS(x)}{dx} - \frac{J^2}{\sigma(x)}, \tag{2-7}$$

where q is the local heat flux at position x, $Q'''(x)$ is the volumetric heat generation rate, J is the current density, and S, k, σ are evaluated according to the local temperature $T(x)$ and the measured temperature dependence of each property. The first term on the right hand side of Eq. (2-6) corresponds to heat conduction, whereas the second term is the heat carried by an electrical current. In Eq. (2-7), the first term on the right hand side is related to the Thomson effect [34] and the second term is from Joule heating. To simplify the computation, we can further convert the two governing equations to two first-order equations as [68]

$$\frac{dT}{dx} = \frac{JS(x)T - q(x)}{k(x)},$$

$$\frac{dq(x)}{dx} = \rho(x)J^2[1 + ZT(x)] - \frac{JS(x)q(x)}{k(x)}. \tag{2-8}$$

In calculations, we assume that the bottom ends of two legs (Fig. 2.19) share the same T_h because of the high thermal conductance of the underneath ceramic plate and copper holder. Similarly, the same T_c is assumed on the top of both legs, i.e., temperature continuity from the n-leg top to the p-leg top. Despite the large ZT imbalance between a nanocomposite p leg and a commercial n leg at elevated temperatures, thermal analysis suggests that the temperature variation across the top copper plate is still within 0.5 °C. This is consistent with the T_c and T_h measurements with four thermocouples, where the difference between the same side thermocouples can be less than 1 °C with carefully mounted thermocouples. Due to the negligible Joule heating and radiation loss on the top copper plate, we also assume that heat flow is conserved from the top end of the n leg to that of the p leg, i.e., continuity of heat flow. Basically we consider a one-dimensional system with p and n sections. Both ends of the system are fixed at T_h, while the two sections are joint with continuous temperature (T_c at the joint point), heat flow, and current flow.

With the above governing equations and boundary conditions, the temperature profiles along both legs are calculated through a trial-and-error process for specified T_h and injected current. The calculated temperature profile is used to re-evaluate all local properties. Convergence is achieved until the recomputed temperature profile is no longer changed.

2.5.4 Thermoelectric Compatibility

To obtain good device performance, only having a high ZT is not enough. For both cooling and power generation modes, we need to adjust the current density J inside each leg to make full use of their ZT values. As an example, $\Delta T_{\max}$ in Eq. (2-5) is achieved for optimized J values in both legs. When the temperature difference across a TE device is large, the local current density also needs to be optimized to assure efficient operations at different locations along a TE leg. Although J can be matched between two legs with different cross sectional areas, in typical TE devices we do not adjust J along an individual TE leg for different ΔT. Limited freedom of such optimization is available and legs with operation performance insensitive to J are always preferred.

We start the analysis with the power generation mode. Similar results are anticipated for the cooling mode. For the power generation mode, a TE leg can be divided into infinitely short segment, viewed as heat engines connected in series. For one of such segments, its maximum power generation efficiency is the Carnot efficiency, $\eta_c = (T_h - T_c)/T_h$, where T_c and T_h are the hot- and cold-end temperatures of this segment, respectively. We can further define a reduced efficiency as the efficiency normalized by η_c, i.e., $\eta_r = \eta/\eta_c$. In the limit $T_h - T_c \to 0$, Snyder and Ursell showed [69]

$$\eta_r = \frac{u\frac{S}{Z}\left(1 - u\frac{S}{Z}\right)}{u\frac{S}{Z} + \frac{1}{ZT}}, \tag{2-9}$$

in which $u = J/k\nabla T$ (current flux over heat flux), S is Seebeck coefficient, Z is again $S^2\sigma/k$. For the SOA ingot and BiSbTe nanocomposites made from ingots, we plot the reduced efficiency as a function of u (Fig. 2.20) with properties at 50, 100, 150 °C. Compared to the SOA ingot, our nanocomposites not only have a higher peak η_r at all temperatures but also maintain a high η_r over a much wider u range. Consequently, it is easier to match a nanocomposite leg with a given n leg in their geometries for better device performance.

The u maximizing η_r is defined as the thermoelectric (power generation) compatibility factor [69]. The new material property is given as

$$s_c = \frac{\sqrt{1+ZT} - 1}{ST}. \tag{2-10}$$

For efficient operations of a TE unicouple, we should assure that local u is close to s_c in both legs. For device-design purposes, Eq. (2-4) is still widely used instead of Eq. (2-10) to match p and n legs. In Eq. (2-4), Seebeck coefficients will not influence the dimension match but it appears in the optimized current I_{opt} expression later to affect the optimized J (or u) values.

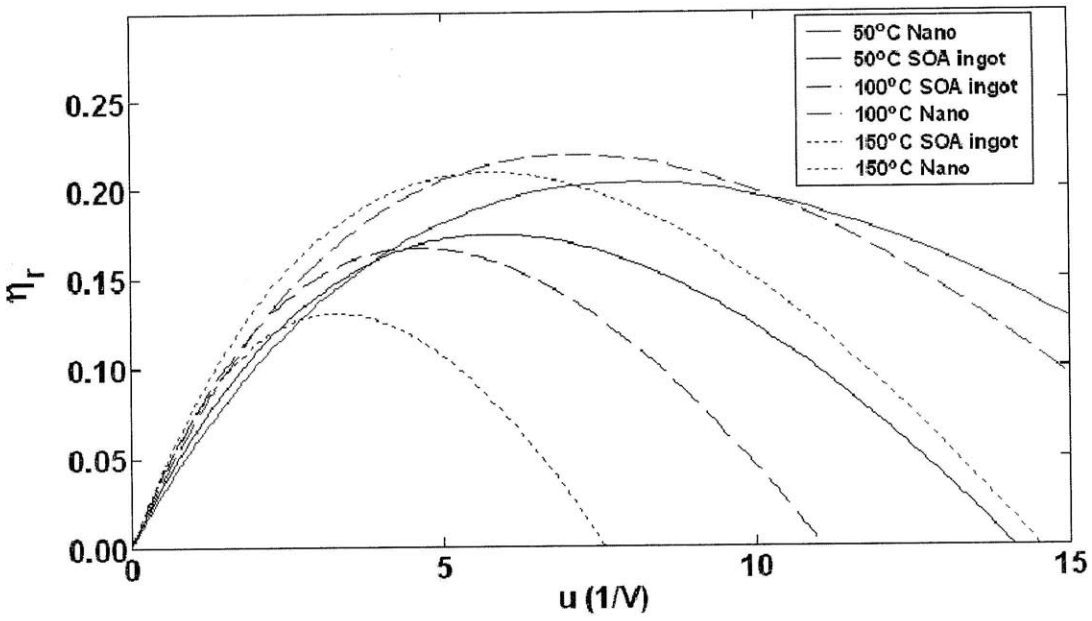

Figure 2.20 Reduced efficiency as a function of $u = J / k\nabla T$.

2.5.5 Cooling Test Results and Discussion

For three hot side temperatures (50, 100, 150 °C), the obtained ΔT is measured as a function of the injected current. All tests are conducted under a vacuum level of around 10^{-3} torr by a mechanical pump. By a combination of a heater and a continuous flow of liquid nitrogen, the hot side temperature (thermally grounded to the cold finger) is controlled within a 1.5 °C variation from set points. For all injection currents, data are taken after the fluctuation of ΔT is less than 0.5 °C. Measurements for the same T_h were successfully repeated on different days. Figure 2.21 shows the results at T_h=100 °C for the unicouple consisting of a nanocomposite p leg and a commercial n leg, with data taken from repeated measurements. The measured temperature differences agree well with the theoretical prediction based on temperature-dependent properties of both legs. For a theoretical analysis, the measured properties of the n leg are given by Figs. 2.22A-D, whereas the nanocomposite leg properties are already plotted in Fig. 2.13. In Fig. 2.23, the measured ΔT_{max} for two unicouples are plotted in comparison. Our nanocomposite p leg consistently produced larger ΔT_{max} for the tested T_h values.

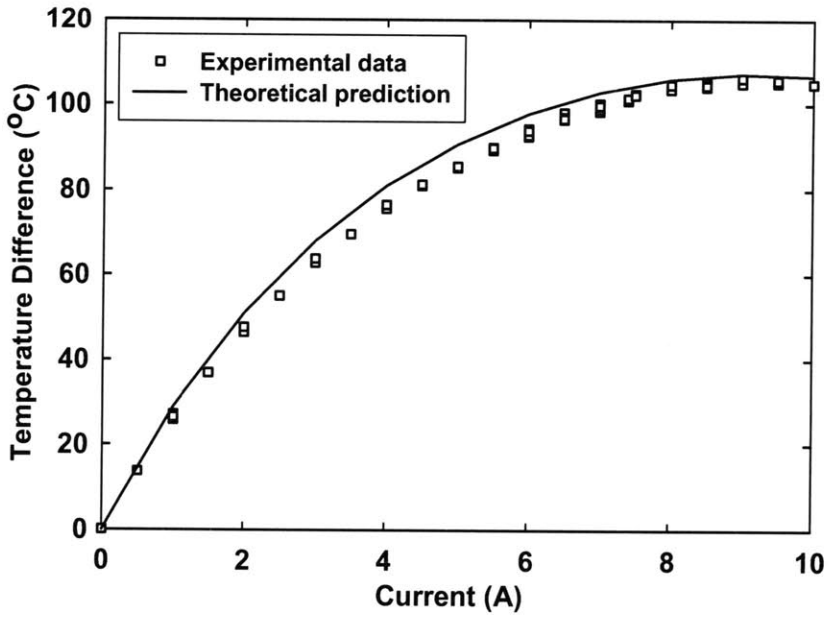

Figure 2.21 Cooling test results with the hot side fixed at 100 °C for a unicouple using a nanocomposite p leg and a commercial n leg.

It should be noted that the obtained ΔT_{max} only corresponds to an averaged $Z\overline{T}$ from 0.86 to 0.96 for the three tested hot-side temperatures, in which $\overline{T}=(T_h+T_c)/2$. This is because the n leg used here only had a peak ZT around 0.86 at 77 °C (Fig. 2.22D), which strongly limited the $\langle Z \rangle$ value in Eq. (2-3). A higher ΔT_{max} value is anticipated if a better n leg can be utilized to match p-type nanocomposites. Therefore, it is important to develop n-type Bi_2Te_3-based nanocomposites that could make full use of our high-ZT p legs for better device performance.

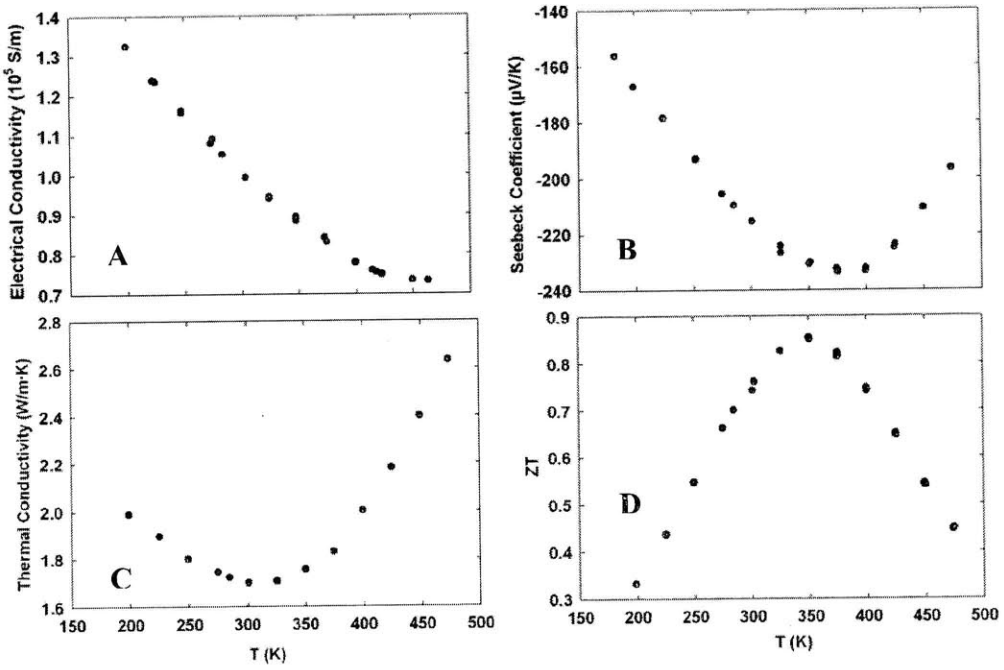

Figure 2.22 Thermoelectric properties of the commercial n leg. Thermal conductivities were measured based on one-dimensional heat conduction along an n leg in good vacuum [34]. Because of the small aspect ratio of the leg, the influence of side wall radiation loss was estimated to be less than 5% and this loss decreases with reduced temperatures.

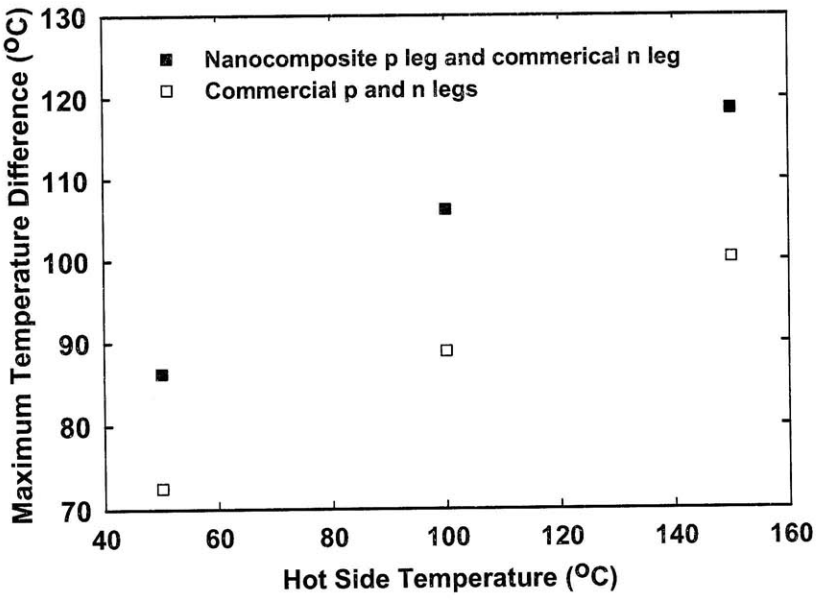

Figure 2.23 Comparison of ΔT_{max} of two unicouples with hot-side temperatures set at 50°, 100°, and 150 °C.

2.6 Annealing Effects on ZT of BiSbTe nanocomposites

One important topic of material science research is to improve material properties by post processes such as annealing. For a p-type $Bi_{0.4}Sb_{1.6}Te_3$ nanocomposite made from element chunks, I found that its peak ZT can be increased from 1.22 at 100 °C to 1.37 at 75 °C (Fig. 2.24D) by baking it overnight at 250 °C and then cooling down to room temperature, all under an Ar flow. The significant ZT enhancement is due to the apparent thermal conductivity reduction (Fig. 2.24A) after the 250 °C anneal. The power factor $S^2\sigma$ was reduced by less than 4% at all temperatures. Although this variation is within measurement errors, the carrier concentration was decreased after annealing, which can be observed from the increased Seebeck coefficient (Fig. 2.24B) and reduced electrical conductivity (Fig. 2.24C) at room temperature. The observed thermal conductivity reduction (~ 0.15 W/m·K at room temperature) resulted from the decrease of both the lattice thermal conductivity k_L and the electronic thermal conductivity k_e. The latter one was estimated to be only 0.036 W/m·K according to the Wiedemann-Franz law [34], $k_e = L\sigma T$, in which the metallic Lorentz number L =2.4×10^{-8} WΩK^{-2} was used. Apparently the reduction in k_L was the main cause of the observed ZT enhancement. Other annealing tests in either Ar or air also yielded reduced carrier concentrations and thermal conductivities. However, the peak ZT was not always improved because the power factor was reduced too much in some cases (up to 15%). For air conditioning and refrigeration applications, a higher ZT close to room temperature is always preferred. It is worth investigating such annealing effects in details in the future.

In the literature, reduced electrical conductivities after annealing were reported for $Bi_{0.5}Sb_{1.5}Te_3$ polycrystals but other TE properties were not measured [70]. Such property changes were attributed to Te precipitates formed during the fast cooling, which is a non-equilibrium process. In such a non-equilibrium process, Te shows retrograde solid solubility in $Bi_{0.25}Sb_{0.75}Te$ (Fig. 2.25) and thus precipitates out in the main phase [71]. Similar to grain interfaces, it seems that these precipitates scatter phonons much stronger than charge carriers in BiSbTe nanocomposites. Along this line, we may improve sample properties by creating more Te precipitates with an annealing-cooling process.

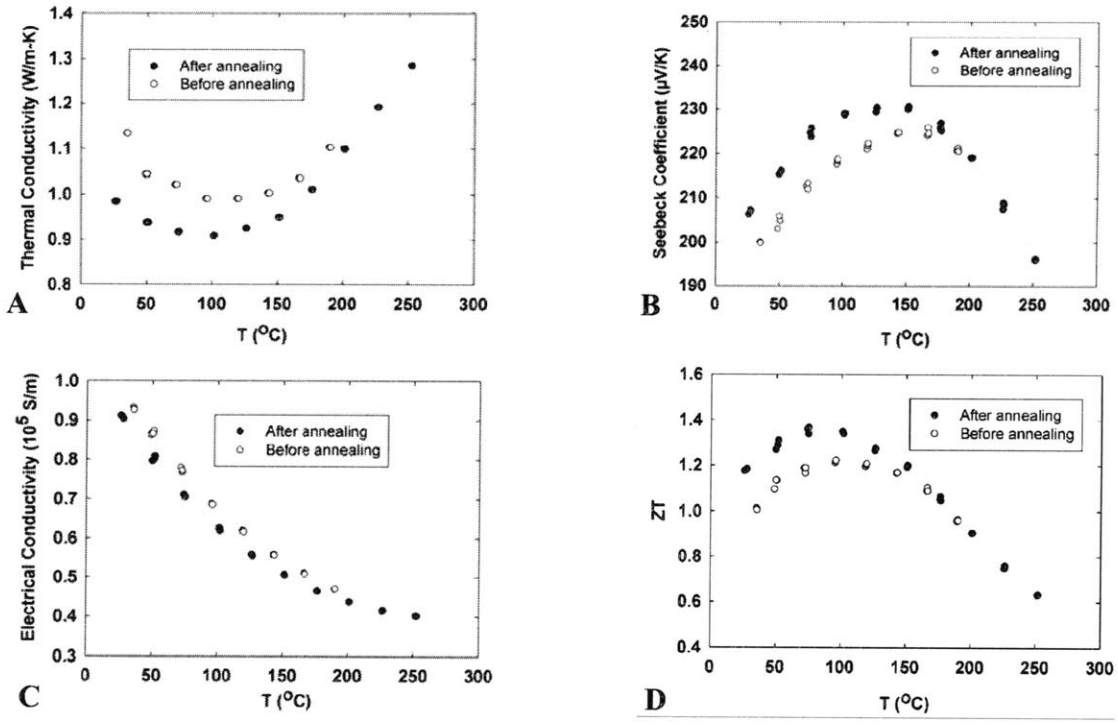

Figure 2.24 Properties of a $Bi_{0.4}Sb_{1.6}Te_3$ nanocomposite sample before and after 250 °C annealing under an Ar flow.

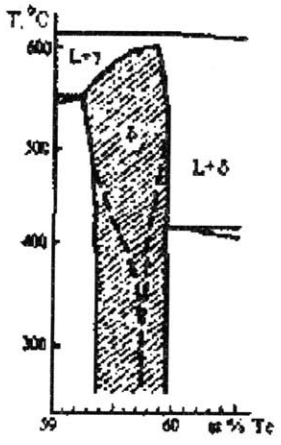

Figure 2.25 Phase diagram of the $Bi_{0.25}Sb_{0.75}Te$ composition, which is close to the $Bi_{0.5}Sb_{1.5}Te_3$ composition of nanocomposites. Tellurium solubility in equilibrium alloys is given by the continuous line, while non-equilibrium alloys show retrograde Te solubility (dashed line) [71].

For nanocomposites made from element chunks, we started with the furnace hot press setup (refer to Fig. 2.4) before switching to the P^2C hot press. In general, the

former one yielded much larger grains (up to 1 μm) because grains had enough time to grow up during the much longer hot press period (30 min to 1 hr versus a few minutes for P^2C hot press). Surprisingly, we found that the lattice thermal conductivities of furnace-hot-press samples were still comparable to P^2C samples. This may indicate that nano-features such as precipitates contribute significantly to the observed thermal conductivity reduction, in addition to the grain interface scattering of phonons. The typical spacing between observed precipitates is 50-100 nm. For pure Bi_2Te_3 or Sb_2Te_3, the phonon mean free paths (MFPs) averaged among all directions and frequencies are ~30 nm [72]. Due to strong alloy scattering, the averaged phonon MFP in $Bi_{0.4}Sb_{1.6}Te_3$ alloys is expected to be even shorter. Using such a short averaged MFP, we cannot explain the significant thermal conductivity reduction caused by nano-sized precipitates in frequency-independent Monte Carlo simulations. When frequency-dependent phonon MFPs are available for these materials, frequency-dependent Monte Carlo simulations should be carried out to check the exact influence of precipitates on the phonon transport. More accurate analysis may further consider the change of frequency-dependent phonon MFPs and even phonon dispersions inside nanograins due to their structure differences from bulk counterpart materials. In addition, detailed microstructure studies and systematic tests should also be conducted to better understand what happens to our samples.

2.7 Conclusions

This chapter introduces the essential experimental parts of my TE nanocomposite research. The effectiveness of this approach was successfully demonstrated in two types of TE composites: nanostructured $Bi_xSb_{2-x}Te_3$ bulk alloys [1-4] and $Yb_xCo_4Sb_{12}$ nanocomposites [5]. Room for further improvement is still available with deeper understanding of electron and phonon transport processes inside these nanocomposites, especially across grain interfaces. As an integrated thesis, the following chapters will focus on theoretical studies of electron and phonon transport phenomena. Advancement in the theoretical aspects could significantly help the future development of TE nanocomposites.

2.8 References

[1] B. Poudel, *A Study on Thermoelectric Properties of Nanostructured Bulk Materials*, Ph.D. thesis, Boston College, 2007. Department of Physics.

[2] Y. Ma, *Thermoelectric Properties of P-Type Nanostructured Bismuth Antimony Tellurium Alloys Bulk Materials*, Ph.D. thesis, Boston College, 2009. Department of Physics.

[3] B. Poudel, Q. Hao, Y. Ma, Y. C. Lan, A. Minnich, B. Yu, X. Yan, D. Z. Wang, A. Muto, D. Vashaee, X. Y. Chen, J. M. Liu, M. S. Dresselhaus, G. Chen, and Z. F. Ren, *Science* **320**, 634 (2008).

[4] Y. Ma, Q. Hao, B. Poudel, Y. C. Lan, B. Yu, D. Z. Wang, G. Chen, and Z. F. Ren, *Nano Lett.* **8**, 2580 (2008).

[5] J. Yang, Q. Hao, H. Wang, Y. C. Lan, Q. Y. He, A. Minnich, D. Z. Wang, J. A. Harriman, V. M. Varki, M. S. Dresselhaus, G. Chen, and Z. F. Ren, *Phys. Rev. B* **80**, 115329 (2009).

[6] Q. Y. He, Q. Hao, X. W. Wang, J. Yang, Y. C. Lan, X. Yan, B. Yu, Y. Ma, B. Poudel, G. Joshi, D. Z. Wang, G. Chen, Z. F. Ren, *J. Nanosci. Nanotech.* **8**, 4003 (2008).

[7] L. D. Hicks and M. S. Dresselhaus, *Phys. Rev. B* **47**, 16631 (1993).

[8] R. Venkatasubramanian, E. Siivola, T. Colpitts, and B. O'Quinn, *Nature* **413**, 597 (2001).

[9] T. C. Harman, P. J. Taylor, M. P. Walsh, and B. E. LaForge, *Science* **297**, 2229 (2002).

[10] G. Chen, *Phys. Rev. B* **57**, 14958 (1998).

[11] M. S. Dresselhaus, G. Chen, M. Y. Tang, R. G. Yang, H. Lee, D. Z. Wang, Z. F. Ren, J.-P. Fleurial, P. Gogna, *Adv. Mater.* **19**, 1043 (2007).

[12] G. Chen and R.G. Yang, *Materials Integration* **18**, special issue (2005).

[13] G. Chen, *Semiconduct. Semimet.* **71**, 2003 (2001).

[14] R.G. Yang and G. Chen, *Phys. Rev. B* **69**, 195316 (2004).

[15] M. S. Jeng, R. G. Yang, D. Song, and G. Chen, *ASME J. Heat Transfer* **130**, 042410 (1-11) (2008).

[16] N. Scoville, C. Bajgar, J. Rolfe, J.P. Fleurial, and J. Vandersande, *Nanostructured Materials* **5**, 207-223 (1995).

[17] X. B. Zhao, X. H. Ji, Y. H. Zhang, T. J. Zhu, J. P. Tu, and X. B. Zhang, *Appl. Phys. Lett.* **86**, 062111 (2005).

[18] J. R. Sootsman, R. J. Pcionek, H. Kong, C. Uher, and M. G. Kanatzidis, *Chem. Mater.* **18**, 4993 (2006).

[19] K. F. Hsu, S. Loo, F. Guo, W. Chen, J. S. Dyck, C. Uher, T. Hogan, E. K. Polychroniadis and M. G. Kanatzidis, *Science* **303**, 818 (2004).

[20] J. Androulakis, C. H. Lin, H. J. Kong, C. Uher, C. I. Wu, T. Hogan, B. A. Cook, T. Caillat, K. M. Paraskevopoulos and M. G. Kanatzidis, *J. Am. Chem. Soc.* **129**, 9780 (2007).

[21] P. F. P. Poudeu, J. D'Angelo, A. D. Downey, J. L. Short, T. P. Hogan and M. G. Kanatzidis, *Angew. Chem., Int. Ed.* **45**, 3835 (2006).

[22] J. R. Sootsman, J. Q. He, V. P. Dravid, S. Ballikaya, D. Vermeulen, C. Uher and M. G. Kanatzidis, *Chem. Mater.* **22**, 869 (2010).

[23] Y. L. Li, J. Jiang, G. J. Xu, W. Li, L. M. Zhou, Y. Li and P. Cui, *J. Alloy Compd.* **480**, 954-957 (2009).
[24] X. L. Xin, Y. Jiang, D.X. Kong, H. H. Zhong, L. Chen, D. B. Yu, *Phys. Status Solidi (a)* **207**, 163 (2010).
[25] Q. Zhang, J. He, T. J. Zhu, S. N. Zhang, X. B. Zhao, and T. M. Tritt, *Appl. Phys. Lett.* **93**, 102109 (2008).
[26] J. L. Mi, X. B. Zhao, T. J. Zhu, and J. P. Tu, *Appl. Phys. Lett.* **91**, 172116 (2007).
[27] J. L. Mi, X. B. Zhao, T. J. Zhu, and J. P. Tu, *J. Phys. D: Appl. Phys.* **41**, 205403 (2008).
[28] D. M. Rowe, Ed. *CRC Handbook of Thermoelectrics* (CRC, Boca Raton, FL, 1995).
[29] N. Okinaka and T. Akiyama, *Jpn. J. Appl. Phys.* **45**, 7009 (2006).
[30] Q. Y. He, Q. Hao, G. Chen, B. Poudel, X.W. Wang, D.Z. Wang, and Z.F. Ren, *Appl. Phys. Lett.* **91**, 052505 (2007).
[31] Y. K. Koh, C. J. Vineis, S. D. Calawa, M. P. Walsh, and D. G. Cahill, *Appl. Phys. Lett.* **94**, 153101 (2009).
[32] P.W. Lange, Naturwissenschaften **27**, 133 (1939).
[33] H. J. Goldsmid, *Proc. Phys. Soc. London. Sect. B* **69**, 203 (1956).
[34] H. J. Goldsmid, *Thermoelectric Refrigeration* (Plenum, New York, 1964).
[35] Y. Q. Cao, X. B. Zhao, T. J. Zhu, X. B. Zhang, and J. P. Tu, *Appl. Phys. Lett.* **92**, 143106 (2008).
[36] H. E. Bennett, *Platinum Metals Rev.* **5**, 132 (1961).
[37] Ångström, *Phrl. Mag.* **25**, 130 (1863).
[38] D. J. Ryden, AERE Report 6996, UKAEA, Harwell (1973).
[39] H. J. Goldsmid, *Proc. Phys. Soc. London.* **71**, 633 (1958).
[40] T.M. Dauphinee, S.B. Woods, *Rev. Sci. Instrum.* **26**, 693 (1955).
[41] W. J. Parker, R. J. Jenkins, C. P. Butler, and G. L. Abbott, *J. Appl. Phys.* **32**, 1679 (1961).
[42] L. J. Van der Pauw, *Philips Research Reports* **13**, 1-9 (1958).
[43] P.W. Lange, *Naturwissenschaften* **27**, 133 (1939).
[44] H. J. Goldsmid, *Proc. Phys. Soc. London. Sect. B* **69**, 203 (1956).
[45] C. H. Seager, G. E. Pike, *Appl. Phys. Lett.* **35**, 709 (1979).
[46] C. H. Seager, G. E. Pike, *Appl. Phys. Lett.* **37**, 747 (1980).
[47] G. E. Pike, *Phys. Rev. B* **30**, 795 (1984).
[48] C. H. Seager, G. E. Pike, and D. S. Ginley, *Phys. Rev. Lett.* **43**, 532 (1979).
[49] D.V. Lang, *J. Appl. Phys.* **45**, 3023 (1974).
[50] T. Knittel and H. J. Goldsmid, *J. Phys. C: Solid State Phys.* **12**, 1891 (1979).
[51] V. M. Muzhdaba and S. S. Shalyt, *Fiz. Tverd. Tela* **8**, 3727 (1966).
[52] P. F. P. Poudeu, J. D'Angelo, H. J. Kong, A. Downey, J. L. Short, R. Pcionek, T. P. Hogan, C. Uher, and M. G. Kanatzidis, *J. Am. Chem. Soc.* **128**, 14347 (2006).
[53] Y. C. Lan, B. Poudel, Y. Ma, D. Z. Wang, M. S. Dresselhaus, G. Chen, and Z. F. Ren, *Nano Lett.* **9**, 1419 (2009).
[54] B. C. Sales, D. Mandrus, and R. K. Williams, *Science* **272**, 1325 (1996).
[55] G. S. Nolas, J. L. Cohn, and G. A. Slack, *Phys. Rev. B* **58**, 164 (1998).
[56] T. M. Tritt, *Semiconductors and Semimetals* (Academic, San Diego, CA, 2001), Vol. 69, pp. 139-253.

[57] B. Chen, J. H. Xu, C. Uher, D. T. Morelli, G. P. Meisner, J. P. Fleurial, T. Caillat, and A. Borshchevsky, *Phys. Rev. B* **55**, 1476(1997).
[58] V. Keppens, D. Mandrus, B. C. Sales, B. C. Chakoumakos, P. Dai, R. Coldea, M. B. Maple, D. A. Gajewski, E. J. Freeman, and S. Bennington, *Nature* **395**, 876 (1998).
[59] M. Puyet, B. Lenoir, A. Dauscher, M. Dehmas, C. Stiewe, and E. Muller, *J. Appl. Phys.* **95**, 4852 (2004).
[60] L. D. Chen, T. Kawahara, X. F. Tang, T. Goto, T. Hirai, J. S. Dyck, W. Chen, and C. Uher, *J. Appl. Phys.* **90,** 1864 (2001).
[61] G. S. Nolas, M. Kaeser, R. T. Littleton IV, and T. M. Tritt, *Appl. Phys. Lett.* **77**, 1855 (2000).
[62] H. Y. Geng, S. Ochi, and J. Q. Guo, *Appl. Phys. Lett.* **91** 022106 (2007).
[63] H. Li, X. F. Tang, Q. J. Zhang, and C. Uher, *Appl. Phys. Lett.* **93**, 252109 (2008).
[64] H. Li, X. F. Tang, X. L. Su, and Q. J. Zhang, *Appl. Phys. Lett.* **92**, 202114 (2008).
[65] X. Shi, H. Kong, C.-P. Li, C. Uher, J. Yang, J. R. Salvador, H. Wang, L. Chen, and W. Zhang, *Appl. Phys. Lett.* **92**, 182101 (2008).
[66] G. Min and D. M. Rowe, *Meas. Sci. Technol.* **12**, 1261–1262 (2001).
[67] Y.C. Lan, D.Z. Wang, G. Chen, Z.F. Ren, *Appl. Phys. Lett.* **92**, 101910 (2008).
[68] H. Zhou, *Appl. Math. Sci.* **4**, 505 (2010).
[69] G. J. Snyder and T. S. Ursell, *Phys. Rev. Lett.* **91**, 148301 (2003).
[70] S. M.Manyakin, M. P.Volkov, *Proc. 21st Int. Conf. Thermoelectrics*, New Jersey, USA (2002).
[71] N. Kh. Abrikosov et al., *Neorganicheskiye Materialy* **13**, 827 (1977, in Russian).
[72] A. Pattamattaa and C. K. Madnia, *Int. J. Heat Mass Transfer* **52**, 860 (2009).

Chapter 3. Theoretical Analysis Based on the Boltzmann Transport Equation

In this chapter, theoretical analysis based on the Boltzmann transport equation (BTE) is conducted on the measured thermoelectric properties of nanocomposites. Such analysis is important for us to understand the phonon and electron transport inside nanocomposites, and thus to provide useful guidance for the future improvement of their material properties. The detailed modeling of phonons and electrons is separately discussed in all sections, with similarities pointed out between the two.

3.1 Boltzmann Transport Equation under the Relaxation Time Approximation

The BTE describes the transport of an ensemble of particles. This equation is related to the variation of the distribution function $f\left(t,\vec{r},\vec{k}\right)$, which depends on time t, position $\vec{r}$, and wave vector $\vec{k}$. In physics, $f\left(t,\vec{r},\vec{k}\right)$ is defined as the mean particle number at time t in the d^3r volume around $\vec{r}$, with wave vector $\vec{k}$ and d^3k accuracy. Without carrier generation and recombination, the BTE of charge carrier transport is given by [1-3]

$$\frac{\partial f}{\partial t}+\vec{F}\cdot\nabla_{\vec{p}}f+\vec{V}_g\cdot\nabla_{\vec{r}}f=\frac{\partial f}{\partial t}\Big|_{collision}, \tag{3-1}$$

in which $\vec{F}$ is the force applied on charge carriers, $\vec{p}=\hbar\vec{k}$ is the momentum, $\hbar$ is the Planck's constant divided by 2π, $\vec{V}_g=\nabla_{\vec{p}}E$ is the group velocity, and E is the energy. Assuming low electric fields and the elastic scattering of charge carriers, the relaxation time approximation can be employed to simplify the collision term $\frac{\partial f}{\partial t}\Big|_{collision}$ [1-3], given by

$$\frac{\partial f}{\partial t}\Big|_{collision}=-\frac{f-f_0}{\tau}, \tag{3-2}$$

where τ is scattering relaxation time. The equilibrium value of f, denoted by f_0, is given by the Fermi-Dirac distribution as

$$f_0 = \frac{1}{\exp\left(\frac{E - E_f}{k_B T}\right) + 1}. \tag{3-3}$$

Here E_f, k_B, T are the Fermi level, the Boltzmann constant, and the local temperature, respectively. The Fermi level E_f is determined by the measured carrier concentrations and density-of-states (DOS) effective masses of the charge carriers, which will be discussed in Section 3.2.1. Equations (3-1) and (3-2) yield the BTE used for charge carrier transport

$$\frac{\partial f}{\partial t} + \vec{F} \cdot \nabla_{\vec{p}} f + \vec{V}_g \cdot \nabla_{\vec{r}} f = -\frac{f - f_0}{\tau}. \tag{3-4}$$

In the steady state, we simply have $\partial f / \partial t = 0$ in Eq. (3-4).

For phonon transport, the force term in Eq. (3-1) disappears and the equilibrium value of f is given by the Bose-Einstein distribution as [1-3]

$$\langle n \rangle = \frac{1}{\exp\left(\frac{\hbar\omega}{k_B T}\right) - 1}, \tag{3-5}$$

where ω is phonon angular frequency. With group velocity $\vec{V}_g = \nabla_{\vec{k}} \omega$ for phonons, the BTE for phonon transport is simply

$$\frac{\partial f}{\partial t} + \vec{V}_g \cdot \nabla_{\vec{r}} f = -\frac{f - \langle n \rangle}{\tau}. \tag{3-6}$$

3.2 Macroscopic Electrical Properties

For any materials system, the BTE can be solved under specified boundary conditions to extract the expressions for different material properties. For instance, we can apply a temperature difference across an open-loop 1D structure, and the Seebeck coefficient is then defined as the negative of the voltage difference over the applied temperature difference. The detailed derivations of various properties can be found elsewhere [1-3] and all discussions here will only focus on their analytical expressions.

3.2.1 Expressions of Different Electrical Properties

Effective Mass of Charge Carriers. In electrical property calculations, usually the only information required from the band structure $E(\vec{k})$ is the effective mass of charge carriers, defined as [1-5]

$$m_i^* = \left(\frac{1}{\hbar^2} \frac{dE}{k_i dk_i} \right)^{-1}. \tag{3-7}$$

Here the subscript i indicates the direction. Close to the conduction band minimum or valence band maximum, the energy $E(\vec{k})$ is normally approximated as a parabolic function [1-3]. For convenience, the following discussions always assume the case of electrons, while the corresponding result is expected for holes. With the energy extrema of the band taken at the origin ($\vec{k}$ =0), the $E(\vec{k})$ relationship for the conduction band follows the general formula

$$E(\vec{k}) = \frac{\hbar^2}{2} \left(\frac{k_x^2}{m_x^*} + \frac{k_y^2}{m_y^*} + \frac{k_z^2}{m_z^*} \right), \tag{3-8}$$

where E refers to the conduction band edge E_c. For a spherical and parabolic band, the above expression can be simplified as

$$E(\vec{k}) = \frac{\hbar^2}{2} \frac{k^2}{m^*}, \tag{3-9}$$

in which $k^2 = k_x^2 + k_y^2 + k_z^2$, $m^* = m_x^* = m_y^* = m_z^*$. Away from the band edge, $E(\vec{k})$ deviates from the above quadratic expressions and the band nonparabolicity must be considered [2-5]. This is normally the case for the heavily doped TE nanocomposites with a narrow band gap E_g because their Fermi levels always cut into the bands and thus high-energy charge carriers are involved in the transport process. In this situation, we employ the Kane's model [2-5] to describe a nonparabolic band, given as

$$\gamma(E) = E(1 + \alpha E) = \frac{\hbar^2}{2} \left(\frac{k_x^2}{m_x^*} + \frac{k_y^2}{m_y^*} + \frac{k_z^2}{m_z^*} \right), \tag{3-10}$$

in which the factor α can be estimated as $\alpha = 1/E_g$ when there are no accurate values available in the literature. For a direct band gap at the Γ point, in some papers a

correction factor is added to estimate α, given as $\alpha = \left(1 - m_\Gamma^* / m_0\right)^2 / E_g$ [2]. Here m_Γ^* is the Γ-point effective mass and m_0 is the mass per electron. More accurate band structure description may further consider effects such as spin-orbit coupling, as suggested by Dresselhaus for zinc blende structures [6].

Because ellipsoidal constant energy surfaces are encountered in most cases, the longitudinal and transverse directions of a band are often used instead of the x, y, and z directions. In this situation, Eq. (3-10) is often rewritten as

$$\gamma(E) = \frac{\hbar^2}{2}\left(\frac{k_L^2}{m_L^*} + 2\frac{k_T^2}{m_T^*}\right), \tag{3-11}$$

with m_L^*, m_T^* as the longitudinal and transverse effective masses, respectively. Equations (3-7) and (3-11) yield the energy-dependent effective mass as

$$m_i^* = m_{i0}^*\left(1 + 2\alpha E\right), \tag{3-12}$$

where m_{i0}^* is the effective mass at the band edge in the i direction. With N as the number of conduction-band valleys, the density of states (DOS) effective mass m_d^* is defined as

$$m_d^* = N^{2/3}\left(m_L^* m_T^{*2}\right)^{1/3}. \tag{3-13}$$

The carrier concentration can then be evaluated by

$$n = \frac{\left(2m_d^* k_B T\right)^{3/2}}{3\pi^2\hbar^3}\,{}^0L_0^{3/2}, \tag{3-14}$$

in which we define a general integral ${}^nL_k^m$ as

$${}^nL_k^m = \int_0^\infty (-\frac{\partial f}{\partial z}) z^n (z + \beta z^2)^m (1 + 2\beta z)^k \, dz, \tag{3-15}$$

with $\beta = k_B T / E_g$, $z = E / k_B T$, the Fermi-Dirac distribution function $f = [\exp(z - \eta) + 1]^{-1}$, and the reduced Fermi level $\eta = E_f / k_B T$.

In addition to m_d^*, the conductivity effective mass m_χ^*, also called the electric-susceptibility effective mass, is defined as

$$m_\chi^{*-1} = \left(m_L^{*-1} + 2m_T^{*-1}\right)/3. \tag{3-16}$$

This effective mass is used in the expressions for the electrical conductivity and carrier mobility.

Expressions for the Electrical Properties. By solving the BTE under specified boundary conditions, we obtain the expressions of the charge carrier mobility μ, electrical conductivity σ, Seebeck coefficient S, and Lorentz number L_0 as [3-5]

$$\mu = \frac{e}{m_\chi^*} \frac{\int_0^\infty (-\frac{\partial f}{\partial z}) \tau(z) \frac{(z+\beta z^2)^{3/2}}{1+2\beta z} dz}{\int_0^\infty (-\frac{\partial f}{\partial z})(z+\beta z^2)^{3/2} dz}, \tag{3-17}$$

$$\sigma = \frac{(2m_d^* k_B T)^{3/2} e^2}{3\pi^2 \hbar^3 m_\chi^*} \int_0^\infty (-\frac{\partial f}{\partial z}) \tau(z) \frac{(z+\beta z^2)^{3/2}}{1+2\beta z} dz, \tag{3-18}$$

$$S = \frac{k_B}{e} \frac{\int_0^\infty (-\frac{\partial f}{\partial z}) \tau(z)(z-\eta) \frac{(z+\beta z^2)^{3/2}}{1+2\beta z} dz}{\int_0^\infty (-\frac{\partial f}{\partial z}) \tau(z) \frac{(z+\beta z^2)^{3/2}}{1+2\beta z} dz}, \tag{3-19}$$

$$L_0 = (\frac{k_B}{e})^2 \left\{ \frac{\int_0^\infty (-\frac{\partial f}{\partial z}) \tau(z) z^2 \frac{(z+\beta z^2)^{3/2}}{1+2\beta z} dz}{\int_0^\infty (-\frac{\partial f}{\partial z}) \tau(z) \frac{(z+\beta z^2)^{3/2}}{1+2\beta z} dz} - \left[\frac{\int_0^\infty (-\frac{\partial f}{\partial z}) \tau(z) z \frac{(z+\beta z^2)^{3/2}}{1+2\beta z} dz}{\int_0^\infty (-\frac{\partial f}{\partial z}) \tau(z) \frac{(z+\beta z^2)^{3/2}}{1+2\beta z} dz} \right]^2 \right\}. \tag{3-20}$$

After computing L_0 and σ, the electronic thermal conductivity k_e can be calculated by the Wiedemann-Franz law, $k_e = L_0 \sigma T$. For phonon transport analysis, the lattice thermal conductivity k_L is computed by subtracting k_e from the measured thermal conductivity. In Section 3.3, the detailed modeling of k_L will be discussed.

Multi-band Calculations. In many materials systems, multiple conduction- and valence-band valleys contribute to transport processes. In general, we find the reduced Fermi level η from the charge neutrality agreement inside a sample, given by

$$N_D^+ - N_A^- = \sum_i n_{ei} - \sum_j n_{hj}, \tag{3-21}$$

where n_{ei} is the electron density for the conduction band i, n_{hj} is the hole density for the valence band j, N_D^+ is the donor concentration, and N_A^- is the acceptor concentration. Both n_{ei} and n_{hj} are computed by Eq. (3-14) as a function of η, which is then determined by the numerical inversion of Eq. (3-21). Linear combinations of the contributions from all bands yield the following individual properties such as

$$\mu = \frac{\sum_i \mu_i n_i}{\sum_i n_i}, \tag{3-22}$$

$$\sigma = \sum_i \sigma_i, \tag{3-23}$$

$$S = \frac{\sum_i \sigma_i S_i}{\sum_i \sigma_i}, \tag{3-24}$$

where μ is again the charge carrier mobility, the subscript i indicates the band index. For narrow-band-gap TE materials at elevated temperatures, thermally excited minority carriers would play an important role in the transport processes. Electrons and holes both contribute to the electrical conductivity and thermal conductivity, but they cancel out in the Seebeck coefficient due to the opposite signs of the charged carriers. In this situation, the electronic thermal conductivity k_e can be significantly larger than the summation of the partial electronic thermal conductivities for each band. The additional contribution is known as the bipolar thermo-diffusion effect [7] and k_e can be calculated by [3]

$$k_e = \sum_i k_{e,i} + \sum_{i \neq k} \frac{\sigma_i \sigma_k}{\sigma_i + \sigma_k} \left(S_i - S_k\right)^2 T, \tag{3-25}$$

in which the subscripts i, k are band indices. When i and k refer to different types of bands, they can have opposite signs for their Seebeck coefficients so that the second term on the right hand side of Eq. (3-25) becomes important.

3.2.2 Scattering Mechanisms of Charge Carriers

In Eqs. (3-17) to (3-20) of this chapter, the total relaxation time $\tau(z)$ is the only unknown function, and $\tau(z)$ is obtained by adding up the individual scattering rates $\tau_i(z)$ using Matthiessen's rule [1-3]

$$\tau(E)^{-1} = \sum_i \tau_i(E)^{-1} . \tag{3-26}$$

In this section, models of the scattering rate $\tau_i(z)$ employed in this thesis are introduced for different scattering mechanisms.

Inside a grain, charge carriers are scattered mainly by ionized impurities and the deformation potential for acoustic phonons [2]. Both scatterings are elastic, which is required for the relaxation time approximation used to simplify the BTE. The considerations for neglecting other scattering mechanisms are listed as follows: (1) polar acoustic phonon (piezoelectric) scattering becomes important only at very low temperatures in very pure semiconductors [2]; (2) optical deformation potential scattering and more complicated intervalley scattering processes were not suggested for these material systems in the literature. Polar optical phonon scattering of charge carriers is weak in covalent crystals [8] such as $Bi_xSb_{2-x}Te_3$ but is suggested to be more important for $CoSb_3$ [9].

On the grain interfaces, the dangling broken bonds would trap nearby charge carriers and form a potential barrier E_b to block the current flow [10]. When charge carriers are scattered by a potential barrier, the energy distribution of the carriers deviates from that in the bulk material. Away from the barrier, the energy distribution of the carriers finally relaxes back to that in the bulk material after a distance l_E, called the energy relaxation length. On the other hand, the behavior of over-the-barrier carriers ($E > E_b$) is similar to that in the bulk material if the grain size d is much larger than the momentum relaxation length l_m. For TE nanocomposites, the preferred grain size should satisfy $l_m < d < l_E$ [11]. In this situation, the Seebeck coefficient is significantly increased by the energy filtering occurring at the grain interfaces [11-13], but the differential electrical conductivity $\sigma(E)$ ($E > E_b$ here) is unchanged from the bulk $\sigma(E)$. The interface electrical properties can be calculated by increasing the lower limits of all

integrations in Eqs. (3-17) to (3-20) from 0 (band edge) to E_b [11-16]. This assumes that all charge carriers with E< E_b are filtered out (no tunneling) and thus do not contribute to the electrical properties. When the grain size $d > 2\,l_E$, the effective properties of a composite material should be averaged between the grain-interface regions and the grain interior regions [17,18]. In the latter case, we are dealing with bulk properties predicted by Eqs. (3-17) to (3-20). Although the electrical properties can be estimated on the grained interfaces and further averaged across the material, the above treatment does not accurately deal with the transition from the grain interfaces to the grain interior regions. In a different approach, the grain interface scattering of charge carriers is included by identifying a scattering potential and calculating the corresponding scattering rate, which is then added to other scattering rates [19]. Similar to ionized impurity scattering, the grain interfaces are simply viewed as scattering centers and a nanocomposite is no longer divided into the interface and in-grain regions for calculations.

Acoustic Deformation Potential Scattering. Inside a material, longitudinal phonons can create volume changes in the lattice and thus cause a deviation from the periodicity of the lattice and these deviations from periodicity scatter charge carriers. This perturbing potential is expected to be proportional to the total volume change by the acoustic phonon:

$$U_{AC} = D\nabla\cdot\vec{u}, \tag{3-27}$$

where the constant D is called the acoustic deformation potential and $\vec{u}$ is the displacement of the phonon. For both electrons and holes, the relaxation time for acoustic deformation potential scattering is given as [20]

$$\tau_A^{-1} = \frac{\pi D_A^2 k_B T}{\rho v_S^2 \hbar} D(E)\left\{\left[1-\frac{E}{E_g+2E}\left(1-\frac{D_v}{D_A}\right)\right]^2 - \frac{8}{3}\frac{E\left(E_g+E\right)}{\left(E_g+2E\right)^2}\frac{D_v}{D_A}\right\}, \tag{3-28}$$

in which the sound velocity $v_S = \sqrt{c_l / d}$, c_l is the elastic constant, d is the density, D_v is the deformation potential for holes, D_A is that for electrons, and the nonparabolic electronic density of states $D(E)$ is given by:

$$D(E)=\frac{1}{2\pi^2}\left(\frac{2m_D}{\hbar^2}\right)^{3/2}\nu^{1/2}(E)\frac{d\nu}{dE}. \tag{3-29}$$

If the Debye model is employed for the phonon analysis, three identical acoustic branches are assumed and v_S is related to the Debye temperature θ by [21]

$$v_S=\frac{k\theta}{h}\left(\frac{V_0}{6\pi^2}\right)^{1/3}, \tag{3-30}$$

in which V_0 is the average atomic volume. In some papers, the correction factor in Eq. (3-28) is not used and the corresponding expression is simply

$$\tau_A^{-1}=\frac{\pi D_i^2 k_B T}{\rho v_S^2 \hbar}D(E). \tag{3-31}$$

Here the acoustic deformation potential D_i is written as D_v for the valence band or D_A for the conduction band.

Ionized Impurity Scattering. In addition to the scattering from phonons, charge carriers can also be scattered by ionized impurities inside a sample. This scattering mechanism is caused by the electric field associated with ionized impurities, i.e., atoms for either donors or acceptors. Ionized impurity scattering is dominant at very low temperatures and can also be strong at high temperatures in heavily doped TE materials. With the screening by free carriers around an ionized impurity, the electric field is described by a screened Coulomb potential:

$$U_S=\frac{Ze}{4\pi\varepsilon r}e^{-r/r_S}, \tag{3-32}$$

where Z is the number of charge units per impurity center, ε is the static permittivity, e is the charge per electron, and the screening length r_S is given as

$$r_S^{-2}=\frac{2^{5/2}e^2 m_d^{3/2}\sqrt{k_B T}}{\pi\hbar^3\varepsilon}{}^0L_1^{1/2}. \tag{3-33}$$

Here ${}^nL_k^m$ is defined in Eq. (3-15). For nondegenerate semiconductors, this screening length simply reduces to the well known Debye length $L_D=\left(\varepsilon k_B T/e^2 n_0\right)^{1/2}$ [2], where

n_0^- is the carrier concentration. Based on the Fermi's Golden Rule, the potential U_S leads to a corresponding relaxation time given by [2]

$$\tau_I^{-1} = \frac{\pi\left(4\pi Ze^2/\varepsilon\right)^2}{8\hbar k^4} D(E)\left(\ln(1+\xi) - \frac{\xi}{1+\xi}\right) N_D, \tag{3-34}$$

in which N_D is the volumetric concentration of scattering centers, $\xi = (2kr_S)^2$.

Polar Optical Phonon Scattering. This scattering occurs when the bond between two constituent materials in a compound is slightly ionic. For ionic crystals such as GaAs, the polar optical phonon scattering can be significant [2]. The high temperature relaxation time is given by Ravich et al. [20], and this expression incorporates screening from free electrons:

$$\tau_P^{-1} = \frac{\sqrt{2m_d^*}k_B T e^2\left(\varepsilon_\infty^{-1} - \varepsilon_0^{-1}\right)}{\hbar^2} \frac{1+2\alpha E}{\sqrt{E(1+\alpha E)}} F, \tag{3-35}$$

$$F = \left[1 - \delta\ln\left(1+\frac{1}{\delta}\right)\right] - \frac{2\alpha E(1+\alpha E)}{(1+2\alpha E)^2}\left[1 - 2\delta + 2\delta^2\ln\left(1+\frac{1}{\delta}\right)\right], \tag{3-36}$$

in which $\delta^{-1/2} = 2kR$, ε_∞ is high-frequency permittivity, and the screening length R is given by

$$R^{-2} = \frac{2^{5/2}e^2 m_d^{3/2}\sqrt{k_B T}}{\pi\hbar^3\varepsilon_\infty} {}^0L_1^{1/2}. \tag{3-37}$$

Here ε in Eq. (3-33) is replaced by ε_∞, with all other terms unchanged.

3.3 Macroscopic Lattice Thermal Conductivity

3.3.1 Callaway's Model

The theoretical analysis strategy is to first fit the measured Seebeck coefficient and the electrical conductivity, from which the parameters that are used in the employed models for the various charge carrier scattering mechanisms can be determined. With these parameters, $\tau_i(z)$ for the various charge carrier scattering mechanisms can be calculated, thereby yielding the electronic thermal conductivity $k_e = L_0\sigma T$. Secondly, k_e

is subtracted from the measured thermal conductivity to get k_L, which is then fitted by the Callaway's model [22] for the phonon transport. Similar to the electrical property analysis, additional parameters used in different phonon scattering models are treated as fitting parameters for k_L.

In the phonon transport modeling, four major scattering mechanisms are considered: (1) three- or four-phonon scattering, including normal (N) and Umklapp (U) processes, (2) electron-phonon scattering, (3) point defect (alloy) scattering, and (4) grain boundary scattering. Under the Debye approximation, the lattice thermal conductivity k_L is written as [22]

$$k_L = \frac{k_B}{2\pi^2 v_s}\left(\frac{k_B\theta}{\hbar}\right)^3\left(I_1 + \frac{I_2^2}{I_3}\right), \tag{3-38}$$

where

$$I_1 = \int_0^{\theta/T} \tau_c \frac{\nu^2 x^4 e^{\nu x}}{\left(e^{\nu x}-1\right)^2} dx, \tag{3-39}$$

$$I_2 = \beta \int_0^{\theta/T} \frac{\tau_c}{\tau_U} \frac{\nu^2 x^4 e^{\nu x}}{\left(e^{\nu x}-1\right)^2} dx, \tag{3-40}$$

$$I_3 = \beta \int_0^{\theta/T} \frac{1}{\tau_U}\left(1-\beta\frac{\tau_c}{\tau_U}\right) \frac{\nu^2 x^4 e^{\nu x}}{\left(e^{\nu x}-1\right)^2} dx, \tag{3-41}$$

θ is the Debye temperature, $x = \hbar\omega / k_B T$, $\nu = (\theta/T)^n k_B T / \hbar\omega_D$, $\tau_c(\omega)$ is the total relaxation time of all scattering mechanisms, $\tau_U(\omega)$ is the relaxation time of the U processes, β is the ratio between the scattering rates of the N processes and U processes, i.e. $\tau_N^{-1} = \beta\tau_U^{-1}$. Here $n \approx 1$ for three-phonon processes only and n can be increased to include high-order phonon scattering processes [19].

The Debye approximation assumes three identical acoustic branches with a linear phonon dispersion $\omega(k)$. A constant phonon group velocity $V_g = \partial\omega / \partial k$ is thus used for high-frequency phonons whose V_g actually decays to zero at the first Brillouin zone edge.

This will overestimate the high-frequency phonon contributions to k_L [1]. To be more accurate, the phonon dispersion can be approximated by a sine function [23, 24]:

$$\omega = \omega_0 \sin\left(\frac{\pi}{2}\frac{k}{k_0}\right), \tag{3-42}$$

which accounts for the group velocity decay at high frequencies. Here ω_0 and k_0 are the maximum angular frequency and wave vector, respectively. For a material with N bases per unit volume and a sound velocity v_S, we can calculate the two values by

$$\omega_0 = \frac{2}{\pi} v_S \left(6\pi^2 N\right)^{1/3}, \tag{3-43}$$

$$k_0 = \left(6\pi^2 N\right)^{1/3}, \tag{3-44}$$

where the sound velocity v_S is averaged between the longitudinal (v_{SL}) and transverse (v_{ST}) values as [23]

$$v_S^{-2} = \frac{1}{3}\left(v_{SL}^{-2} + 2v_{ST}^{-2}\right). \tag{3-45}$$

The underlying physics behind this averaging method is to match the low-temperature lattice thermal conductivity.

3.3.2 Scattering Mechanisms of Phonons

As discussed in the foregoing section, four major scattering mechanisms of phonons are considered. The total relaxation time τ_c is still calculated by the Matthiessen's rule as

$$\tau_c^{-1} = \tau_N^{-1} + \tau_U^{-1} + \tau_{e-ph}^{-1} + \tau_{pd}^{-1} + \tau_G^{-1}, \tag{3-46}$$

where τ_N, τ_U, τ_{e-ph}, τ_{pd}, τ_G represent the relaxation time of the N processes, U processes, electron-phonon scattering, point-defect scattering, and grain boundary scattering, respectively.

Phonon-Phonon Scattering. Among the two types of phonon-phonon scattering processes, the momentum-conserved N process indirectly affects the transport process by altering the frequency distribution of resident phonons, while the momentum non-

conserved U process directly poses resistance to energy transport. The relaxation times are given as [25]

$$\tau_N^{-1}(x) = \beta\tau_U^{-1}, \tag{3-47}$$

$$\tau_U^{-1}(x) = \frac{20\pi}{3}\hbar N_A\left(\frac{6\pi^2}{4}\right)^{1/3}\frac{1+5\beta/9}{1+\beta}\frac{\gamma^2}{M_{AV}{a_{AV}}^2}\left(\frac{T}{\theta}\right)^3 x^2, \tag{3-48}$$

in which again $x = \hbar\omega/k_BT$, β is the ratio between τ_U and τ_N, γ is the Grüneisen constant (or anharmonicity parameter), N_A is the Avogadro's number, M_{AV} is the mean atomic mass for the material, and a_{AV} is the mean atomic size determined by the cubic root of the atomic volume. For a given composition, the average values M_{AV} and a_{AV} are computed by

$$M_{AV} = \sum_i f_i M_i, \tag{3-49}$$

$${a_{AV}}^3 = \sum_i f_i {a_i}^3. \tag{3-50}$$

Here f_i, M_i, a_i represent the fractional concentration, the atomic mass, and the atomic size for atom i. By merging all factors into a single constant C, Eq. (3-48) can also be written as [3]

$$\tau_U^{-1}(x) = C\omega^2 T = C\left(\frac{k_B x}{\hbar}\right)^2 T^3, \tag{3-51}$$

where C can be fitted directly and can bring convenience to our analysis.

Electron-Phonon Scattering. For heavily doped TE nanocomposites, the phonon scattering from bound charge carriers [26] can always be neglected. For free charge carrier scattering of phonons, the scattering rate is given by Ziman as [27]

$$\tau_{e-ph}^{-1}(\omega) = \frac{D^2 {m_d}^{*3} v_g}{4\pi\hbar^4 d}\frac{k_BT}{\frac{1}{2}{m_d}^* {v_g}^2} \times\left\{\frac{\hbar\omega}{k_BT} - \ln\frac{1+\exp\left[\left(\frac{1}{2}{m_d}^* {v_g}^2 - E_F\right)/k_BT + \hbar^2\omega^2/8{m_d}^* {v_g}^2 k_BT + \hbar\omega/2k_BT\right]}{1+\exp\left[\left(\frac{1}{2}{m_d}^* {v_g}^2 - E_F\right)/k_BT + \hbar^2\omega^2/8{m_d}^* {v_g}^2 k_BT - \hbar\omega/2k_BT\right]}\right\}, \tag{3-52}$$

where T is the absolute temperature, D is the acoustic deformation potential of the corresponding band, m_d^* is the DOS effective mass, d is the density, E_F is the Fermi energy calculated by the generalized Kane's model [4,5], the phonon group velocity v_g is typically averaged over the sound velocities of different branches as

$$v_g^{-1} = \frac{1}{3}\left(v_{SL}^{-1} + 2v_{ST}^{-1}\right). \tag{3-53}$$

For the Debye model, v_g becomes v_S defined in Eq. (3-30).

Point-Defect Scattering. Inside a grain, phonons are also scattered by point defects [28]. Similar to Rayleigh scattering, the scattering rate τ_{PD}^{-1} due to point defects is proportional to the fourth power of the phonon angular frequency ω:

$$\tau_{PD}^{-1} = \frac{V_0\Gamma}{4\pi v_g^3}\omega^4, \tag{3-54}$$

in which V_0 is the volume per atom, the average phonon group velocity v_g is calculated by either Eq. (3-53) or Eq. (3-30) for the Debye model. For impurity atoms on a single atomic site, the disorder parameter Γ in Eq. (3-54) is calculated as

$$\Gamma = \sum_i \left[f_i\left(1 - M_i / M_{AV}\right)^2 + \varepsilon_S f_i\left(1 - a_i / a_{AV}\right)^2 \right], \tag{3-55}$$

where ε_S is a strain parameter, again f_i is the fractional concentration of impurity atom i, M_i is its mass, and a_i is its atomic size, while M_{AV} is the mean atomic mass, and a_{AV} is the mean atomic size. When a single type of impurity atoms with a relative concentration α_i is considered, Eq. (3-55) is reduced to

$$\Gamma = \sum \alpha_i\left(1-\alpha_i\right)\left[\left(\Delta M / M_{AV}\right)^2 + \varepsilon_S \alpha_i\left(\Delta a / a_{AV}\right)^2\right], \tag{3-56}$$

where ΔM represents the mass difference between the impurity and the host atoms, Δa is the atomic size difference between the impurity and the host atoms. One example of this can be SiGe alloys, in which Si is the host and Ge is treated as the impurity atom [29]. Here M_{AV} and a_{AV} are averaged between Si and Ge atoms according to Eqs. (3-49) and (3-50), whereas ΔM and Δa are the corresponding differences between the two types of atoms.

Grain Boundary Scattering. Because the grain interfaces inside a nanocomposite are normally rough at the phonon wavelength scale, phonons incident on a grain interface are always assumed to be either diffusely transmitted or reflected. With an averaged grain size l, the corresponding scattering relaxation time τ_G is estimated by

$$\tau_G^{-1} = v_s / l . \tag{3-57}$$

It should be pointed out that this τ_G estimation is very coarse. First, the exact geometry of the structure, even the interface density (interface area per unit volume [30,31]), cannot be exactly treated in the analysis. Secondly, the traveling length for a phonon to reach the grain interface depends on the traveling direction and starting location of this phonon. Considering a phonon emitted from a grain interface (Fig. 3.1), l is actually its longest distance to reach the grain interface and τ_G can be significantly shorter in other traveling directions. Therefore, phonon size effects inside nanocomposites are expected to be underestimated by Eq. (3-57). In analogy to radiation, the average mean beam length for a sphere radiating to its own surface is $0.65l$ [32], which may replace l in Eq. (3-57) as a better estimation. For more accurate lattice thermal conductivity predictions, in Chap. 4 frequency-dependent Monte Carlo simulations are performed on 2D porous Si and 3D Si nanocomposites. The individual phonon movement is tracked and the exact structure geometry can be specified in actual simulations.

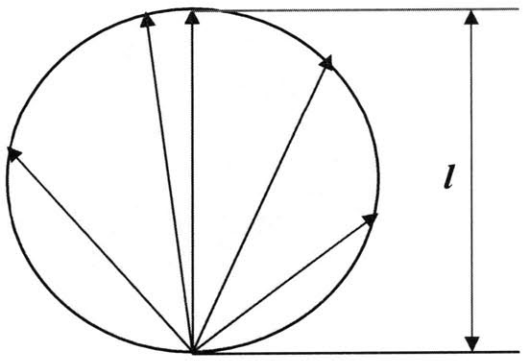

Figure 3.1 Phonon traveling distance between grain interfaces inside a spherical grain. The grain size l is seen to be the upper limit of this distance.

3.4 Results and Discussions

3.4.1 BiSbTe Nanocomposites

For BiSbTe nanocomposites, the theoretical analysis based on the BTE was performed mainly by Dr. Daryoosh Vashaee [33]. For the completeness of this thesis, his fitting results are summarized here. The analysis was first conducted on a state-of-the-art (SOA) ingot, and then extended to BiSbTe nanocomposites with major parameters determined by the first analysis. Because limited measurements were available in the literature for the bulk material with this composition, most material properties used for the analysis are determined by averaging between the values for bulk Sb_2Te_3 and Bi_2Te_3 according to their fractional concentrations. For instance, the dielectric constant can be averaged first among different crystal orientations in Bi_2Te_3 and Sb_2Te_3, and then between these two compositions, given as

$$\langle \varepsilon_r \rangle = \alpha_{Bi_2Te_3} \left[\left(\varepsilon_{r\perp} + 2\varepsilon_{r//} \right) / 3 \right]_{Bi_2Te_3} + \left(1 - \alpha_{Bi_2Te_3} \right) \left[\left(\varepsilon_{r\perp} + 2\varepsilon_{r//} \right) / 3 \right]_{Sb_2Te_3}, \qquad (3\text{-}58)$$

where for the Bi_2Te_3 percentage $\alpha_{Bi_2Te_3}$=0.25, the bulk values are given in Table 3.1. This leads to $\varepsilon_r(0)$=97. Values for other major parameters are listed in Table 3.2. The fitting results are presented in Figs. 3.2. The predicted lattice thermal conductivities are also shown in Fig. 2.14.

For the phonon modeling, the N processes, U processes, electron-phonon scattering, point-defect scattering, and grain boundary scattering are all considered for both the SOA ingot and the nanocomposite. In the electron modeling, charge carriers are scattered by the grain interfaces and acoustic phonons. The former one is neglected for the large-grain-size SOA ingot (l=1.0 μm) though it is included in the lattice thermal conductivity calculations. This treatment can be justified by the fact that charge carriers typically have much shorter mean free paths than phonons and are thus less affected by the grain interface scattering. All parameters determined by the SOA ingot analysis are then applied to the BiSbTe nanocomposites. As mentioned in Chap. 2, the bipolar contribution is suppressed in the BiSbTe nanocomposites, which can be observed from their slower thermal conductivity increase and lower power factor decay at elevated temperatures [33]. In the theoretical analysis, this can be explained by assuming an

interfacial potential (height $\Phi_B = 80$ meV, width w=9 Å) to scatter electrons (minority carriers) much more strongly than holes. The scattering rate associated with this barrier is given as [2]

$$\tau_{gb}^{-1} = \frac{1}{\pi\hbar^4 l^3} U_D^2 \sqrt{2} m_d^{*3/2} \sqrt{E(1+\alpha E)}(1+2\alpha E), \tag{3-59}$$

with $U_D = \Phi_B w^3$, l as the grain size, and α as defined in Eq. (3-10). Similar to Ref. 19, this scattering rate is added to that for the acoustic deformation potential to get the total relaxation time $\tau(z)$ for electrical property calculations. For heavily doped nanocomposites, majority carriers (holes here) generally have a much higher energy than minority carriers (electrons here) so that they are less affected by the grain-interface barrier.

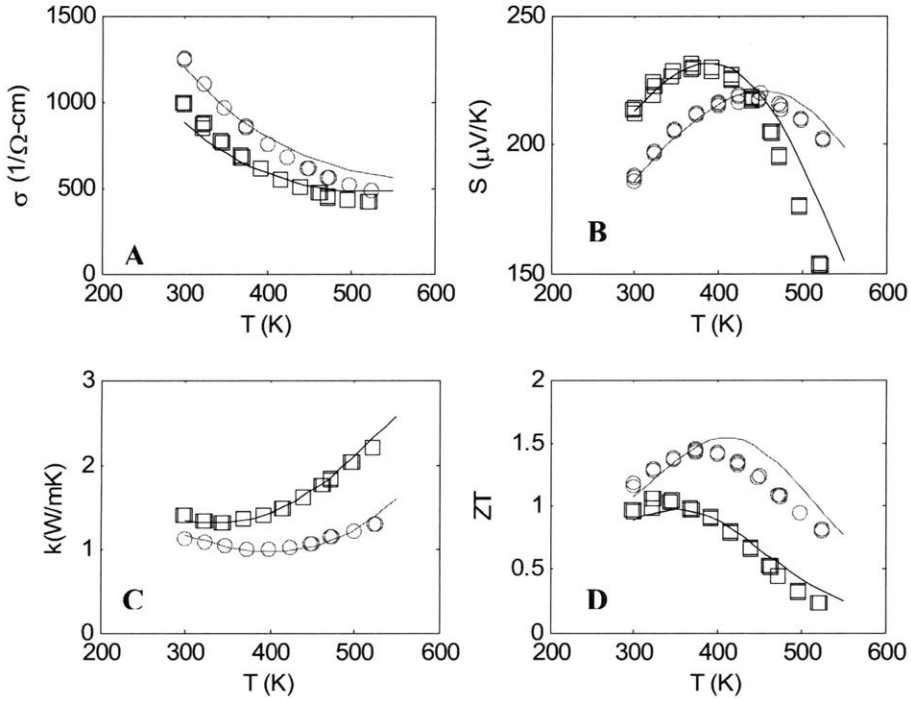

Figure 3.2 Fitting results of the SOA ingot (squares) and the BiSbTe nanocomposite from ingots (circles): (A) electrical conductivity, (B) Seebeck coefficient, (C) thermal conductivity, (D) ZT.

Table 3.1 Dielectric constants for bulk Sb_2Te_3 and Bi_2Te_3 [34]. Here the bulk values are averaged for a nanocomposite according to the composition. This should be justified when more experimental data are available.

Material	$\varepsilon_{r\perp}(0)$	$\varepsilon_{r//}(0)$
Sb_2Te_3 (80 K)	168	36.5
Bi_2Te_3 (15 K)	290	75

Table 3.2 Major parameters used in analyzing both the SOA ingot and the BiSbTe nanocomposites. These effective masses (in m_0) are mainly determined by fitting all three TE properties simultaneously.

Deformation potential	D=5.7 [eV]
τ_U / τ_N	β=20
Bandgap [35,36]	$E_g = 0.237 - 1.4\times10^{-4}T$ [eV]
Hole	m_L^*=0.39, m_T^*=0.168, m_d^*=0.317
Electron	m_L^*=0.22, m_T^*=0.20, m_d^*=0.155
Effective grain size	l=1.0 [μm] (ingot), l=60 [nm] (nanocomposite)
Charge units per impurity	Z =1
Anharmonicity parameter	γ=1
Strain parameter	ε_S=10
Phonon velocity	$v_g = v_S$=2463 [m/s]
Carrier concentration	p=1.8×10^{19} (SOA ingot), 2.56×10^{19} (nanocomposite) [cm^{-3}]
Debye temperature [37]	$\theta = 4.19\times10^{-8} a_{AV}^{-1.5} M_{AV}^{-0.5} G$=163 [K], G=0.43

3.4.2 Bulk $CoSb_3$ Analysis

As part of my thesis, efforts were also dedicated to analyzing the results of $Yb_xCo_4Sb_{12}$ nanocomposites. However, it was later found that the complicated band structures of $CoSb_3$-based nanocomposites caused unexpected uncertainties in such analysis. As one important parameter for the electron modeling, the bandgap value of pure $CoSb_3$ was reported to be from 0.031 to 0.7 eV by either calculations or measurements [38-52], which hinders accurate predictions for the occurrence of observed bipolar conduction at elevated temperatures [7,53]. In addition, it is difficult to estimate the effective masses of charge carriers from the complicated band structure of $CoSb_3$ and a large divergence exists in values used in the literature. For doped or filled $CoSb_3$, the calculated band structures were strongly distorted from that for the pure $CoSb_3$ and more uncertainties are therefore anticipated [49-52]. Keeping this in mind, fully understanding the electronic structure of bulk $CoSb_3$ should be regarded as a necessary step towards analyzing $CoSb_3$-based nanocomposites. In this section, preliminary results of bulk $CoSb_3$ analysis are presented as the starting point of more advanced modeling work in the future.

In the literature, limited modeling work on the transport properties of doped or filled $CoSb_3$ was available, and presently inconsistencies can always be found between different results. One noteworthy fact is that most of the work to date has only attempted to fit either the electrical properties or the thermal properties. However, the analysis of the thermal and electrical properties is coupled by shared parameters such as the acoustic deformation potentials. To obtain a dependable theoretical analysis, it is important to fit all TE properties with the same set of parameters. Secondly, most electron modeling was oversimplified: (1) Parabolic bands were still assumed [9, 48, 54, 55] though the band nonparabolicity was pointed out before [39]. As explained in Section 3.2.1, inaccuracies were expected for heavily doped samples whose Fermi level cuts into the bands. (2) A single band model was employed in some studies even though strong bipolar conduction was observed [48]. As shown in Eq. (3-25), this led to a significantly underestimated electronic thermal conductivity. (3) The acoustic deformation potential scattering was usually treated as the only scattering mechanism for charge carriers [48, 55]. The possibly important impurity scattering and polar optical phonon scattering [9] were often

neglected. When it comes to the phonon transport analysis, arguments mainly focus on the mechanisms of the significant thermal conductivity reduction in filled $CoSb_3$. One explanation for this thermal conductivity reduction is the "rattling" scattering [11,56], which assumes that filled foreign atoms can move about in the cage-like open structure and act as phonon rattlers. In addition, the lattice thermal conductivity reduction is also attributed to the mass fluctuation scattering (point defects) caused by the random distribution of partially filled atoms [57].

As the major topic of this section, a comprehensive analysis of the thermal and electrical properties is thus carried out on a Te-doped single-crystal $CoSb_3$ sample (n-type, 0.08% Te) reported in Ref. 48. The fitting results are shown in Fig. 3.3 and the fitting utilizes parameters that are listed in Table 3.3. For charge carriers, the scattering mechanisms include acoustic deformation potential scattering, ionized impurity scattering, and polar optical phonon scattering. For the phonon modeling, the N processes, U processes, electron-phonon scattering, and point-defect scattering are all considered. The thermal conductivities can be reasonably fitted by including high-order phonon scattering. The fitting parameter n is thus increased from 1 (three-phonon scattering only) to 3 for $\nu = (\theta / T)^n k_B T / \hbar\omega_D$ used in Eqs. (3-39) to (3-41).

Despite the big divergence in the reported bandgaps, the Seebeck coefficient fitting here clearly suggests a bandgap of around 0.24 eV, close to 0.22 eV given by Ref. 39. With a bandgap of 0.1 eV, the Seebeck coefficient switches its sign at 320 K (Fig. 3.4), a temperature much lower than the experimentally observed transition point (565 K). This cannot be corrected by changing the DOS effective masses of the charge carriers or the acoustic deformation potentials. On the other hand, a large bandgap at 0.5 eV indicates that bipolar conduction should take place at 600 K instead of 400 K based on Figs. 3.3A, C.

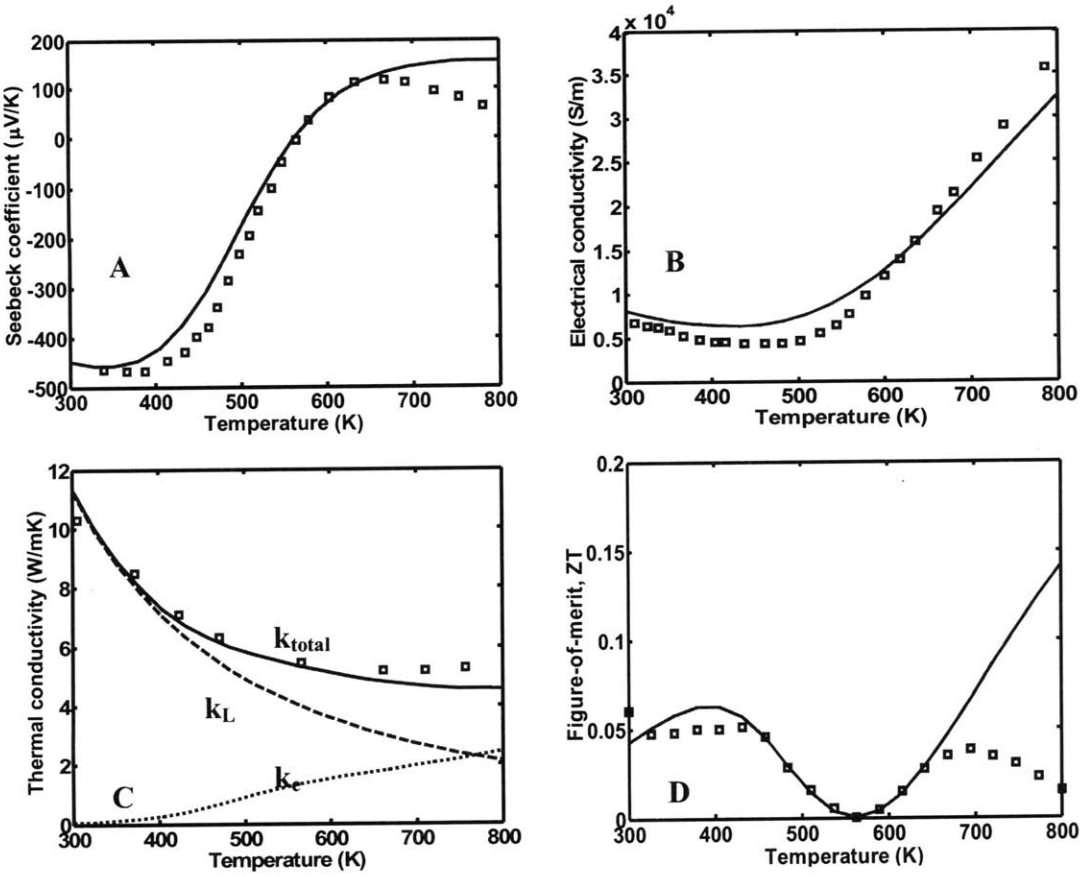

Figure 3.3 Theoretical fitting of S, σ, k and ZT for a Te-doped single-crystal $CoSb_3$ sample in Ref. 48. The squares are the measurement results. Lines are the theoretical predictions.

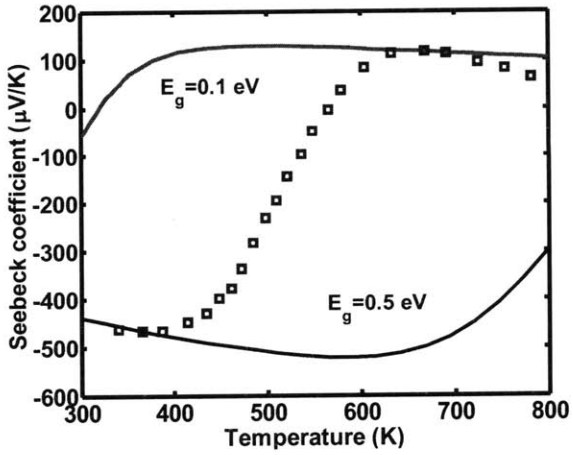

Figure 3.4 Seebeck coefficients predicted for bandgaps different from $E_g = 0.24$ eV used in Fig. 3.3A. The squares are again the experimental data. With a either too large or too small bandgap, changing other parameters does not lead to Seebeck coefficients agreeing with the measurements.

Table 3.3 Parameters used in analyzing the Te-doped single-crystal $CoSb_3$ sample in Ref. 48. All effective masses are in m_0. The nonparabolic valence band is spherical in the k space. The conduction band has a triply degenerate parabolic band (heavy electrons) and a nonparabolic band (light electrons) at the Γ point (see Fig. 3.5).

Deformation potential	$D_A = 0.2$, $D_V = 1.0$ [eV]
τ_U / τ_N	β=1.0 (2.75 in [56])
Bandgap	$E_g = 0.24$ [eV]
Electron	$m_L^* = 4.0$, m_T^*=0.5, m_d^*=1.04 (heavy electrons)
	m_L^*=1.6, m_T^*=0.2, m_d^* =0.2 (light electrons)
Hole	m_L^*=0.28, m_T^*=0.07, m_d^*=0.07 [39, 48]
Charge units per impurity	Z =1
Anharmonicity parameter	γ=0.7 (1.23 in [58])
Strain parameter	ε_S=0
Phonon velocity	$v_g = v_S$=2973 [m/s]
Carrier concentration	$n = 4.54\times10^{18}$ [cm^{-3}]
Debye temperature	θ=307 [K] [58]
Dielectric constant	$\varepsilon_r(\infty)$=25.6, $\varepsilon_r(0)$=33.5 [9,59]
Density	$d = 7640$ [kg/m^3] [60]

For $CoSb_3$-based nanocomposites with various compositions, it is more challenging to determine their bandgaps by either experiments or band structure calculations. Therefore, we pursued a simple bandgap measurement technique with nanopowders based on Fourier Transform Infrared Spectroscopy (FTIR), which is introduced in Chap. 5. This technique may help us to further clarify the puzzles on the

bandgap of pure $CoSb_3$ and may potentially be applied to general $CoSb_3$-based nanocomposites.

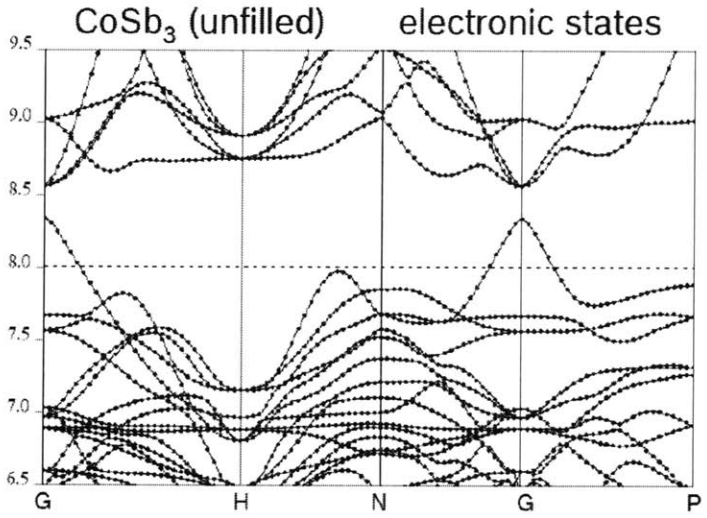

Figure 3.5 Band structure of $CoSb_3$, computed by our collaborators at the Bosch Research and Technology Center (unpublished).

3.5 Conclusions

This chapter summaries the theoretical analysis on BiSbTe nanocomposites and bulk $CoSb_3$. The latter one is the first step towards a detailed theoretical analysis of $CoSb_3$-based nanocomposites. Although reasonable agreement between the experimental results and theoretical analysis can be obtained, further improvement can still be made on how to better include the grain interface scattering into the 3D bulk material analysis. To reduce the uncertainties in the BTE analysis, additional measurements should also be conducted to provide more information for the electron and phonon transport. One example can be the interface capacitance measurements introduced in Chap. 5. Another one is the Nernst effect measurement whose results can be fitted together with S, σ and k to eliminate unrealistic choices of some parameters. This measurement is not discussed in this thesis but is introduced elsewhere [53]. Instead of using the coarse interface treatment in the BTE analysis, Monte Carlo simulations should also be performed for both electrons and phonons, in which the details of the grain interface scattering and the exact sample geometry can be specified. For electron Monte Carlo simulations, the local

Seebeck coefficients and electrical conductivities inside a grain can also be investigated in addition to the effective electrical properties of a nanocomposite. Similarly, phonon Monte Carlo simulations reveal details of the phonon transport inside a grain and can predict the phonon size effects more accurately than the Callaway's model. In Chap. 4, frequency-dependent Monte Carlo simulations are applied to 2D porous silicon and 3D silicon nanocomposites. In the future, more work should be conducted on electron Monte Carlo simulations of nanocomposites to yield accurate predictions of their TE properties.

3.6 References

[1] G. Chen, *Nanoscale Energy Transport and Conversion: A Parallel Treatment of Electrons, Molecules, Phonons, and Photons* (Oxford University Press, New York, 2005).

[2] M. Lundstrom, *Fundamentals of Carrier Transport* (Oxford University Press, Cambridge, UK, 2000).

[3] Austin Minnich, *Modeling the Thermoelectric Properties of Bulk and Nanocomposite Thermoelectric Materials*, Master thesis, Massachusetts Institute of Technology, May 2008. Department of Mechanical Engineering.

[4] E. O. Kane, *J. Phys. Chem. Solids* **1**, 249 (1957).

[5] J. Kołodziejczak, *Acta Phys. Pol.* **20**, 289 (1961).

[6] G. Dresselhaus, *Phys. Rev.* **100**, 580 (1955).

[7] P. J. Price, *Philos. Mag* **46**, 1252 (1955).

[8] A. F. Joffe and L. S. Stil'bans, translated by M. G. Priestley, *Rep. Prog. Phys.* **22**, 167 (1959).

[9] E. Arushanov, K. Fess, W. Kaefer, Ch. Kloc, and E. Bucher, *Phys. Rev. B* **56**, 1911 (1997).

[10] C. R. M. Grovenor, *J. Phys. C: Solid State Phys.* **18**, 4079 (1985).

[11] D. M. Rowe, Ed. *CRC Handbook of Thermoelectrics* (CRC, Boca Raton, FL, 1995).

[12] B. Moyzhes and V. Nemchinsky, *Appl. Phys. Lett.* **73**, 1895 (1998).

[13] J. Martin, Li Wang, Lidong Chen, and G. S. Nolas, *Phys. Rev. B* **79**, 115311 (2009).

[14] L. W. Whitlow and T. Hirano, *Proc. 12ndInt. Conf. Thermoelectrics*, Yokohama, Japan (1993).

[15] D. M. Rowe and G. Min, *Proc. 13rd Int. Conf. Thermoelectrics,* Kansas, USA (1994).

[16] Y. Nishio and T. Hirano, *Jpn. J. Appl. Phys.* **36**, 170 (1997).

[17] D. J. Bergman and O. Levy, *J. Appl. Phys.* **70**, 6821 (1991).

[18] D. J. Bergman and L. J. Fel, *J. Appl. Phys.* **85**, 8205 (1999).

[19] A. Minnich, H. Lee, X. W. Wang, G. Joshi, M. S. Dresselhaus, Z. F. Ren, G. Chen, and D. Vashaee, *Phys. Rev. B* **80**, 155327 (2009).

[20] Yu. I. Ravich, B. A. Efimova, and V. I. Tamarchenko, *Phys. Status Solidi (b)* **43**, 11 (1971).
[21] J. R. Drabble and H. J. Goldsmid, *Thermal Conduction in Semiconductors* (Pergamon Press, Oxford, 1961).
[22] J. Callaway, *Phys. Rev.* **113**, 1046 (1959).
[23] C. Dames and G. Chen, Chapter 42 in *Thermoelectrics Handbook: Macro to Nano*, edited by D. M. Rowe (CRC Press, Boca Raton, FL, 2005).
[24] C. Dames and G. Chen, *J. Appl. Phys.* **95**, 682 (2004).
[25] P. G. Klemens, in *Solid State Physics*, edited by F. Seitz and D. Turnbull (Academic, New York, 1958), Vol. 7, p. 1.
[26] K. Suzuki and N. Mikoshiba, *J. Phys. Soc. Jpn.* **31**, 44 (1971).
[27] J. M. Ziman, *Philos. Mag.* **1**, 191 (1956), *Philos. Mag.* **2**. 292 (1957).
[28] E. F. Steigmeier and B. Abeles, *Phys. Rev.* **136**, A1149 (1964).
[29] C. B. Vining, *J. Appl. Phys.* **69**, 331 (1991).
[30] M. S. Jeng, R. G. Yang, D. Song, and G. Chen, *ASME J. Heat Transfer* **130**, 042410 (1-11) (2008).
[31] A. Minnich, G. Chen, *Appl. Phys. Lett.* **91**, 073105 (2007).
[32] M. F. Modest, *Radiative Heat Transfer, 2nd edition* (Elsevier Science, California, 2003).
[33] B. Poudel, Q. Hao, Y. Ma, Y. C. Lan, A. Minnich, B. Yu, X. Yan, D. Z. Wang, A. Muto, D. Vashaee, X. Y. Chen, J. M. Liu, M. S. Dresselhaus, G. Chen, and Z. F. Ren, *Science* **320**, 634 (2008).
[34] R. W. G. Wyckoff, Landolt-Börnstein, New Series III/17f, *Group III: Crystal and Solid State Physics* (Springer, Berlin, 1983).
[35] M. Stordeur and H. Sobotta, *Proc. 1st European Cof. Thermoelectrics*, Ed. D. M. Rowe (P. Peregrinus, London, 1998).
[36] M. Stordeur, H. T. Langhammer, H. Sobotta, V. Riede, *Phys. Status Solidi (b)* **104**, 513 (1981). The bandgap of bulk $Bi_{0.5}Sb_{1.5}Te_3$ is around 0.2 eV at 300 K.
[37] E. F. Steigmeier and B. Abeles, *Phys. Rev.* **136**, A1149 (1964).
[38] D. J. Singh and W. E. Pickett, *Phys. Rev. B* **50**, 11235 (1994).
[39] J. O. Sofo and G. D. Mahan, *Phys. Rev. B* **58**, 15620 (1998).
[40] K. Koga, K. Akai, K. Oshiro, and M. Matsuura, *Phys. Rev. B* **71**, 155119 (2005).
[41] E. Z. Kurmaev, A. Moewes, I. R. Shein, L. D. Finkelstein1, A. L. Ivanovskii, and H. Anno, *J. Phys.: Condens. Matter* **16**, 979 (2004).
[42] G. S. Nolas, G. A. Slack, T. Caillat and G. P. Meisner, *J. Appl. Phys.* **79**, 2622 (1996).
[43] E. Arushanov, M. Respaud, H. Rakoto, J. M. Broto and T. Caillat, *Phys. Rev. B* **61**, 4672 (2000).
[44] D. Mandrus, A. Migliori, T. W. Darling, M. F. Hundley, E. J. Peterson, and J. D. Thompson, *Phys. Rev. B* **52**, 4926 (1995).
[45] J. W. Sharp, E. C. Jones, R. K. Williams, P. M. Martin, and B. C. Sales, *J. Appl. Phys.* **78**, 1013 (1995).
[46] K. Matsubara, T. Iyanaga, T. Tsubouchi, K. Kishimoto, and T. Koyanagi, in *Proc. 13rd Int. Conf. Thermoelectrics*, Kansas, USA (1994).
[47] L. D. Dudkin and N. K. Abrikosov, *Fiz. Tverd Tela (Leningrad)* **1**, 31 (1959) [*Sov. Phys. Solid State* **1**, 29 (1956)].

[48] T. Caillat, A. Borshchevsky, and J.-P. Fleurial, *J. Appl. Phys.* **80**, 4442 (1996).
[49] P. Ghosez, M. Veithen, *J. Phys.: Condens. Matter* **19**, 096002 (2007).
[50] Z. G. Mei, J. Yang, Y. Z. Pei, W. Zhang, L. D. Chen, and J. Yang, *Phys. Rev. B* **77**, 045202 (2008).
[51] J. Yang, L. Xi, W. Zhang, L. D. Chen, and J. H. Yang, *J. Electron. Mater.* **38**, 1397 (2009).
[52] L. Bertini and C. Gatti, *J. Chem. Phys.* **121**, 8983 (2004).
[53] H. J. Goldsmid, *Thermoelectric Refrigeration* (Plenum, New York, 1964).
[54] B. C. Sales, D. Mandrus, B. C. Chakoumakos, V. Keppens, and J. R. Thompson, *Phys. Rev. B* **56**, 15081 (1997).
[55] H. Anno, K. Matsubara, Y. Notohara, T. Sakakibara, H. Tashiro, *J. Appl. Phys.* **86**, 3780 (1999).
[56] G. Fowler, and G. S. Nolas, *Proc. 24th Int. Conf. Thermoelectrics*, South Carolina, USA (2005).
[57] G. S. Nolas, J. L. Cohn, and G. A. Slack, *Phys. Rev. B* **58**, 164 (1998).
[58] K. L. Stokes, A. C. Ehrlich, and G. S. Nolca, *Mater. Res. Soc. Symp.* **545**, 339 (1999).
[59] G. Kliche and H. D. Lutz, *Infrared Phys.* **24**, 171 (1984).
[60] J. Ackerman and A. Wold, *J. Phys. Chem. Solids* **38**, 1013 (1977).

Chapter 4. Frequency-Dependent Monte Carlo Simulations of Phonon Transport and ZT Predictions of Nano-Grained Bulk Silicon

4.1 Introduction

As pointed out in Chap. 1, the idea of thermoelectric (TE) nanocomposites is to significantly reduce the lattice thermal conductivity using grain interface scattering of phonons, and in some cases to simultaneously increase the power factor $S^2\sigma$, resulting in ZT improvements over their bulk counterparts [1]. Unlimited to nanocomposites of traditional TE materials [2-7], this approach may also yield a high ZT in materials that were previously unsuitable for TE applications due to their high thermal conductivities. This concept was first demonstrated in nano-grained bulk silicon, where a peak ZT around 0.7 was reported at around 1200 K [8].

Despite these promising results, very little theoretical work has been conducted to understand the phonon transport in TE nanocomposites, which hinders the prediction of their potential ZT improvements. Previous studies by either numerically solving the Boltzmann Transport Equation (BTE) [9-14] or Monte Carlo (MC) simulations [15-16] were always based on the gray medium approximation, i.e., a frequency-independent phonon mean free path (MFP). However, this approximation could lead to a significant underestimation of phonon size effects inside micro- to nano-structured bulk materials. For example, experimental results have suggested strong phonon size effects in micro-porous silicon films [17], which can be explained only if frequency-dependent phonon MFPs are considered [18].

In this chapter, a Monte Carlo simulation technique considering frequency-dependent phonon MFPs is introduced to investigate the phonon transport in various periodic structures. A novel boundary condition based on the periodic heat flux with a constant virtual wall temperature is developed for the studied periodic structures. This allows us to calculate the thermal conductivity of a periodic structure with a single period as the computational domain. In the literature, very few papers performed frequency-dependent MC simulations, and they were focused on thin films or nanowires [19-22], or

1D transient phonon transport [23]. This work is the first attempt to apply the Monte Carlo method to complicated geometries with inclusion of frequency-dependent phonon scattering. My code is used to compute the thermal conductivities of 2D porous silicon with periodically aligned pores [18] and 3D silicon nanoparticle composites [24]. For the 2D porous silicon case, it is found that phonon size effects caused by the periodically arranged pores can be remarkable even when the pore size and spacing are much larger than the averaged phonon MFPs. These results clearly show the importance of considering the frequency dependence of phonon MFPs in the analysis of micro- and nano-structured materials. For heavily doped silicon nanocomposites with grain sizes around 200 nm, phonon scattering by electrons and point defects are dominant and much smaller grain sizes are required to benefit from the grain interface scattering of phonons. Calculations for nanocomposites with 10 nm grain sizes show that the lattice thermal conductivity can be dropped to around 3.0 W/m·K at room temperature. The peak thermoelectric figure of merit (ZT) of 10-nm-grain-size nanocomposites is estimated to be around 1.0 at 1173 K, which is comparable to traditional SiGe alloys. Our results show the potential of obtaining high thermoelectric performance in bulk silicon by the nanocomposite approach. Furthermore, the MC simulation technique can also be applied to transient cases, which can be used to analyze the data from pump probe measurements.

4.2 Basic Simulation Scheme

In a MC simulation, phonons bundles are first drawn and distributed randomly across the computational domain. Each bundle represents a number of phonons with similar properties. Their initial states (velocity, frequency, branch, and traveling direction) are generated by a random sampling approach based on the equilibrium phonon spectrum [19,20], which will be discussed later. With their individual velocities and traveling directions, phonons are allowed to move and may experience various scattering events during their movement. At each time step, whether a phonon will get scattered and thus change its state is determined by a random number and the individual scattering probabilities. By tracking a large number of phonons and averaging the results over a long period of time, statistically the MC simulations will approach the BTE solutions after convergence.

As an overview, the procedure of MC simulations is briefly described here. We still follow the schematic process flow given in Ref. 16, but the gray-media approximation is replaced by the frequency-dependent model. In the simulation, the computational domain is divided into many spatial bins, also called subcells. Because it is not feasible to simulate a large number of phonons, phonons are grouped into bundles (with W phonons per bundle) to save computer memory. States of phonons inside each bundle are identical, i.e., they share the same angular frequency ω, traveling direction $\vec{k}$, polarization p, and group velocity $V_{g,p}(\omega)$, where the subscript p indicates the polarization. In this chapter, only the longitudinal acoustic (LA) branch and two transverse acoustic (TA) branches will be considered because the optical branches contribute little to the thermal conductivities [25]. The potential effect of optical phonon scattering on the acoustic phonon MFPs [26] is included via the molecular dynamics simulation results themselves, from which phonon MFPs are obtained for our MC simulations.

At the beginning of each simulation, phonon bundles are generated inside the computational domain according to the initial temperatures assigned to individual subcells. The states of created phonons are randomly sampled based on the equilibrium phonon spectrum $\langle n \rangle D(\omega)$ [19,20], where $D(\omega)$ is the density of states for phonons, $\langle n \rangle$ is the Bose-Einstein distribution at the current subcell temperature T, defined as

$$\langle n \rangle = \frac{1}{\exp\left(\frac{\hbar\omega}{k_B T}\right) - 1}. \tag{4-1}$$

For a subcell with volume V_{sub}, the number of created phonon bundles is $V_{sub}\sum_{p=1}^{3}\int_0^{\omega_{p,\max}} \langle n \rangle D(\omega) d\omega / W$, in which $\omega_{p,\max}$ is the maximum phonon frequency for branch p, and W is again the phonon bundle size. Initially, the created phonon bundles are randomly distributed spatially inside each subcell. In all simulations, W is chosen so that the total number of initialized phonon bundles inside the whole domain is less than 1.5×10^7. Although smaller W is always preferred for less fluctuations in simulation results, the computing speed can be extremely slow with more phonon bundles in the

domain. To define the frequency of a phonon bundle, ω_0, a random number R ($0 \le R \le 1$) is generated and ω_0 value should satisfy

$$R = \frac{\sum_{p=1}^{3} \int_0^{\omega_0} \langle n \rangle D(\omega) d\omega}{\sum_{p=1}^{3} \int_0^{\omega_{p,\max}} \langle n \rangle D(\omega) d\omega}. \tag{4-2}$$

The exact polarization of the phonon is determined by another random number between zero and unity. It indicates the LA branch if the number is less than the ratio

$$P = \left. \frac{\left[\langle n \rangle D(\omega)\right]_{LA}}{2\left[\langle n \rangle D(\omega)\right]_{TA} + \left[\langle n \rangle D(\omega)\right]_{LA}} \right|_{\omega=\omega_0}, \tag{4-3}$$

in which $\left[\langle n \rangle D(\omega)\right]_{LA}$ and $\left[\langle n \rangle D(\omega)\right]_{TA}$ represent the product $\langle n \rangle D(\omega)$ for the LA branch and TA branch, respectively. Otherwise, the phonon bundle belongs to a TA branch. After the polarization and angular frequency of a phonon bundle are both determined, its group velocity $V_{g,p}(\omega)$ can be obtained from the phonon dispersion curve. For the 3D simulation, the traveling direction of a phonon is generated by two random numbers, R_1 and R_2 ($0 \le R_{1,2} \le 1$). The unit vector of the traveling direction is

$$\vec{k} = \begin{pmatrix} \sin\theta\cos\psi \\ \sin\theta\sin\psi \\ \cos\theta \end{pmatrix}, \tag{4-4}$$

where the polar angle θ satisfies $\cos\theta = 2R_1 - 1$, and the azimuthal angle ψ is determined by $\psi = 2\pi R_2$.

Within a time step, each phonon bundle travels with its own group velocity, which is $V_{g,L}(\omega)$ for the longitudinal mode and $V_{g,T}(\omega)$ for the transverse mode. To achieve good spatial resolutions, the time step Δt is chosen so that the maximum travel distance of a phonon bundle within Δt, $V_{\max}\Delta t$, is smaller than the subcell dimension. Consequently, phonon bundles will generally take a few time steps to travel out of a subcell, which enables us to better capture the phonon movement. During their travels, the phonons may encounter the interfaces or the domain boundaries, and will change their

trajectories. The interface transport treatment will be discussed in the following subsections.

After the phonon movement, the total phonon energy inside each subcell is calculated and divided by the subcell volume to get the phonon energy density, defined as

$$E = \sum_{p=1}^{3} \int_0^{\omega_{p,\max}} \hbar\omega \langle n \rangle D(\omega) d\omega, \tag{4-5}$$

in which the pseudo-temperature $\widetilde{T}$ of a subcell appears in the term

$$\langle n \rangle = \frac{1}{\exp\left(\dfrac{\hbar\omega}{k_B \widetilde{T}}\right) - 1}, \tag{4-6}$$

and $\widetilde{T}$ can be computed by the numerical inversion of Eq. (4-5) [18-20]. The above expression works for phonons in equilibrium, but becomes invalid when we deal with transport processes. Within an infinitesimal time step Δt, the density of scattered phonons can be expressed as

$$N_s = \sum_{p=1}^{3} \int_0^{\omega_{p,\max}} \frac{\Delta t}{\tau(\omega)} \langle n \rangle D(\omega) d\omega, \tag{4-7}$$

where $\tau(\omega)$ is the scattering relaxation time, the weight $\Delta t / \tau(\omega)$ is the probability of being scattered, the subscript s indicates scattered phonons. In this situation, the scattered phonon pseudo-temperature $\widetilde{T}_s$, different from the subcell temperature $\widetilde{T}$, should be associated with a new energy density

$$E_s = \sum_{p=1}^{3} \int_0^{\omega_{p,\max}} \hbar\omega \frac{\Delta t \langle n \rangle}{\tau(\omega)} D(\omega) d\omega, \tag{4-8}$$

instead of the energy density E in Eq. (4-5). For a fixed time step Δt, we can always use

$$\frac{E_s}{\Delta t} = \sum_{p=1}^{3} \int_0^{\omega_{p,\max}} \hbar\omega \frac{\langle n \rangle}{\tau(\omega)} D(\omega) d\omega \tag{4-9}$$

to evaluate the temperature of scattered phonons.

The above approach is consistent with the results from the BTE. Under the relaxation time approximation, the phonon BTE can be written as [27]

$$\frac{\partial f}{\partial t}+V_{g,p}(\omega)\vec{k}\cdot\nabla_{\vec{r}}f=-\frac{f-\langle n\rangle}{\tau(\omega)}, \tag{4-10}$$

where $\vec{k}$ is the unit vector of the traveling direction, $\langle n\rangle$ is the Bose-Einstein distribution, $\tau(\omega)$ is the scattering relaxation time, vector $\vec{r}$ is the phonon position, f is the phonon distribution function, $V_{g,p}(\omega)$ is the group velocity, and subscript p indicates the polarization. We multiply both sides of Eq. (4-10) by $\hbar\omega D(\omega)$ and integrate with respect to phonon angular frequency ω. The summation over the three acoustic branches yields

$$\sum_{p=1}^{3}\int_0^{\omega_{p,\max}}\frac{\partial f}{\partial t}\hbar\omega D(\omega)d\omega+\sum_{p=1}^{3}\int_0^{\omega_{p,\max}}\hbar\omega D(\omega)V_{g,p}(\omega)\vec{k}\cdot\nabla_{\vec{r}}f d\omega$$

$$=-\sum_{p=1}^{3}\int_0^{\omega_{p,\max}}\hbar\omega D(\omega)\frac{f-\langle n\rangle}{\tau(\omega)}d\omega. \tag{4-11}$$

On the other hand, phonon energy conservation requires

$$\frac{\partial u}{\partial t}+\nabla_{\vec{r}}\cdot\vec{q}=0, \tag{4-12}$$

in which $u=\sum_{p=1}^{3}\int_0^{\omega_{p,\max}}f\hbar\omega D(\omega)d\omega$ is the phonon energy density, and the vector $\vec{q}=\sum_{p=1}^{3}\int_0^{\omega_{p,\max}}\hbar\omega D(\omega)V_{g,p}(\omega)\vec{k}\,f d\omega$ is the heat flux. For the equilibrium situation, u is equalized to E defined in Eq. (4-5) to get the pseudo-temperature $\tilde{T}$ appearing in $\langle n\rangle$. However, this is not the case when we are only concerned with the scattered phonons. It can be observed that

$$\frac{\partial u}{\partial t}=\frac{\partial}{\partial t}\left[\sum_{p=1}^{3}\int_0^{\omega_{p,\max}}f\hbar\omega D(\omega)d\omega\right]=\sum_{p=1}^{3}\int_0^{\omega_{p,\max}}\frac{\partial f}{\partial t}\hbar\omega D(\omega)d\omega, \tag{4-13}$$

and

$$\nabla_{\vec{r}}\cdot\vec{q}=\sum_{p=1}^{3}\int_0^{\omega_{p,\max}}\hbar\omega D(\omega)V_{g,p}(\omega)\vec{k}\cdot\nabla_{\vec{r}}f d\omega. \tag{4-14}$$

Comparing Eqs. (4-13) and (4-14), we obtain

$$\sum_{p=1}^{3}\int_0^{\omega_{p,\max}}\hbar\omega D(\omega)\frac{f-\langle n\rangle}{\tau(\omega)}d\omega=0,$$

or

$$\sum_{p=1}^{3}\int_{0}^{\omega_{p,\max}}\hbar\omega D(\omega)\frac{f}{\tau(\omega)}d\omega=\sum_{p=1}^{3}\int_{0}^{\omega_{p,\max}}\hbar\omega D(\omega)\frac{\langle n\rangle}{\tau(\omega)}d\omega, \tag{4-15}$$

which indicates that for scattered phonons the numerical inversion process to get $\widetilde{T}_s$ must be associated with $\sum_{p=1}^{3}\int_{0}^{\omega_{p,\max}}\hbar\omega D(\omega)\frac{\langle n\rangle}{\tau(\omega)}d\omega$ instead of the energy density E defined in Eq. (4-5). Under the gray-media approximation, $\tau(\omega)$ is a constant for all the phonons at the same temperature, and Eq. (4-15) will reduce to the case defined by Eq. (4-5). For the frequency-dependent model, however, cautions must be taken and Eq. (4-15) must be used to define the temperature of scattered phonons.

The phonons may also experience internal scatterings during their travels. These scatterings are processed at the end of each time step. The scattering probabilities, used to determine the occurrence of internal scattering events, are first computed based on the updated subcell temperature $\widetilde{T}$, phonon branch, and phonon frequency. The selection rule and detailed treatment of scattered phonons will be given later. Basically the simulation repeats the following procedures after the phonon initialization: phonon movement with possible interface or boundary scatterings, subcell temperature update with the new spatial distribution of phonon bundles, internal scattering treatment inside each subcell. Convergence is achieved when the calculated temperature profile no longer changes with time. After the convergence, the thermal conductivity of the studied structure can be derived from the domain dimension, the heat flowing through the domain, and the temperature difference across the domain.

4.3 Phonon Scattering Treatment

In MC simulations, phonon bundles may experience internal scatterings (by impurities, charge carriers, or other phonons) or interface scattering, where charge carrier scattering of phonons are normally neglected for lightly doped samples [19]. The detailed treatments are discussed below.

4.3.1 Internal Scattering Treatment

For internal scatterings, we assume that charge carrier scattering and impurity scattering only randomize the phonon bundle traveling direction, leaving the phonon frequency and velocity unchanged. In contrast, the phonon-phonon scattering, including the normal process (N process) and Umklapp process (U process), will reset all phonon states (its frequency, branch, velocity, and traveling direction) according to the current subcell temperature. This will help establish the thermal equilibrium between the scattered phonon bundle and the local temperature.

The phonon overall lifetime τ_T is calculated using the Matthiessen's rule, $\tau_T^{-1}(\omega) = \tau_I^{-1}(\omega) + \tau_N^{-1}(\omega) + \tau_U^{-1}(\omega) + \tau_{E(H)}^{-1}(\omega)$, where τ_I, $\tau_{E(H)}$, τ_N, τ_U are the relaxation times of impurity scattering, charge carrier scattering (τ_E for electrons, τ_H for holes), for N processes, and U processes, respectively. For lightly doped samples, the term $\tau_E^{-1}(\omega)$ or $\tau_H^{-1}(\omega)$ can be neglected. In Callaway's model [28], N processes were treated differently from other scattering mechanisms, by adding an associated correction term to the thermal conductivity. However, the refinement work by Holland [29] argued that this correction term would possibly cause more errors and N processes should be treated in exactly the same way as other scattering mechanisms. In this work, we follow Holland's treatment and N processes are simply a scattering mechanism added to other mechanisms. Additionally, the N process and the U process are not differentiated, and a combined relaxation time τ_{NU}, defined as $\tau_{NU}^{-1}(\omega) = \tau_N^{-1}(\omega) + \tau_U^{-1}(\omega)$, will be used. The probability for a phonon bundle to be scattered is given by $P(\omega) = 1 - \exp(-\Delta t / \tau_T(\omega))$ [18,19]. For an infinitesimal Δt, $P(\omega)$ simply becomes the weight $\Delta t / \tau_T(\omega)$ in Eqs. (4-7) and (4-8). At the end of every time step, a random number R_s ($0 \le R_s \le 1$) is generated for each phonon bundle at a frequency ω_0 and compared with $P(\omega_0)$. The phonon bundle is scattered if R_s is less than $P(\omega_0)$. If a phonon bundle is scattered, another random number R_{NU} will be generated and compared with $P_{NU}(\omega_0) = \tau_{NU}^{-1}(\omega_0) / \tau_T^{-1}(\omega_0)$. The phonon will have phonon-phonon scattering if

R_{NU} is less than $P_{NU}(\omega_0)$. Otherwise, it will be scattered by either charge carriers or impurities, which will only randomize its traveling direction.

Phonon-phonon scattering will reset all the states of a phonon bundle, which follows similar procedures as described by Eqs. (4-2) to (4-4). However, the spectrum $\langle n \rangle D(\omega)$ in Eqs. (4-2) and (4-3) should be replaced by $\langle n \rangle D(\omega)/\tau_{NU}(\omega)$ introduced in Eqs. (4-7) to (4-9). Because $1/\tau_{NU}(\omega)$ monotonically increases with ω, most phonons scattered are from the high-frequency portion of the phonon spectrum. At a fixed temperature, the averaged frequency of the phonons scattered by other phonons is

$$\langle \omega \rangle_s = \frac{\sum_{p=1}^{3} \int_0^{\omega_{p,\max}} \frac{1}{\tau_{NU}(\omega)} \hbar\omega \langle n \rangle D(\omega) d\omega}{\sum_{p=1}^{3} \int_0^{\omega_{p,\max}} \frac{1}{\tau_{NU}(\omega)} \hbar \langle n \rangle D(\omega) d\omega}, \tag{4-16}$$

which is higher than the averaged frequency of all the phonons at the same temperature, given as

$$\langle \omega \rangle_{eq} = \frac{\sum_{p=1}^{3} \int_0^{\omega_{p,\max}} \hbar\omega \langle n \rangle D(\omega) d\omega}{\sum_{p=1}^{3} \int_0^{\omega_{p,\max}} \hbar \langle n \rangle D(\omega) d\omega}. \tag{4-17}$$

In Ref. 19, Eqs. (4-2) and (4-3) were used to reset the states of a scattered phonon bundle. The phonon bundles experiencing phonon-phonon scattering are assigned frequencies averaged at $\langle \omega \rangle_{eq}$. We find that this treatment will result in a final phonon spectrum distorted from the real spectrum and will yield abnormal temperature profiles when the temperature difference across the domain is small. A simple test can be conducted with the equilibrium situation in which the 1D computational domain has both ends fixed at 300 K (isothermal wall boundary condition [19]). To simplify, the model used in this test only considers the U processes and impurity scattering [30]. The corresponding scattering rates are: $1/\tau_U(\omega) = B_1 \nu^2 T \exp(-B_2/T)$ (U process), where ν is the phonon frequency, B_1 = 3.0×10^{-19} s/K, B_2 =210 K; $1/\tau_I(\omega) = A\omega^4$ (impurity scattering), with A =2.4×10^{-45} s^3. The Debye model is used for the phonon dispersion, with $\omega_{LA,\max} = \omega_{TA,\max}$ =7.06×10^{13} rad·Hz, and the lattice constant a=5.5 Å. Due to the distorted

phonon spectrum from the equilibrium one, the resulting temperature profile always shows a valley in the middle (solid circles in Fig. 4.1), with a significantly increased number of phonon bundles from equilibrium. This problem is resolved when we use the spectrum $\langle n \rangle D(\omega)/\tau_{NU}(\omega)$ instead of $\langle n \rangle D(\omega)$ in Eqs. (4-2) and (4-3) to reset the scattered phonon states (empty circles in Fig. 4.1). This treatment is consistent with Eqs. (4-11) to (4-15), obtained from the BTE under the relaxation time approximation.

After processing all internal scatterings inside one single subcell, phonons will be either randomly created according to the spectrum $\langle n \rangle D(\omega)$ in Eqs. (4-2) and (4-3) or deleted from the domain. Our purpose is to assure the subcell energy conservation before and after the scatterings. The energy imbalance inside a subcell is controlled to be less than $\hbar\omega_{TA,\max}/2$.

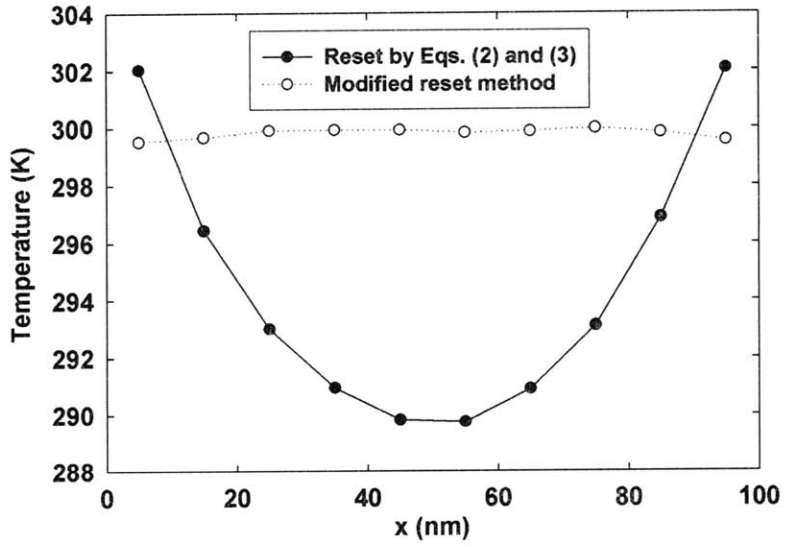

Figure 4.1 Calibration of the reset methods for scattered phonons [18]. The slight asymmetry and undulation of the temperature profiles are attributed to the numerical errors of MC simulations. The 1D computational domain is 100 nm in length and its both ends are fixed at 300 K (isothermal wall boundary condition [19]). The reset method based on Eqs. (4-2) and (4-3) always yields an abnormal temperature profile, which can be resolved by replacing the spectrum $\langle n \rangle D(\omega)$ with $\langle n \rangle D(\omega)/\tau_{NU}(\omega)$ in Eqs. (4-2) and (4-3). Here the time step is fixed at 1 ps and the temperature of each subcell is averaged over 0.5 ns.

4.3.2 Interface Scattering Treatment

For micro- and nanostructured materials, both the interface scattering and internal scattering can contribute to the thermal resistance of the material. We assume phonons are diffusely scattered at the interfaces. When a phonon bundle encounters an interface during its travel, it will be diffusely transmitted or reflected. For phonons incident from side 1 of the interface, this is determined by a random number P_r $(0 \le P_r \le 1)$ and the interface transmissivity T_{12} from side 1 toward side 2 [15,16,24]. The phonon bundle will be transmitted to side 2 if P_r is less than T_{12}. Otherwise, it will be reflected back to side 1. The reflected or transmitted phonon bundles are assigned a new traveling direction, with all other phonon states (velocity, frequency, and branch) unchanged, and hence phonon mode conversion is not included. For rectangular subcells, the direction reassignment within the anticipated semi-sphere for either reflection or transmission is simple. Equation (4-4) is again used to generate a direction vector $\vec{k}$ and then the sign of one particular component in $\vec{k}$ will be specified. It should be noted that θ should be determined by $\sin^2\theta = R_1$ instead of $\cos\theta = 2R_1 - 1$ in this case [16]. Suppose a phonon bundle moving in the positive x direction is transmitted across a y-z plane interface. It will have a positive x component in its new traveling vector $\vec{k}$. If it is reflected, the x component will be negative. Similarly, we can treat reflection and transmission on x-y and x-z plane interfaces. After the interface scattering, the phonon bundle will continue its movement with the remaining drift time to finish the current time step.

4.4 Boundary Condition

For a periodic structure, the boundary condition used for the numerical solution of the 2D BTE equation [9] can be extended to the 3D MC simulation. With a $L_x \times L_y \times L_z$ rectangular computational domain, heat is assumed to flow in the positive x direction. Our chosen unit cell is symmetric in both y and z directions. For such a symmetric structure, phonon bundles hitting the four side walls of the domain are specularly reflected [15,16,18,24]. If the unit cell structure is asymmetric in the y or z directions, we can use periodic boundary conditions for the corresponding side walls. In this case,

phonon bundles exiting from the domain on one side wall will re-enter the domain from the same interception position on the opposite side wall, and continue their travels. In the x direction, the essence of the boundary condition is that on both ends of the simulation domain, which we will call the hot and cold walls, the distortions of the distribution functions from the equilibrium distribution are periodic (shown in Fig. 4.2). This can be written as

$$f_2^-(\theta,\psi,\omega,y,z)-\langle n(y,z)\rangle_2 = f_1^-(\theta,\psi,\omega,y,z)-\langle n(y,z)\rangle_1, \tag{4-18}$$

$$f_2^+(\theta,\psi,\omega,y,z)-\langle n(y,z)\rangle_2 = f_1^+(\theta,\psi,\omega,y,z)-\langle n(y,z)\rangle_1, \tag{4-19}$$

in which f is the distribution function, θ is the polar angle, ψ is the azimuthal angle, the subscript "2" donates the cold wall ($x = L_x$) and "1" represents the hot wall ($x = 0$), the superscripts "+" and "-" represent the distribution in the positive and negative x directions. Here $\langle n(y,z)\rangle_1$ and $\langle n(y,z)\rangle_2$ are evaluated at the corresponding local wall temperatures. They are not periodic since their difference is the driving force for heat flow along the x direction.

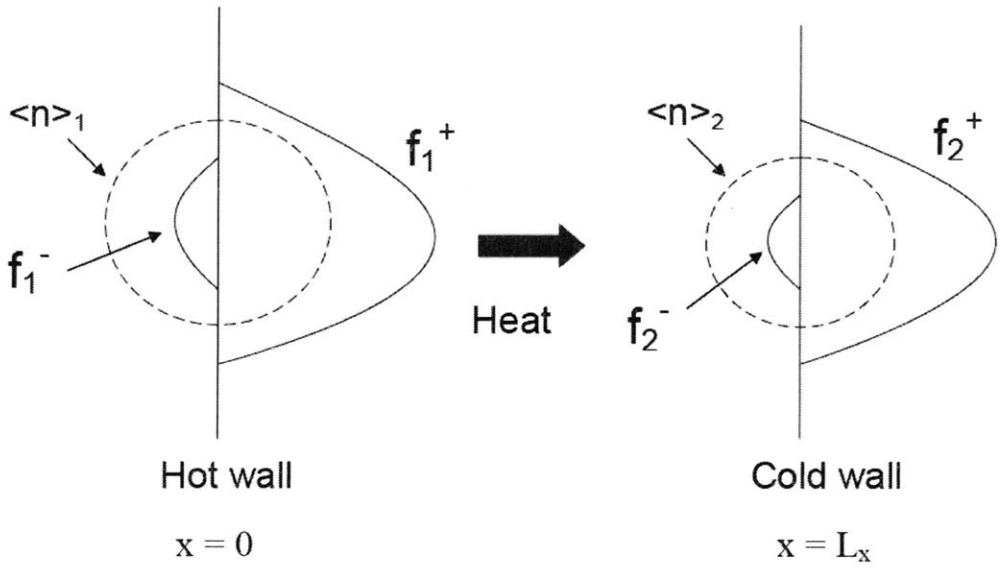

Figure 4.2 Distribution functions on the domain boundaries described by the periodic heat flux boundary condition. The hot wall and cold wall positions are located at $(0,y,z)$ and (L_x,y,z), respectively. The equilibrium distributions, $\langle n(y,z)\rangle_1$ and $\langle n(y,z)\rangle_2$, are both isotropic. With the x-direction heat flow, the distribution function f is anisotropic and distorted from $\langle n(y,z)\rangle$.

Equation (4-18) means when a phonon bundle, following the distribution function $f_1^-(\theta,\psi,\omega,y,z)$, encounters the hot wall during its movement, it will be "absorbed" by the wall. At the same time, a new phonon bundle, following the distribution function $f_2^-(\theta,\psi,\omega,y,z)$, will be emitted from the cold wall to maintain the heat flow through the domain. Similarly, Eq. (4-19) relates the distribution functions of phonon bundles "absorbed" by the cold wall and phonon bundles emitted from the hot wall. In our simulations, the absorbed phonons are recorded during tracking the phonon movement in each time step. The states of the emitted phonons are determined by Eqs. (4-18) and (4-19), as described below.

4.4.1 Cold Wall Emission

In Eq. (4-18), $f_2^-(\theta,\psi,\omega,y,z)$ represents the distributions of phonons entering the simulation domain, which we call emitted phonons. The distribution of these emitted phonons is determined by $f_1^-(\theta,\psi,\omega,y,z)$, the distributions of phonons leaving the domain from the hot wall, or absorbed phonons. In the y-z plane, a fixed cross section area A is assigned for all subcells. Denoting unit vector $\vec{n}$ as the normal of the wall, $\vec{k}$ as the phonon traveling direction, we multiply $\left(V_{g,p}(\omega)\vec{k}\cdot\vec{n}\right)D(\omega)A\Delta t$ to both sides of Eq. (4-18) and integrate with respect to ω, and ψ, θ for 2π solid angle. Summation over the three acoustic branches and rearranging the equation yields

$$N_2^-(y,z)=N_1^-(y,z)-\frac{1}{4W}\sum_{p=1}^{3}\int_0^{\omega_{p,\max}}V_{g,p}(\omega)D(\omega)A\Delta t\left(\langle n(y,z)\rangle_1-\langle n(y,z)\rangle_2\right)d\omega, \qquad (4\text{-}20)$$

where W is the number of phonons in each bundle, $N_1^-(y,z)$ is the number of locally absorbed phonon bundles on the hot wall, $N_2^-(y,z)$ is the number of phonon bundles locally emitted by the cold wall. Similarly, multiplying $\hbar\omega\left(V_{g,p}(\omega)\vec{k}\cdot\vec{n}\right)D(\omega)A\Delta t$ to both sides of Eq. (4-18) and conducting similar procedures yields

$$Q_2^-(y,z)=Q_1^-(y,z)-\frac{1}{4W}\sum_{p=1}^{3}\int_0^{\omega_{p,\max}}\hbar\omega V_{g,p}(\omega)D(\omega)A\Delta t\left(\langle n(y,z)\rangle_1-\langle n(y,z)\rangle_2\right)d\omega, \qquad (4\text{-}21)$$

in which $Q_2^-(y,z)$ is the total phonon bundle energy locally emitted from the cold wall for area A, $Q_1^-(y,z)$ is the total phonon bundle energy absorbed by the hot wall.

In our simulations, all the $N_1^-(y,z)$ phonon bundles are deleted from the domain but their states are separately stored as a pool for the cold wall emission. The phonon states include its frequency, velocity, location intercepting the wall, the remaining drift time after hitting the wall, and its traveling direction. To obtain the $N_2^-(y,z)$ phonon bundles, we need to delete

$$N_{del} = \frac{1}{4W}\sum_{p=1}^{3}\int_0^{\omega_{p,\max}} V_{g,p}(\omega)D(\omega)A\Delta t\left(\langle n(y,z)\rangle_1 - \langle n(y,z)\rangle_2\right)d\omega \tag{4-22}$$

phonon bundles from the pool consisting of $N_1^-(y,z)$ phonon bundles. To do this, N_{del} phonons are first randomly generated according to the spectrum $V_{g,p}(\omega)D(\omega)\left(\langle n(y,z)\rangle_1 - \langle n(y,z)\rangle_2\right)$, which replaces $\langle n\rangle D(\omega)$ in Eqs. (4-2) and (4-3) for phonon state determination in this situation. Among the $N_1^-(y,z)$ phonon bundles, we delete N_{del} bundles that best match the frequencies and branches of the generated bundles. The states of these N_{del} bundles are saved for later usage, which will be clear when the hot wall emission is discussed. The phonons left in the pool constitute the $N_2^-(y,z)$ phonons emitted from the cold wall.

4.4.2 Hot Wall Emission

Similar to Eq. (4-20), the hot wall emission can be derived from Eq. (4-19)

$$N_1^+(y,z) = N_2^+(y,z) + \frac{1}{4W}\sum_{p=1}^{3}\int_0^{\omega_{p,\max}} V_{g,p}(\omega)D(\omega)A\Delta t\left(\langle n(y,z)\rangle_1 - \langle n(y,z)\rangle_2\right)d\omega, \tag{4-23}$$

in which $N_2^+(y,z)$ phonon bundles are absorbed by the cold wall, and they are known for each time step. The previous N_{del} phonon bundles deleted from the cold wall emission pool, with their traveling directions reversed this time, will be added to the $N_2^+(y,z)$ bundles and thus form the $N_1^+(y,z)$ bundle pool for the hot wall emission.

4.4.3 Periodic Heat Flux with a Constant Virtual Wall Temperature Boundary Condition

Based on the foregoing discussions, a novel periodic heat flux with a constant virtual wall temperature boundary condition can be introduced for periodic structures. We assign $T_1(y,z) \equiv T_h$ to the hot wall and $T_2(y,z) \equiv T_c$ to the cold wall of the domain. By combining such temperature setting with periodic boundary conditions used in Eqs. (4-18) and (4-19), the local heat flux q'' is allowed to vary across each virtual wall but still hold its periodicity, $q''(0,y,z) = q''(L_x,y,z)$. It should be noted that our boundary condition is fundamentally different from the traditional isothermal wall boundary condition [19]. In the latter case, the computational domain is sandwiched between two physical black walls. For a periodic structure, the isothermal wall boundary condition requires a computational domain consisting of many periods to eliminate the strong end effects. The exact thermal conductivity can be obtained only if the calculation results will no longer change with further increasing the number of periods inside the computational domain. In contrast, our boundary condition is specified on two "virtual" walls cut arbitrarily inside the material without affecting the real heat flow, as long as the virtual walls define an integer multiple of unit cells of the periodic structure. In principle, accurate thermal conductivities can be obtained using a single period as our computational domain. This will significantly reduce the computational cost. Our calculation validates this point.

4.5 Results and Discussion

The previous sections cover the basic simulation procedure, the treatment of different phonon scatterings, and the employed boundary condition for a periodic structure. With these, we are ready to use frequency-dependent MC simulations to investigate the phonon transport in various periodic structures. My calculations here are focused on silicon-based materials, including 2D micro- to nano-porous silicon and 3D silicon nanocomposites.

4.5.1 Employed Models for Different Scattering Mechanisms

To get dependable simulation results, it is necessary to use accurate frequency-dependent phonon lifetimes in silicon. In literature, Holland's model [29] provided a very good fit to the experimental data from 1.7 to 1300 K. However, in his work the real phonon dispersion was simplified as two linear sections for both TA and LA branches, resulting in abrupt changes of phonon group velocities across the threshold frequencies between two linear sections (ω_1 for two TA branches, ω_4 for the LA branch). In addition, the phonon-phonon scattering rates employed different expressions for the TA branches below and above ω_1. As a result, the calculated phonon MFPs had a significant jump across the threshold frequencies. Although the first problem was fixed using the real phonon dispersion [19], the second issue still remained and led to a TA phonon MFPs jump from 9 nm to 179 nm at ω_1 for Si. Henry and Chen carried out molecular dynamics simulations to study the spectral dependence of phonon MFPs in silicon [31]. The results of this past work are now incorporated into the MC simulations. Based on their calculations from 300 to 1000 K, the combined relaxation time for the N and U processes follows the expression $\tau_{NU} = A_{NU}\nu^{-2}T^{-b}$, where ν (in Hz) is the phonon frequency, $A_{NU} = 5.32\times10^{18}$ $K^{1.49}/s$, b $=1.49$ for LA phonons; and $A_{NU} = 5.07\times10^{18}$ $K^{1.65}/s$, b $=1.65$ for TA phonons. To simplify the simulation, an isotropic phonon dispersion is assumed and the calculated (001) direction phonon dispersion is used to evaluate the frequency-dependent phonon group velocity and density of states. The whole phonon spectrum (from 0 to $\omega_{LA,\max}$) is discretized into N_b equally spaced intervals. Numerical integrations with respect to the phonon frequency, such as the evaluation of Eq. (4-5), are all conducted by summing the integrals over all N_b intervals, in which the integrals are evaluated at the central frequency of each interval.

For doped bulk silicon, the impurity-phonon scattering should be considered in addition to the phonon-phonon scattering. The phonon scattering rate by impurities is expressed as [32]

$$\tau_I^{-1}(\omega) = A\omega^4, \tag{4-24}$$

where the constant $A = A_{\delta M} + A_{\delta R} + A_x$ [33]. Here $A_{\delta M}$, $A_{\delta R}$, A_x correspond to the scattering due to the presence of impurity atoms, the induced strain by inserting impurity atoms into the lattice, and unintentional impurities and imperfections, respectively. The employed phonon dispersion suggests an average sound velocity as $v_s = \left\{\left[2v_{TA}^{-1} + v_{LA}^{-1}\right]/3\right\}^{-1}$=6127 m/s and this v_s is used to compute $A_{\delta M}$ and $A_{\delta R}$. All other parameters are unchanged from Ref. 33 that uses v_s=6400 m/s instead.

For free charge carrier scatterings of phonons (only considered for heavily doped samples), the scattering rate is given by Ziman [34,35] as

$$\tau_E^{-1}(\omega) = \frac{E_d^2 m^{*3} v_g}{4\pi\hbar^4 d} \frac{k_B T}{\frac{1}{2} m^* v_g{}^2} \times \left\{ \frac{\hbar\omega}{k_B T} - \ln \frac{1 + \exp\left[\left(\frac{1}{2} m^* v_g{}^2 - E_F\right)/k_B T + \hbar^2\omega^2/8m^* v_g{}^2 k_B T + \hbar\omega/2k_B T\right]}{1 + \exp\left[\left(\frac{1}{2} m^* v_g{}^2 - E_F\right)/k_B T + \hbar^2\omega^2/8m^* v_g{}^2 k_B T - \hbar\omega/2k_B T\right]} \right\}, \quad (4\text{-}25)$$

where T is the absolute temperature, $\hbar$ is the Planck constant, k_B is the Boltzmann constant, E_d is the acoustic deformation potential, m^* is the density of states effective mass, d is the density, v_g is the averaged phonon group velocity, and E_F is the Fermi energy calculated by the generalized Kane's model based on the carrier concentration [36,37]. Because the investigated silicon nanocomposites always have a carrier concentration much higher than the carrier concentration threshold 3.0×10^{18} cm^{-3} for becoming metallic [38,39], the scattering of phonons by bound electrons or holes will not be considered.

Given the relaxation times of different mechanisms, the lattice thermal conductivity of bulk silicon can be calculated by [25,29]

$$k_L = \frac{1}{3}\sum_{p=1}^{3}\int_0^{\omega_{p,\max}} C_p(\omega) V_{g,p}^2(\omega)\tau_{T,p}(\omega)d\omega, \tag{4-26}$$

where the subscript p indicates the polarization, $C_p(\omega)$ is the spectral volumetric specific heat, $V_{g,p}(\omega)$ is the phonon group velocity, and $\tau_{T,p}(\omega)$ is the overall phonon relaxation time for branch p and frequency ω.

4.5.2 Calibration for Bulk Silicon

The MC code developed is first calibrated with bulk silicon and only phonon-phonon scattering is considered. In this case, Eq. (4-26) predicts bulk k_L=146.5 W/m·K at 300 K. Because we only employ the phonon dispersion along the (001) direction for our calculations, this isotropic k_L value is lower than the prediction averaged in three major crystal directions by Henry and Chen (175 W/m·K by the BTE approach, 166 W/m·K by the Green-Kubo analysis), in which the phonon density of states (used in calculating $C_p(\omega)$) are summed over the Brillouin zone.

With N_b=2000, phonon bundle size W=2, T_h=305 K and T_c=295 K are assigned to a rectangular computational domain that is 200 nm in length, and 10 nm ×10 nm for the cross section area. The time step Δt is fixed at 0.6 ps in this simulation. After 1 ns, the temperature profile (averaged over successive 800 time steps) converges and its variation in the following steps is within 0.5 % (Fig. 4.3). The linearity for the converged temperature profile is R^2=0.9987. The heat flow passing through the domain always fluctuates due to the randomness of phonon absorption by the hot and cold walls at different time steps. This heat flow is obtained by averaging the net heat flows across the two walls, which are $Q_2^+ - Q_2^-$ for the cold wall and $Q_1^+ - Q_1^-$ for the hot wall. After the convergence of the temperature profile, the heat flows at different time steps are further averaged over a period, with the highest and lowest 20 values excluded. To be accurate, the averaging period is chosen to be no shorter than the time for the temperature profile to converge. The lattice thermal conductivity can then be calculated with this averaged heat flow and the temperature difference across the domain. Averaging over a period of 16 ns yields a thermal conductivity of 142.9 W/m·K, which is slightly lower than the expected 146.5 W/m·K. In comparison, averaging the heat flows over any 2.4 ns period after the

initial 1 ns gives thermal conductivities ranging from 141.8 to 145.4 W/m·K, all with less than 4% relative error. At 300 K, our employed model predicts that around 53% of the lattice thermal conductivity is contributed by phonons with MFPs larger than the 200 nm domain length. The chances for these phonons to be scattered are relatively small but their contributions can still be included by averaging the results over a long period of time.

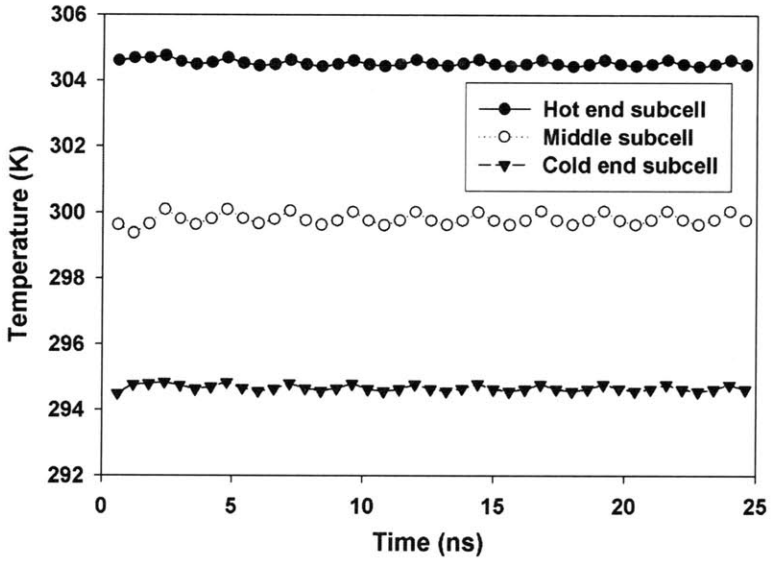

Figure 4.3 The time history of subcell temperatures for a pure silicon computational domain [18]. The 200 nm×10 nm×10 nm domain consists of 20 cubic subcells that are 10 nm in dimension. The subcell adjacent to the hot wall (hot end subcell), the one adjacent to the cold wall (cold end subcell), and the middle one are tracked here. Every temperature point is averaged over the previous 800 time steps, or 0.48 ns.

One important aspect of the statistical MC simulation is the signal-to-noise ratio, which is mainly reflected in the fluctuation of the heat flowing through the domain at different time steps. Such fluctuations can always be decreased by reducing the bundle size. However, this also requires a significantly larger computer memory that is not feasible in many cases. Averaging the heat flow over a longer period of time can be used to compensate the errors brought by large bundle sizes but requires more computational time. In practice, a balance between computation time and computer memory usage is required. The temperature difference between the cold wall and the hot wall can be increased to improve the signal-to-noise ratio, mainly by increasing the signal (averaged

heat flow). The accuracy of the calculation will be slightly affected because in this case the thermal conductivity is an effective value averaged over a wider temperature range and does not correspond well to a particular temperature.

4.5.3 Two-Dimensional Porous Silicon with Aligned Pores

Although it is one of the most important materials in the electronics industry, silicon is unsuitable for some applications because of its high thermal conductivity. Porous silicon, with its much lower thermal conductivity, could provide a simple solution to widen the usage of silicon [40-43]. Along this line, nanoscale porous structures are expected to introduce strong phonon size effects and further lower the thermal conductivity from the prediction based on the classical Fourier heat conduction theory. Surprisingly, experimental results showed that even microsize periodically arranged through-film pores would still yield notable phonon size effects in silicon thin films [17]. This reduction in thermal conductivity cannot be explained using an averaged phonon MFP that is on the order of a hundred nanometer. To better understand the phonon size effects in porous silicon, we carry out frequency-dependent MC simulations on 2D porous silicon with periodically arranged square pores, in which the pore dimensions range from 5 nm to 2 μm.

It is assumed that phonons are all specularly reflected on the z-direction, i.e., the top and bottom surfaces of the film shown in Fig. 4.4(a). This choice of the z-direction boundary condition converts the problem into a 2D case where the z-direction film thickness will not affect the results. The purpose of choosing this boundary condition is to reduce the computational load since a small z-direction dimension can be chosen (1 to 10 nm for all cases). Figure 4.4(b) presents the simulated film structure with the chosen computational domain, which is a square-shape period in the x-y plane, with a square pore in its center. All phonons encountering the rough pore boundaries are reflected diffusely. The silicon film is assumed to be n-type with a doping level as 5×10^{15} cm^{-3}. The electronic thermal conductivity is negligible (<0.01 W/m·K from the Wiedemann-Franz Law) for this low doping level and the electron-phonon scattering can also be neglected. The constant A for impurity scattering is determined as 9.3×10^{-50} s^3, with A_x as zero for slightly doped samples [33].

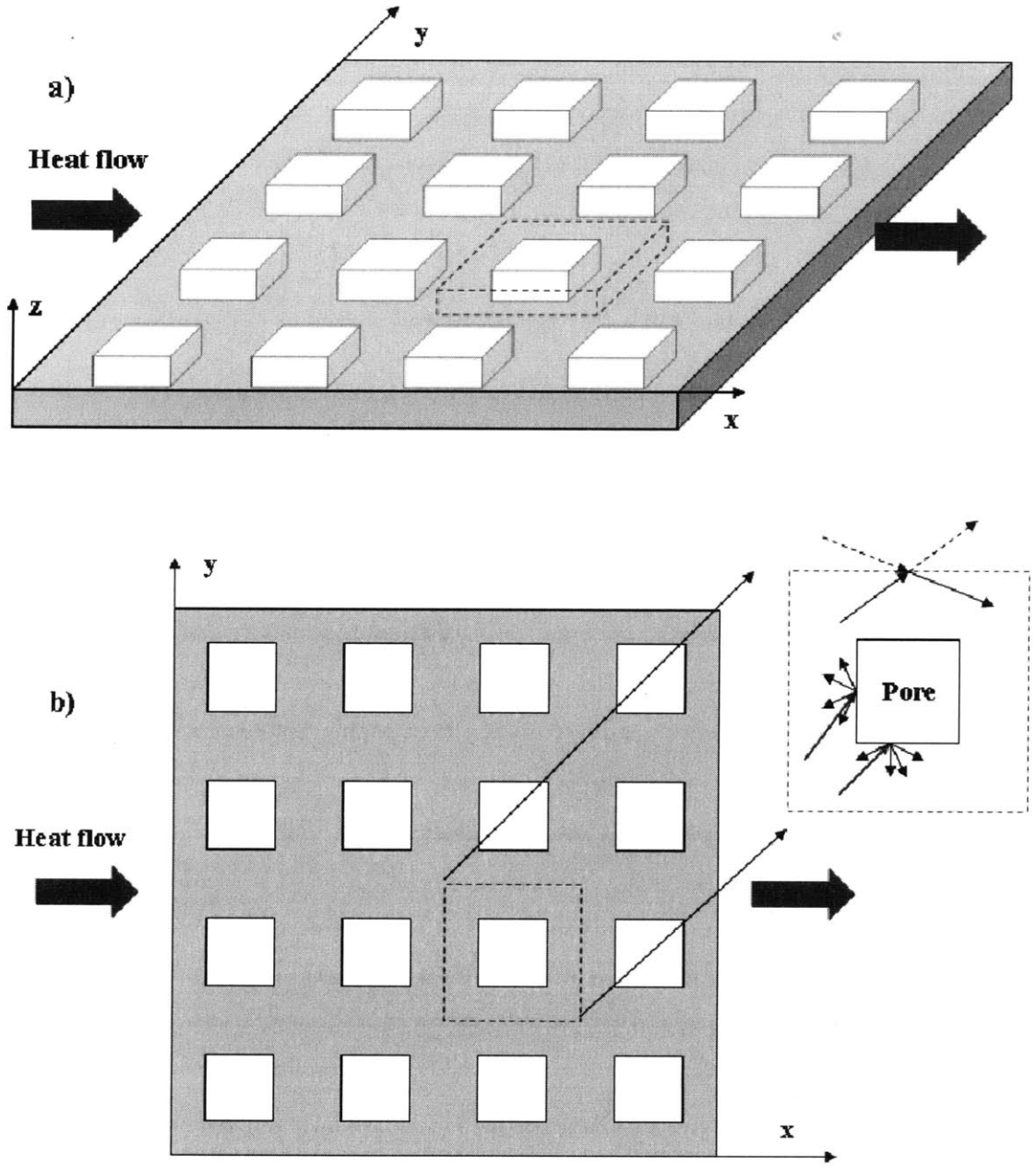

Figure 4.4 a) Structure of the simulated porous silicon film [18]. The chosen computation domain (marked by dashed line) is a single period with a square pore right in its center. b) Top view of the film, with details of the computational domain.

Based on the used parameters, the corresponding bulk lattice thermal conductivity is slightly reduced to 145.9 W/m·K according to Eq. (4-26). In our simulations, the period of the pores always equals twice the square pore size, resulting in a fixed porosity $\Phi = 0.25$. Without considering the phonon size effects, the Eucken model [44] from the Fourier classical heat conduction theory predicts

$$k_{Porous} / k_{Solid} = (1-\Phi)/(1+\Phi/2) \tag{4-27}$$

for cubic pores, and the calculated k_{Porous} is 97.3 W/m·K.

A 10 K temperature difference is applied to the computational domain for cases with period sizes up to 1 μm. To improve the signal-to-noise ratio, the temperature difference is increased to 20 K for larger period sizes. The normalized temperature contour for the 200-nm-period case is shown in Fig. 4.5(a), with subcells chosen as 5 nm cubes. The normalization is performed as $(T - T_{\min})/(T_{\max} - T_{\min})$, where T is the subcell temperature, and the subscripts max and min denote the maximum and minimum temperatures of subcells. Figure 4.5(b) presents the x-direction normalized temperature distribution at a few typical y locations. When the spacing between adjacent pores is smaller than the phonon MFPs, ballistic phonon transport becomes more important compared with the internal phonon scatterings inside silicon. Therefore, close to the left surface of the pore (facing the incoming heat flow) there will be a locally heated region because it receives hotter phonons directly from the "upstream" adjacent pore. Similarly, a locally cooled region will exist close to the back surface of the pore. In both cases, we will have a negative local temperature gradient compared with the main x-direction temperature gradient across the whole domain. These local "overshoots" do not violate the second law of thermodynamics because no local thermal equilibrium is established under the strong phonon ballistic transport [9,16].

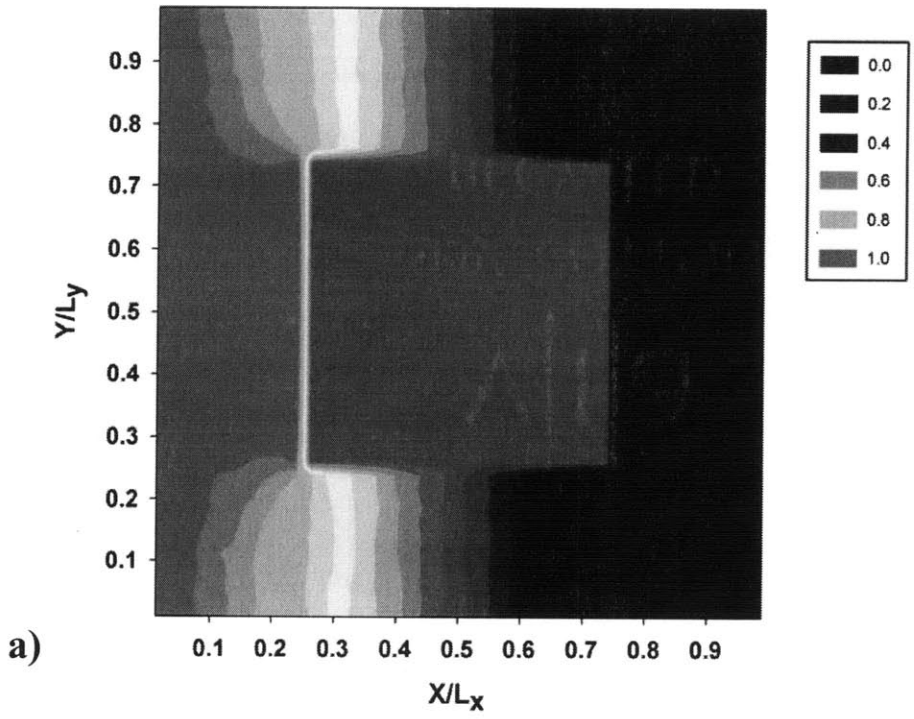

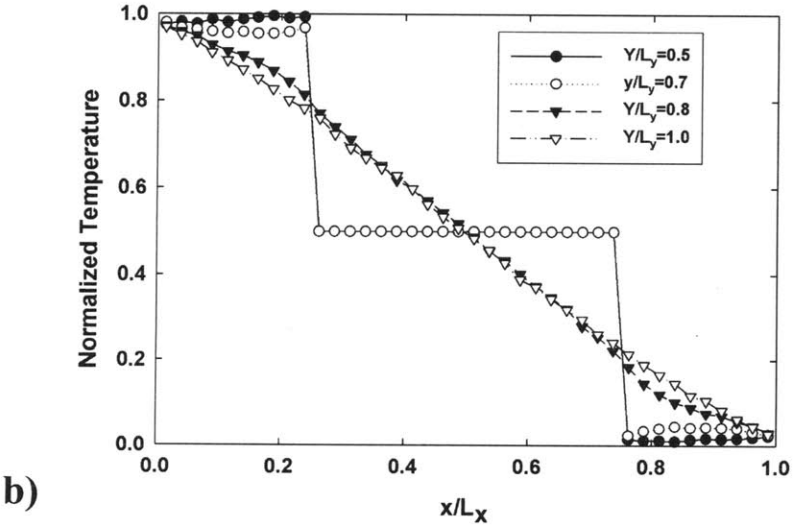

Figure 4.5 (a) Normalized temperature contour for a 200 nm period [18]. The empty pore region is assigned the average temperature of the domain. (b) Temperature distribution along the x direction for typical y locations.

The room-temperature in-plane lattice thermal conductivities, averaged over at least 4 ns after the convergence of the temperature profile, are plotted as a function of period size in comparison with the Eucken model prediction (Fig. 4.6).

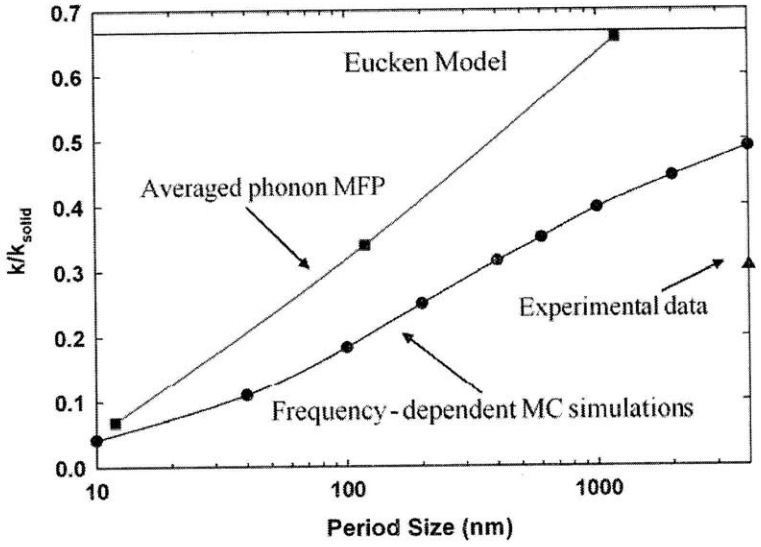

Figure 4.6 Normalized in-plane lattice thermal conductivities of porous silicon films as a function of period size [18]. The circles are the frequency-dependent MC simulation results. The squares are results by solving the BTE for the same 2D unit cell [12], with an averaged phonon MFP and isothermal wall boundary condition [19] applied. The triangle is Song's experimental result of a 4.49 μm thick silicon film with similar doping level, 2.3 μm pore diameter, 4 μm pore spacing, and a corresponding porosity $\Phi = 0.26$ [17]. The Eucken model prediction (solid line) is plotted for comparison.

To clearly show the thermal conductivity reduction, all the values are normalized by the bulk thermal conductivity k_{Solid} (145.9 W/m·K). Remarkable phonon size effects can be observed even for a period size of 4 μm, which is one magnitude larger than the averaged phonon MFP of 119 nm at 300 K. In comparison, solving the BTE based on the gray-media approximation suggests k_{Porous} / k_{Solid} to be around 0.66 (shown in Fig. 4.6) for exactly the same 2D unit cell with a phonon Knudsen number of 0.1, where the Knudsen number is defined as the averaged phonon MFP divided by the period size [12]. Although isothermal wall boundary condition [19] is used instead of the periodic heat flux boundary condition to solve the BTE, this comparison clearly shows that phonon

size effects cannot be accurately predicted without considering the frequency-dependent phonon MFPs.

Song et al. reported a 44.5 W/m·K (also shown in Fig. 4.6) lattice thermal conductivity at 300 K for a 4.49 μm thick silicon film with similar doping level, 2.3 μm pore diameter, 4 μm pore spacing, and a corresponding porosity $\Phi = 0.26$ [17]. Our current prediction is still higher than this result, which can be mainly attributed to two factors. First, our simulation is 2D while the phonon scattering at the film top and bottom surfaces are mostly diffuse [19]. We expect such diffuse scattering should further reduce the thermal conductivity. Secondly, during the process of drilling through-film pores, damaged surface layer may be created by the ion bombardment of the deep reactive-ion etching [17], and effectively increase A_x. The pore shape difference is not expected to be very important because of the phonon diffuse scattering on the pore boundaries and similar porosities. Despite the difference, our simulation shows that indeed size effects exist even in micron range, consistent with experimental observations. Contribution of long-MFP phonons to the thermal conductivity is significantly suppressed by the scattering of periodically arranged pores, and such influence can be predicted only if frequency-dependent phonon MFPs are considered.

4.5.4 Silicon Nanocomposites

To simulate the phonon transport inside nanocomposites, another critical parameter is the phonon transmissivity across interfaces. Because no general theoretical expression is available for the frequency-dependent transmissivity on a given interface, we simply assume a frequency-independent transmissivity in simulations. Based on the diffuse mismatch model, the interface transmissivity from material 1 to material 2 is given by

$$T_{12}(T) = \frac{U_2(T)v_2}{U_1(T)v_1 + U_2(T)v_2}, \tag{4-28}$$

in which v and U are the averaged phonon group velocity and energy density at a given temperature T, respectively [45-47]. For interfaces between two grains of the same material, the transmissivity is fixed at 0.5. At 575 K, an average phonon transmissivity

$\langle T \rangle = 0.57$ is given by molecular dynamics simulations for silicon grain interfaces [48], which is close to our estimation.

The studied n-type silicon nanocomposites were synthesized in two steps as described in literature [2-8]. We first prepared nanopowders by high energy ball milling bulk silicon together with the doping element chunks (3% phosphorous in mole). Secondly, we hot-pressed the obtained $Si_{1.00}P_{0.03}$ nanopowders into a bulk disc and measured its thermoelectric properties with commercial setups. The ZT of the investigated sample reaches its peak around 0.55 at 1173 K. The averaged grain size in the sample is determined as 200 nm by transmission electron microscopy. In MC simulations, parameters used for silicon nanocomposites are listed in Table 4.1. The lattice thermal conductivity k_L is calculated by subtracting the electronic contribution k_e from the measured thermal conductivity (Fig. 4.7). Here k_e is calculated by the Wiedemann-Franz law, $k_e = L\sigma T$, where L is the computed Lorenz number [37], σ is electrical conductivity, and T is absolute temperature. Due to large grain sizes, we do not consider the grain interface influence on Lorenz numbers. In heavily doped n-type silicon (n>1.0×10^{18} cm^{-3}), shallow impurity levels within the band gap start to merge with the conduction band so that the dopants are always completely ionized [49]. Therefore, we assume n is fixed at the dopant concentration for all temperatures. The Fermi level E_F in Eq. (4-25) is calculated according to the n value.

Table 4.1 Parameters used for silicon nanocomposites. Temperature-dependent band gap E_g is used to calculate E_F based on fixed electron concentration n. The electron density of states effective mass is calculated for the lowest conduction band valley. The sound velocity is averaged over TA and LA branches as $v_g = \left\{\left[2v_{g,TA}^{-1} + v_{g,LA}^{-1}\right]/3\right\}^{-1}$.

E_d (eV) [49]	m^* (m_0)	v_g (m/s)	Band gap E_g (eV) [50]	d (kg/m^3)	n (cm^{-3})
9.5	1.06	6127	$1.17 - 4.73\times10^{-4}T^2/(T+636)$	2327	3.93×10^{20}

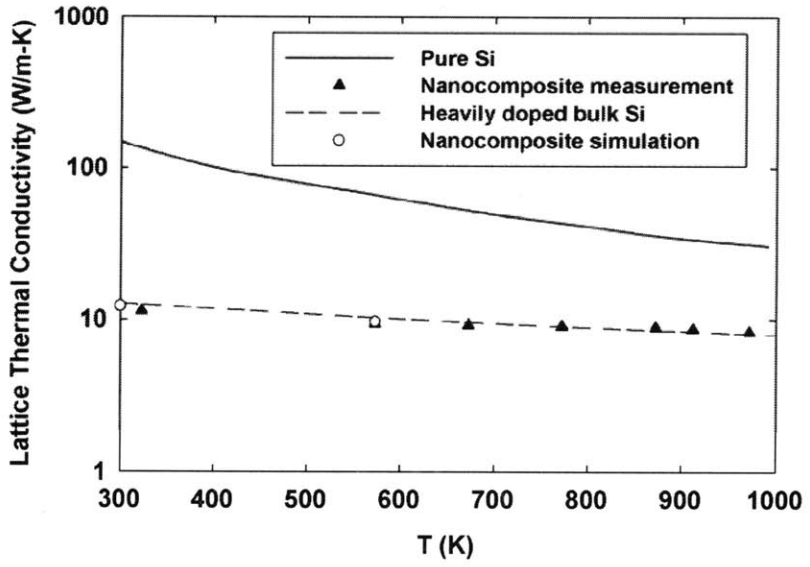

Figure 4.7 Lattice thermal conductivities of pure silicon (solid line), measured silicon nanocomposite (filled triangles), calculated heavily doped bulk silicon with electron concentration fixed at n =3.93×10^{20} cm^{-3}, and phonon-impurity scattering coefficient A =1.0×10^{-43} s^3 (dashed line), and simulated 200-nm-grain-size nanocomposite with the same n, A values (empty circles).

Despite the variation of grain shapes inside nanocomposites, we can approximate the structure as packed equal-sized cubes. To avoid conflicts between our boundary condition and grain interface scatterings of phonons, the chosen computational domain boundary must be away from grain interfaces. Here the computational domain is chosen as a cube consisting of eight adjacent cubes, each of which is 1/8 of a cubic grain. In heavily doped polycrystalline silicon, unintentional impurities and imperfections will contribute to impurity scattering and significantly increase the effective A value [51]. Therefore, we cannot predict A based on the doping concentration and A is normally treated as a fitting parameter in analysis. By matching simulation results (empty circles in Fig. 4.7) with experimental data (filled triangles) at 300 and 573 K, the phonon-impurity scattering coefficient is determined as A =1.0×10^{-43} s^3, which is on the same order as pervious studies for polycrystalline silicon with similar grain sizes [51]. The divergence between simulation and experimental results is within 6% at both temperatures. Because of the strong internal scatterings of phonons, we find that grain interface scatterings only slightly affect the phonon transport in this nanocomposite. To

compare, we use Eq. (4-26) to calculate the lattice thermal conductivities of bulk silicon with the same internal scatterings of phonons (dashed line in Fig. 4.7). At 300 and 573 K, adding grain interfaces will only reduce the lattice thermal conductivity by less than 6% from its bulk counterpart. The weak influence of grain interfaces can be understood from Fig. 4.8, which shows the accumulative contributions of phonons with different MFPs to the lattice thermal conductivity. Figure 4.8 indicates that phonons with MFPs longer than 60 nm contribute negligibly to the lattice thermal conductivity at 300 K. At elevated temperatures, internal scatterings of phonons inside grains are significantly enhanced and thus the influence of grain interfaces becomes even weaker. Without conducting time-consuming MC simulations, we can obtain reasonable agreement between our experimental results and calculated lattice thermal conductivities of heavily doped bulk silicon (Fig. 4.7).

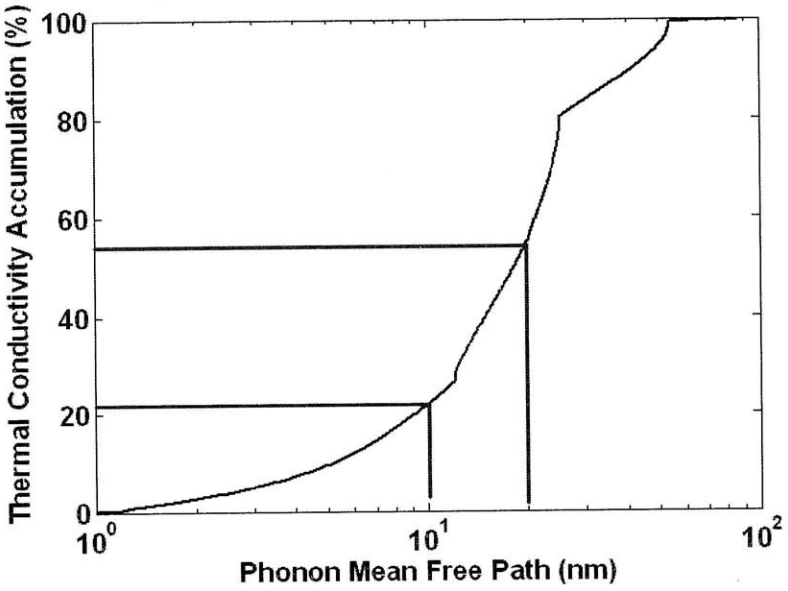

Figure 4.8 Room-temperature accumulated thermal conductivity of heavily doped bulk silicon, with electron concentration fixed at n =3.93×10^{20} cm^{-3}, and phonon-impurity scattering coefficient A =1.0×10^{-43} s^3. The accumulation percentage $\alpha(\Lambda)$ is defined as the percentage of lattice thermal conductivity that is contributed by phonons with MFP less than Λ [31]. From the curve, we can observe that more than 40% of the lattice thermal conductivity is contributed by phonons with MFPs larger than 20 nm, while close to 80% of the lattice thermal conductivity is from phonons with MFPs larger than 10 nm.

To take advantages of the interface scattering of phonons, much smaller grain sizes are required. At 300 K, we find that the room-temperature lattice thermal conductivity can be dropped to 3.0 W/m·K if grain sizes can be reduced to 10 nm, as shown in Fig. 4.9. More accurate calculations may further consider the change of A in such small grains with more complicated strain patterns. Due to dominant grain interface scattering, the lattice thermal conductivities for 10 nm grain sizes are insensitive to temperature variations [Fig. 4.10(a)]. Because Ref. 31 only provided phonon-phonon scattering rates from 300 to 1000 K for our simulations, the lattice thermal conductivity at 1173 K is linearly extrapolated from simulation results for 973 and 773 K. Slight inaccuracy is expected in this treatment due to the weak temperature dependence of lattice thermal conductivities in 10-nm-grain-size samples.

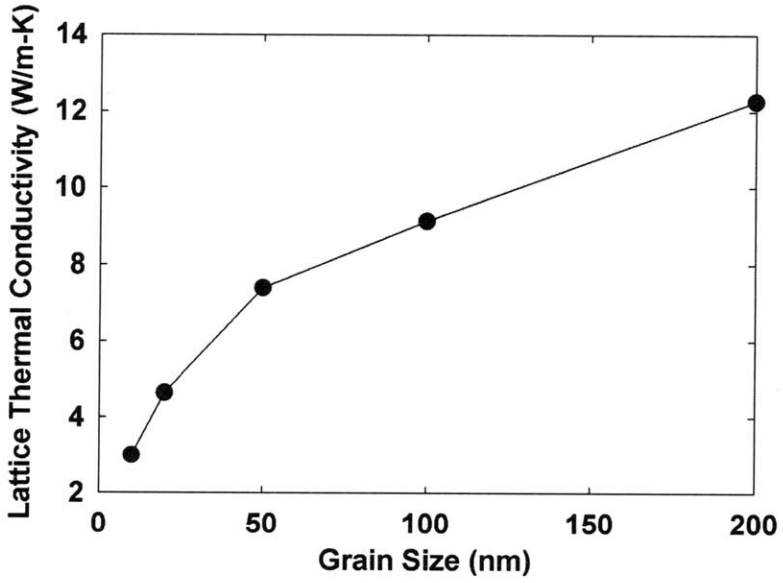

Figure 4.9 Grain size dependence of room-temperature lattice thermal conductivities for silicon nanocomposites with $n=3.93\times10^{20}$ cm^{-3}, $A=1.0\times10^{-43}$ s^3. For 200 nm grain sizes, the lattice thermal conductivity is already close to the bulk value of 12.7 W/m·K.

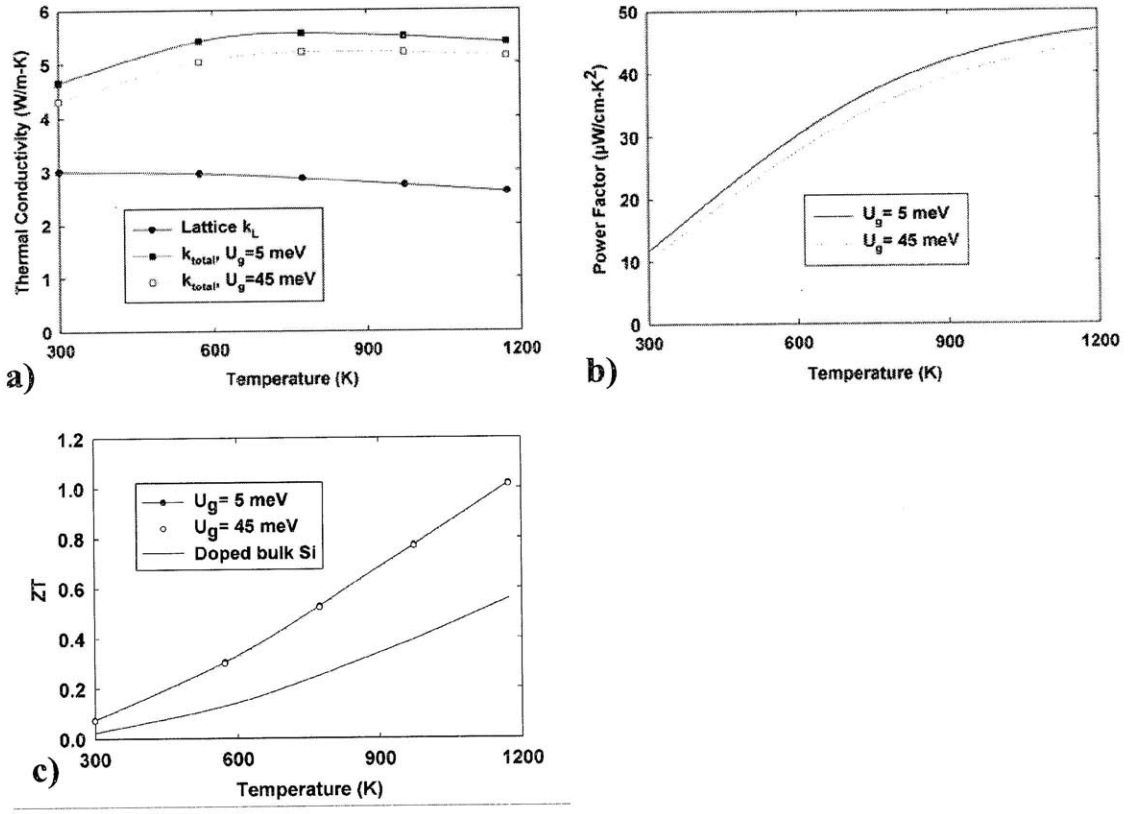

Figure 4.10 (a) Predicted thermal conductivities of a silicon nanocomposite with 10 nm grain sizes. Two typical grain interface barrier heights (5, 45 meV) are considered here. The lattice thermal conductivity at 1173 K is linearly extrapolated from the results for 773 and 973 K. (b) Power factors predicted by the model developed in Ref. 52. (c) Predicted thermoelectric figure of merit (ZT) for above two cases and corresponding heavily doped bulk silicon.

For charge carrier transport inside nanocomposites, we have developed a model based on the Boltzmann transport equation under the relaxation-time approximation [52]. The total relaxation time τ for all the scattering mechanisms is obtained by adding up the scattering rates τ_i using Matthiessen's rule $\tau^{-1} = \sum_i \tau_i^{-1}$ [25,50]. Inside a gain, carriers are scattered by acoustic lattice vibrations and ionized impurities [50,52]. On grain interfaces, charge carriers are scattered by a potential barrier created by charges trapped on the interfaces. The grain interface scattering of charge carriers is included into our model by identifying a scattering potential and calculating the corresponding scattering rate, which is then added to the scattering rates of other two mechanisms. Assuming the

parameters in Table 4.1 are unchanged for 10 nm grain sizes, we use the same model to predict k_e and power factors $S^2\sigma$ [Fig. 4.10(b)] for two typical grain-interface energy barrier heights U_g (5, 45 meV [52]). The corresponding total thermal conductivities are plotted in Fig. 4.10(a). Despite the difference in particular properties, two barrier heights yield almost identical ZT curves with a maximum as 1.02 at 1173 K, shown in Fig. 4.10(c). Figure 4.10(c) also shows the predicted ZT of the bulk counterpart, with k_L from Holland's model and electrical properties predicted for U_g=0 eV in our electron transport model. The peak ZT at 0.56 is similar to our measured nanocomposites. For a nanocomposite with 10 nm grain sizes, the peak ZT can be almost doubled and become comparable to conventional SiGe alloys. The main challenge here is to effectively prevent the nanograin growth during hot press and conserve the nano-features to scatter phonons [8].

4.6 Transient Phonon Monte Carlo Simulations

In addition to calculating the lattice thermal conductivities of various periodic structures, frequency-dependent MC Simulations can also be used to study transient phonon transport [23]. One particular application could be the data analysis of pump-probe measurements, in which an ultrafast laser "pump" pulse excites a sample and a probe pulse is used for probing the sample's response after an adjustable delay time t. In thermal conductivity measurements with this technique [53-55], the sample surface is first coated with a thin metal layer (typically Al). A sudden temperature rise is created by a pump pulse on the metallic film and the film temperature will decay with time due to heat diffusion into the underneath sample. After the delay time, the film temperature is measured by the probe pulse from its instantaneous reflectivity, which is a function of temperature. In a series of measurements, the delay time t is changed to obtain the complete temperature history of the sample. With known heat capacity of the sample, the film temperature variation can be fitted using metal-sample interfacial thermal resistance and out-of-plane thermal conductivity of the sample as fitting parameters in the model.

As the first step, our analysis can focus on the single-pulse response of a sample. At a time delay t after the pump pulse, heat penetrates a depth of $\sqrt{\alpha t}$ into the sample, with α as thermal diffusivity. Because the thermal diffusion equation fails on length scales comparable to the MFPs of the dominant energy carriers, data analysis becomes difficult for small t with $\sqrt{\alpha t}$ less than these phonon MFPs [56]. Combined with frequency-dependent MC simulations, more dependable data analysis can be carried out to explain sample temperature changes at all time steps.

In steady-state MC simulations, only acoustic branches are considered because optical phonons normally have group velocities close to zero and thus contribute little to thermal conductivities [25]. However, this is not the case for transient analysis. In traditional heat transfer, such transient thermal processes always involve thermal diffusivity $\alpha = k / C\rho$, in which C is specific heat, ρ is density, k is again thermal conductivity [57]. Although optical phonons have negligible influence on k, they account for a large percentage of C and is expected to strongly affect α. When we deal with phonon transport, optical phonons can store energy carried by acoustic phonons and thus contribute to subcell temperature changes. In the literature, the important role of optical phonons in transient processes is not always realized. In Ref. 23, only acoustic branches were considered for transient MC simulations and we should be cautious about errors caused by this simplification.

Figure 4.11 shows the transient MC simulation results for 1D pure silicon, with phonon-phonon scattering rates given by molecular dynamics simulations [31]. Heat spreads inside a chosen 500×50×50 nm^3 domain along the 500 nm direction, denoted as the x direction. The domain is divided into 500 subcells (1×50×50 nm^3 in dimension) along the x direction, corresponding to an x-direction spatial resolution as 1 nm. Adiabatic boundary conditions are assigned to all walls of the domain, i.e., specular reflection of all incident phonons. The initial temperature is assigned as $T=50\times\exp(-N/20)+300$ (in K) for the Nth subcell from the x=0 end (hot end). The temperature history at location x=0 is simulated with and without considering optical phonons. To simplify, here Einstein's model [25] is used for optical phonons, where they share the same energy at 0.06 eV and the relaxation time of optical-acoustic phonon scattering is fixed at 3 ps. Apparent difference can be observed between the two cases. Because

around 40% of the thermal energy is stored in stationary optical phonons, cooling down the hot end requires optical phonons to first transfer energy to acoustic phonons that can finally carry the energy to the cold end. As heat reservoirs [60,61], optical phonons significantly slow down the temperature changing process. The temperature profile evolution of the computational domain is plotted in Fig. 4.12, considering optical phonon contributions. Despite the fluctuations in calculated temperatures, we can clearly observe the decay process of hot-end temperatures as heat spreads across the whole computation domain.

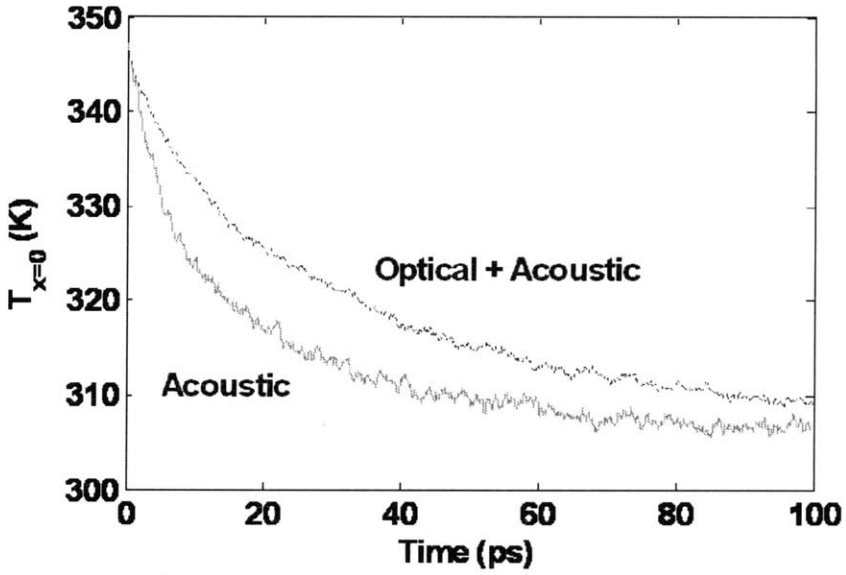

Figure 4.11 Simulated temperature decay at location x=0. With optical phonons, the temperature decays slower.

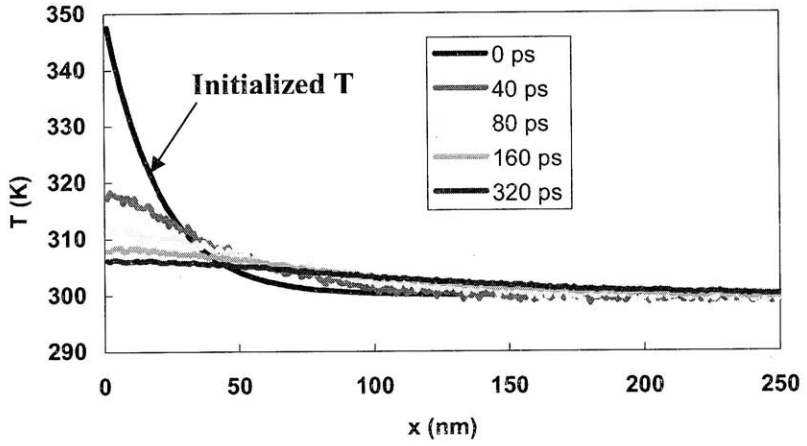

Figure 4.12 Temperature profile evolution of the simulation domain. Only the hot-end half is plotted here.

To match the real experimental data, we also need to include the Al film into simulations. In physics, major heat carriers in metals are electrons, while they become phonons in silicon. More efforts should be dedicated to better treatment of the electron-phonon energy exchange inside Al and the phonon transport across the Al-Si interface. In literature, a two-fluid model [58,59] was used to describe the energy transfer inside Al, in which the electron temperature T_e and phonon temperature T_p are coupled and solved together. Without simulating detailed electron transport, here T_e can be described by the Fourier law as

$$C_e \frac{dT_e}{dt} = k_e \frac{d^2 T_e}{dx^2} - G\left(T_e - T_p\right), \tag{4-29}$$

in which C_e is volumetric heat capacity of electrons, k_e is electronic thermal conductivity, G is the electron-phonon energy exchange rate per unit volume. With τ as the relaxation time of electron-phonon scattering, G is simply estimated by $G = C_e / \tau$. In MC simulations, T_p is the phonon pseudo temperature $\widetilde{T}$ of a subcell, determined by the numerical inversion of Eq. (4-5). On both the Al-Si interface (x=L) and the Al film surface (x=0), adiabatic boundary condition is enforced to T_e, i.e., $k_e \frac{dT_e}{dx}\Big|_{x=0,L} = 0$. At every time step, T_e is recalculated by solving Eq. (4-29) across the Al film thickness,

with updated local $\tilde{T}$ from the previous time step. Inside each Al subcell, phonons are then either deleted or created according to $\tilde{T}$ to compensate the energy exchange from electrons to phonons, $G\left(T_e - \tilde{T}\right)$. After processing electron-phonon energy exchange inside Al, the rest of the simulation scheme is the same as that Section 4.2. Within each time step, phonons in both Al and Si move with their individual group velocities and traveling directions. During the process, phonons may be diffusely transmitted or reflected by the Al-Si interface, or scattered by charge carriers, impurities, and other phonons inside each material region. Again specular reflection boundary condition is enforced to all boundaries of the computational domain.

As mentioned earlier, one challenge in MC simulations is how to accurately treat phonon reflection and transmission on the Al-Si interface. For Si-Si interfaces, in MC simulations phonons are assumed to only change their traveling directions after interface scattering. For an asymmetric Al-Si interface, however, such simplification is no longer valid. Because the highest allowed phonon frequency ($\omega_{\max}$) is smaller in Al, special attentions must be paid to the transmission of Si phonons with frequencies higher than $\omega_{\max,Al}$. Although these high-frequency silicon phonons contribute little to energy transport at low temperatures, they are expected to be important at high temperatures and their transmission should be correctly treated for accurate simulations. In addition, a more accurate MC simulation should utilize a frequency-dependent phonon transmissivity on the Al-Si interface. In principle, this can be obtained by molecular dynamics simulations but only a few calculations were performed on other interfaces in the past. Some future efforts may be dedicated to this aspect.

4.7 Summary

In this chapter, frequency-dependent MC simulations are carried out to study the phonon transport inside 2D periodic porous silicon and 3D silicon nanocomposites. A new boundary condition consisting of periodic heat flux with a constant virtual wall temperature is developed for arbitrary periodic structures, enabling accurate thermal

conductivity prediction with a single period as the computational domain. This work sets up a framework for future studies of phonon transport inside periodic structures.

For lightly doped silicon, MC simulations show that a large thermal conductivity reduction can be observed even in micro-porous structures, an effect that is not expected if an average phonon MFP is used. This indicates that phonon size effects in lightly doped nanostructured bulk silicon can be significantly underestimated if frequency-dependent phonon MFPs are not included into the model.

For heavily doped silicon nanocomposites, we find that grain sizes on the order of 10 nm are required to observe strong phonon size effects. The lattice thermal conductivity can be dropped to around 3.0 W/m·K for 10 nm grain sizes. With 10 nm grain sizes and heavy doping, the lattice thermal conductivity can be dropped to around 3.0 W/m·K, which is a factor of 50 reduction from pure single-crystal silicon. Although traditionally silicon is not considered for TE applications, our studies show that a ZT above 1.0 is achievable in bulk silicon via the nanocomposite approach. Compared with SiGe alloys, silicon nanocomposites eliminate the usage of expensive germanium, which makes it more attractive for commercialization.

With more accurate information on phonon MFPs in other materials, frequency-dependent MC simulations of phonon transport can also be conducted for their TE nanocomposites to provide useful guidance for material synthesis. Along this line, one interesting topic is the lattice thermal conductivities of PbTe and PbSe nanocomposites, which we intensively investigated during 2005-2007. For micro-meter grain sizes, PbTe nanocomposites showed a 25% lattice thermal conductivity reduction from the bulk value, whereas the lattice thermal conductivity of PbSe nanocomposites was already close to the bulk value. This cannot be explained based on the similar averaged phonon MFPs (both around 20 nm at 300 K) for both materials. On the other hand, frequency-dependent analysis at 300 K shows that 50% of the lattice thermal conductivity of PbTe is contributed by phonons with MFP less than 40 nm [30], while 50% of the lattice thermal conductivity of PbSe is carried by phonons with MFP less than 20 nm. According to this, theoretically we expect much stronger phonon size effects in PbTe nanocomposites. The comparison between my frequency-dependent MC simulations and measurement data may finally clarify our puzzles.

4.8 References

[1] A. Minnich, M. S. Dresselhaus, Z. F. Ren, and G. Chen, *Energy Environ. Sci.* **2**, 466 (2009).

[2] B. Poudel, Q. Hao, Y. Ma, Y. C. Lan, A. Minnich, B. Yu, X. Yan, D. Z. Wang, A. Muto, D. Vashaee, X. Y. Chen, J. M. Liu, M. S. Dresselhaus, G. Chen, and Z. F. Ren, *Science* **320**, 634 (2008).

[3] Y. Ma, Q. Hao, B. Poudel, Y. C. Lan, B. Yu, D. Z. Wang, G. Chen, and Z. F. Ren, *Nano Lett.* **8**, 2580 (2008).

[4] J. Yang, Q. Hao, H. Wang, Y. C. Lan, Q. Y. He, A. Minnich, D. Z. Wang, J. A. Harriman, V. M. Varki, M. S. Dresselhaus, G. Chen, and Z. F. Ren, *Phys. Rev. B* **80**, 115329 (2009).

[5] G. H. Zhu, H. Lee, Y.C. Lan, X.W. Wang, G. Joshi, D.Z. Wang, J. Yang, D. Vashaee, H. Guilbert, A. Pillitteri, M.S. Dresselhaus, G. Chen, and Z.F. Ren, *Phys. Rev. Lett.* **102**, 196803 (2009).

[6] G. Joshi, H. Lee, Y. C. Lan, X. W. Wang, G. H. Zhu, D. Z. Wang, R. W. Gould, D. C. Cuff, M. Y. Tang, M. S. Dresselhaus, G. Chen, and Z. F. Ren, *Nano Lett.* **8**, 4670 (2008).

[7] X. W. Wang, H. Lee, Y. C. Lan, G. H. Zhu, G. Joshi, D. Z. Wang, J. Yang, A. J. Muto, M. Y. Tang, J. Klatsky, S. Song, M. S. Dresselhaus, G. Chen, and Z. F. Ren, *Appl. Phys. Lett.* **93**, 193121 (2008).

[8] S. K. Bux, R. G. Blair, P. K. Gogna, H. Lee, G. Chen, M. S. Dresselhaus, R. B. Kaner, and J. P. Fleurial, *Adv. Fun. Mater.* **19**, 2445 (2009).

[9] R. G. Yang, G. Chen, *Phys. Rev. B* **69**, 195316 (2004).

[10] R. G. Yang, G. Chen, and M. S. Dresselhaus, *Phys. Rev. B* **72**, 125418 (2005).

[11] R. Prasher, *J. Appl. Phys.* **100**, 034307 (2006).

[12] K. Miyazaki, T. Arashi, D. Makino, and H. Tsukamoto, *IEEE Trans. Comp. Pack. Tech.* **29**, 247 (2006).

[13] A. Pattamattaa and C. K. Madnia, *Int. J. Heat Mass Transfer* **52**, 860 (2009).

[14] J.-D. Chung and M. Kaviany, *Int. J. Heat Mass Transfer* **43**, 521 (2000).

[15] W. X. Tian and R. G. Yang, *J. Appl. Phys.* **101**, 054320 (2007).

[16] M. S. Jeng, R. G. Yang, D. Song, and G. Chen, *ASME J. Heat Transfer* **130**, 042410 (1-11) (2008).

[17] D. Song, G. Chen, *Appl. Phys. Lett.* **84**, 687 (2004).

[18] Q. Hao, G. Chen, M. S. Jeng, *J. Appl. Phys.* **106**, 114321 (2009).

[19] S. Mazumder, A. Majumdar, *ASME J. Heat Transfer* **123**, 749 (2001).

[20] Y. F. Chen, D. Y. Li, J. R. Lukes, A. Majumdar, *ASME J. Heat Transfer* **127**, 1129 (2005).

[21] D. Lacroix, K. Joulain, D. Terris, D. Lemonnier, *Appl. Phys. Lett.* **89**, 103104 (2006).

[22] J. Randrianalisoa and D. Baillis, *ASME J. Heat Transfer* **130**, 072404 (2008).

[23] D. Lacroix, K. Joulain, and D. Lemonnier, *Phys. Rev. B* **72**, 064305 (2005).

[24] Q. Hao, G. H. Zhu, X. W. Wang, A. Minnich, Z. F. Ren, G. Chen, submitted.

[25] G. Chen, *Nanoscale Energy Transport and Conversion: A Parallel Treatment of Electrons, Molecules, Phonons, and Photons* (Oxford University Press, New York, 2005).
[26] L. Lindsay and D. A. Broido, *J. Phys.: Condens. Matter* **20**, 165209 (2008).
[27] K. E. Goodson, Chapter 7 in *Microscale Energy Transport*, edited by by C. L. Tien, A. Majumdar, and F. M. Gerner (Taylor & Francis, Washington, DC , 1997).
[28] J. Callaway, *Phys. Rev.* **113**, 1046 (1959).
[29] M. G. Holland, *Phys. Rev.* **132**, 2461 (1963).
[30] C. Dames and G. Chen, Chapter 42 in *Thermoelectrics Handbook: Macro to Nano*, edited by D. M. Rowe (CRC Press, Boca Raton, FL, 2005).
[31] A. Henry and G. Chen, *J. Comput. Theor. Nanosci.* **5**, 141 (2008).
[32] P. G. Klemens, *Proc. Phys. Soc. London* **68**, 1113 (1955).
[33] M. Asheghi, K. Kurabayashi, R. Kasnavi, K. E. Goodson, *J. Appl. Phys.* **91**, 5079 (2002).
[34] J. M. Ziman, *Philos. Mag.* **1**, 191 (1956).
[35] J. M. Ziman, *Philos. Mag.* **2**. 292 (1957).
[36] E. O. Kane, *J. Phys. Chem. Solids* **1**, 249 (1957).
[37] J. Kołodziejczak, *Acta Phys. Pol.* **20**, 289 (1961).
[38] M. N. Alexander and D. F. Hocomb, *Rev. Mod. Phys.* **40**, 815 (1968).
[39] C. Yamanouchi, K. Mizuguchi, and W. Sasaki, *J. Phys. Soc. Jpn.* **22**, 859 (1967).
[40] J.-D. Chung and M. Kaviany, *Int. J. Heat Mass Transfer* **43**, 521 (2000).
[41] J.-H. Lee, J. C. Grossman, J. Reed, and G. Galli, *Appl. Phys. Lett.* **91**, 223110 (2007).
[42] G. Gesele, J. Linsmeier, V. Drach, J. Fricke, and R. Arens-Fischer. *J. Phys. D* **30**, 2911 (1997).
[43] A. Yamamoto, H. Takazawa, T. Ohta, *Proc. Int. Conf. Thermoelectr.* 428 (1999).
[44] A. Eucken, *Forsch. Ceram. Abstr.* **11**, 576 (1932); **12**, 231 (1933).
[45] C. Dames and G. Chen, *J. Appl. Phys.* **95**, 682 (2004).
[46] G. Chen, *Phys. Rev. B* **57**, 14958 (1998).
[47] T. F. Zeng, G. Chen, *ASME J. Heat Transfer* **123**, 340 (2001).
[48] A. Maiti, G. D. Mahan, and S. T. Pantelides, *Solid State Commun.* **102**, 517 (1997).
[49] V.I. Fistul', *Heavily Doped Semiconductors* (Plenum, New York, 1969).
[50] M. Lundstrom, *Fundamentals of Carrier Transport* (Oxford University Press, Cambridge, UK, 2000).
[51] S. Uma, A. D. McConnell, M. Asheghi, K. Kurabayashi, and K. E. Goodson, *Int. J. Thermophys.* **22**, 605 (2001).
[52] A. Minnich, H. Lee, X. W. Wang, G. Joshi, M. S. Dresselhaus, Z. F. Ren, G. Chen, and D. Vashaee, *Phys. Rev. B* **80**, 155327 (2009).
[53] W. S. Capinski and H. J. Maris, *Physica B* **219-220**, 699 (1996).
[54] J. Morath, H. J. Maris, J. J. Cuomo, D. L. Pappas, A. Grill, V. V. Patel, J. P. Doyle, and K. L. Saenger, *J. Appl. Phys.* **76**, 2636 (1994).
[55] W. S. Capinski, H. J. Maris, E. Bauser, I. Silier, M. Asen-Palmer, T. Ruf, M. Cardona, and E. Gmelin, *Appl. Phys. Lett.* **71**, 2109 (1997).
[56] D. G. Cahill, W. K. Ford, K. E. Goodson, G. D. Mahan, A. Majumdar, H. J. Maris, R. Merlin,and S. R. Phillpot, *J. Appl. Phys.* **93**, 793 (2003).

[57] A. F. Mills, *Heat Transfer* (Prentice Hall, Upper Saddle River, NJ, 1999).
[58] A. Majumdar and P. Reddy, *Appl. Phys. Lett.* **84**, 4768 (2004).
[59] Ronggui Yang, *Nanoscale Heat Conduction with Applications in Nanoelectronics and Thermoelectrics*, Ph.D. thesis, Massachusetts Institute of Technology, December 2005. Department of Mechanical Engineering.
[60] S. V. J. Narumanchi, J. Y. Murthy, C. H. Amon, *Heat Mass Transfer* **42**, 478 (2006).
[61] P. Heino, *Comput. & Math. with Applications* **59**, 2351 (2010).

Chapter 5. Measurements on Grain Interface Barrier Height and Nanopowder Bandgap

In this chapter, two novel techniques are introduced for the fundamental studies of thermoelectric (TE) nanocomposites. As an important parameter for electron modeling, the grain-interface barrier height was extracted from the impedance measurement of a PbTe nanocomposite. In the thermoelectrics field, this is the first experimental attempt to understand the influence of grain interfaces on charge carrier transport. This method can be potentially extended to other nanocomposites as a general tool for grain interface studies. Secondly, a simple bandgap measurement technique with nanopowders was developed based on Fourier Transform Infrared Spectroscopy (FTIR). This provides a convenient way to quickly check the bandgaps of various TE nanocomposites, which is critical for theoretical analysis.

5.1 Interface Studies of Nanograin Boundaries using Novel Capacitance Technique

Experimental results of BiSbTe nanocomposites suggest that the bipolar conduction observed at elevated temperatures (refer to Chap. 2) can be suppressed in nanocomposites. This benefits the high-temperature thermoelectric performance of these nanocomposites in addition to the lattice thermal conductivity reduction caused by grain-interface phonon scattering. Theoretically, this fact can be explained by assuming the existence of an interfacial barrier that scatters more minority charge carriers than majority charge carriers [1]. As a fitting parameter, this interface barrier height can be obtained from the theoretical analysis of temperature-dependent material properties. On the other hand, the suppressed bipolar conduction may also be attributed to the increased majority carrier concentration in BiSbTe nanocomposites, which ranges from 2.5×10^{19} to 2.9×10^{19} cm^{-3} in comparison with 1.8×10^{19} cm^{-3} for state-of-art ingots (3D bulk materials). In this case, weaker bipolar conduction is anticipated because more thermally excited minority carriers are required for bipolar conduction to take place in nanocomposites. Experimentally, the first hypothesis can be verified by measuring the grain interface

barrier height and comparing it with modeling predictions. In this section, impedance measurements on a PbTe nanocomposite are performed to extract its grain interface barrier height. More advanced measurements on a single grain interface are further discussed in Chap. 6. In the future, similar work can be carried out on BiSbTe nanocomposites to find out in more detail the cause of suppressed bipolar conduction, which is important for ZT enhancements at elevated temperatures.

5.1.1 Concept of Interface Capacitance Measurement

In electron modeling, the influence of a grain interface is viewed as a potential barrier to scatter charge carriers (Fig. 5.1) [2,3]. This potential barrier is formed as a result of charge trapping by states on grain interfaces [3]. Such interface states can be created by dangling bonds or other interfacial defects. They may also result from impurity atoms trapped on the interface, which act as either donor or acceptor levels in this case. The interface charge trapping leads to a depletion region with a width w, and an associated static capacitance given by [3]

$$C_0 = \varepsilon_r \varepsilon_0 / w, \tag{5-1}$$

where ε_r , ε_0 are the dielectric constant and vacuum permittivity, respectively. Experimentally, the static capacitance C_0 can be extracted from ac impedance measurements [4-8]. The trapped charges per unit interface area, Q, and the potential barrier height, Φ_B, can be calculated by [9]

$$Q = \frac{\varepsilon_r \varepsilon_0 N_d}{C_0}, \tag{5-2}$$

$$\Phi_B = \frac{N_d e^2 w^2}{8\varepsilon_r \varepsilon_0} = \frac{\varepsilon_r \varepsilon_0 N_d e^2}{8C_0^2}, \tag{5-3}$$

where N_d is the doping level, e is the charge per electron. For $Bi_xSb_{2-x}Te_3$ nanocomposites ($x \approx 0.5$), an effective ε_r is estimated to be 97 by averaging ε_r values first among different crystal orientations in Bi_2Te_3 and Sb_2Te_3, and then between these two compositions (refer to Chap. 3). In addition, our TE property analysis [1] suggested $\Phi_B \sim 0.1$ eV in these nanocomposites, indicating $w \sim 13$ nm according to Eq. (5-3). It can

be justified that grain sizes (at least 20-30 nm) are typically larger than w in this case. Otherwise, the whole grain is depleted and w is limited to the grain size in Eqs. (5-2) and (5-3). For $CoSb_3$-based or PbTe nanocomposites, the obtained grain sizes are much larger (200 nm-1 μm) and this assumption is always valid.

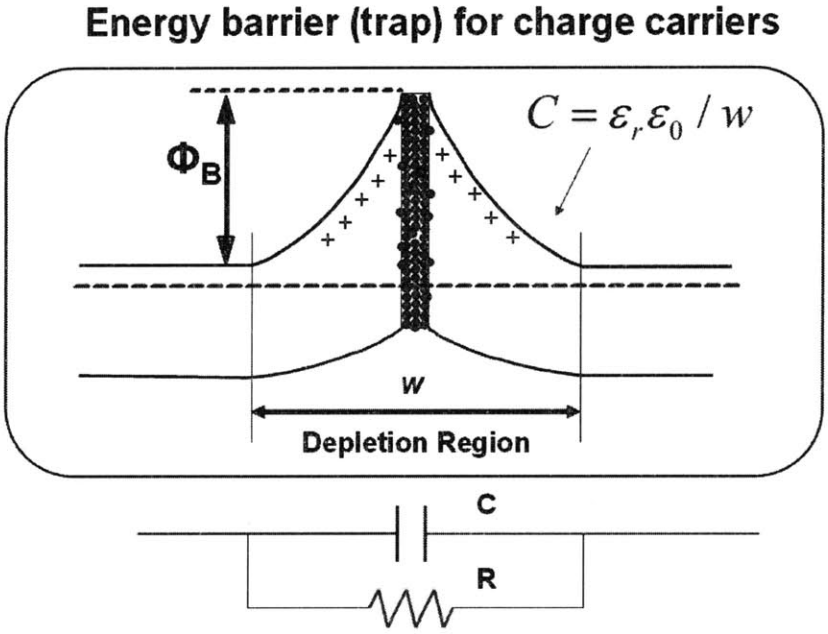

Figure 5.1 Energy-band diagram and charge distribution at a grain boundary. This figure presents an n-type sample with a barrier for electrons (majority carriers) and a trap for holes (minority carriers) on its grain interface. A capacitance is associated with the depletion region formed by charge trapping on grain interfaces. The boundary is modeled as a symmetric Schottky barrier, whose equivalent circuit consists of a resistor in parallel connected with a capacitor, as shown below the upper figure.

To study charge carrier transport across grain interfaces, ac impedance measurements were conducted on polycrystals of silicon and various oxides (e.g. ZnO) [4-8]. In a general test, the applied bias across a grain interface consists of an ac part and an additional dc part. In the steady state, the capacitance was measured as a function of temperature, ac frequency, and the additional dc bias. In transient measurements, the dc bias was suddenly zeroed and the recovery history of the non-equilibrium capacitance was recorded, from which the interfacial state spectrum can be derived [10-12]. In this thesis, ac impedance measurements and the corresponding data analysis are demonstrated in a PbTe nanocomposite. As the starting point, all ac measurements are focused on the

steady state without an additional dc bias. In the thermoelectrics field, this is the first attempt to understand the interface properties of TE nanocomposites and these results are expected to have an impact on research topics related to "interface engineering".

5.1.2 Interface Admittance Model

Under an ac bias, the small-signal ac current across a grain interface consists of two parts: one part is the current flowing over the barrier Φ_B and the other part is a displacement current due to the time dependence of the screening charge in the depletion region. The over-the-barrier part here also includes the contribution from charge trapping and emission at the interface. For a symmetric depletion region shown in Fig. 5.1, theoretically it can be shown that the Φ_B variation is completely in phase with the applied ac voltage [13]. In this situation, taking all current components into account yields an effective interface admittance of $g_0 + i\omega C_0$ at all frequencies [13,14], where g_0 is the zero-bias dc conductance, and ω is the ac angular frequency. Instead of constant g_0 and C_0, previous measurements on both polycrystalline ZnO and Si suggested a frequency-dependent interface conductance $G^*(\omega)$ and capacitance $C^*(\omega)$, where the frequency dependence of $C^*(\omega)$ was normally much stronger than that for $G^*(\omega)$ [3]. These experimental observations were attributed to the out-of-phase Φ_B variation under an applied ac bias [3], caused by deep trap effects [13].

Figure 5.2B shows the carrier distribution in a depletion region with a single deep trap level, which provides extra charges in addition to the dominant impurity concentration N_d (shallow defects). In this situation, the grain-interface conductance G^* and capacitance C^* are given as [13]

$$G^*(\omega) = g_0 + C_0\omega^2 \frac{n_1\hat{\tau}_1}{1+(\omega\hat{\tau}_1)^2}, \tag{5-4}$$

$$C^*(\omega) = C_0\left[1+\frac{n_1}{1+(\omega\hat{\tau}_1)^2}\right], \tag{5-5}$$

in which $\hat{\tau}_1$ is the relaxation time of grain interface emissions, and a factor n_1 which is used to weigh the importance of the deep trap level, are expressed as

$$\hat{\tau}_1 = \frac{e}{A^* T^2 c_1} \frac{e^{-E_f/k_B T}}{1+\frac{1}{2}e^{(E_T-E_f)/k_B T}} \frac{1}{1+(N_1/N_d)(X_1/X_0)}, \tag{5-6}$$

$$n_1 = \frac{N_1}{N_d} \frac{1-X_1/X_0}{1+(N_1/N_d)(X_1/X_0)}, \tag{5-7}$$

where the deep level energy E_T and the Fermi level E_f both refer to the band edge, A^* is the Richardson constant, c_1 is the capture cross section for interface trap emission, X_1 (X_0) is the half depletion region width for deep-level (shallow) defects, N_1 (N_d) is the charge concentration for deep-level (shallow) defects (see Fig. 5.2B). Without deep trap levels (n_1=0), $C^*(\omega)$ and $G^*(\omega)$ simply degrade to C_0 and g_0, respectively.

Consistent with experimental observations, Eq. (5-5) indicates that $C^*(\omega)$ monotonically decreases with increased ω. In physics, the characteristic emission rate of interface traps ($1/\hat{\tau}_1$) imposes a limit on the rate at which charge transfer can occur between the boundary and the grains. At high frequencies, charge carrier transfer into and out of grain-boundary traps becomes impossible so that the capacitance $C^*(\omega)$ is expected to approach the static value C_0 [3]. Correspondingly, the high-frequency limits of Eqs. (5-4) and (5-5) suggest $G^*(\infty)=g_0+C_0 n_1/\hat{\tau}_1$ and $C^*(\infty)=C_0$. The frequency for $C^*(\omega)$ saturation is normally found experimentally because $\hat{\tau}_1$ is rarely available for studied grain interfaces.

When the charge distribution in Fig. 5.2 is known, the steady-state barrier height Φ_B can be determined by solving the Poisson equation, given as

$$\Phi_B = \frac{e^2}{2\varepsilon_r \varepsilon_0}\left(N_d X_0^2 + N_1 X_1^2\right), \tag{5-8}$$

which is simply the superposition of Φ_B for the shallow defects and the deep-trap level. Based on the thermionic emission theory, g_0 in Eq. (5-4) can be computed by [15,16]

$$g_0 = \frac{A^* eT}{k_B} e^{-(\Phi_B - E_f)/k_B T} . \tag{5-9}$$

The Richardson constant is calculated by [16]

$$A^* = \frac{4\pi e k_B{}^2 m_0}{h^3} \sqrt{\frac{\left(m_d^* / m_0\right)^3}{m_\chi^* / m_0}} , \tag{5-10}$$

in which m_d^* is the density of states effective mass, m_χ^* is the conductivity effective mass of charge carriers.

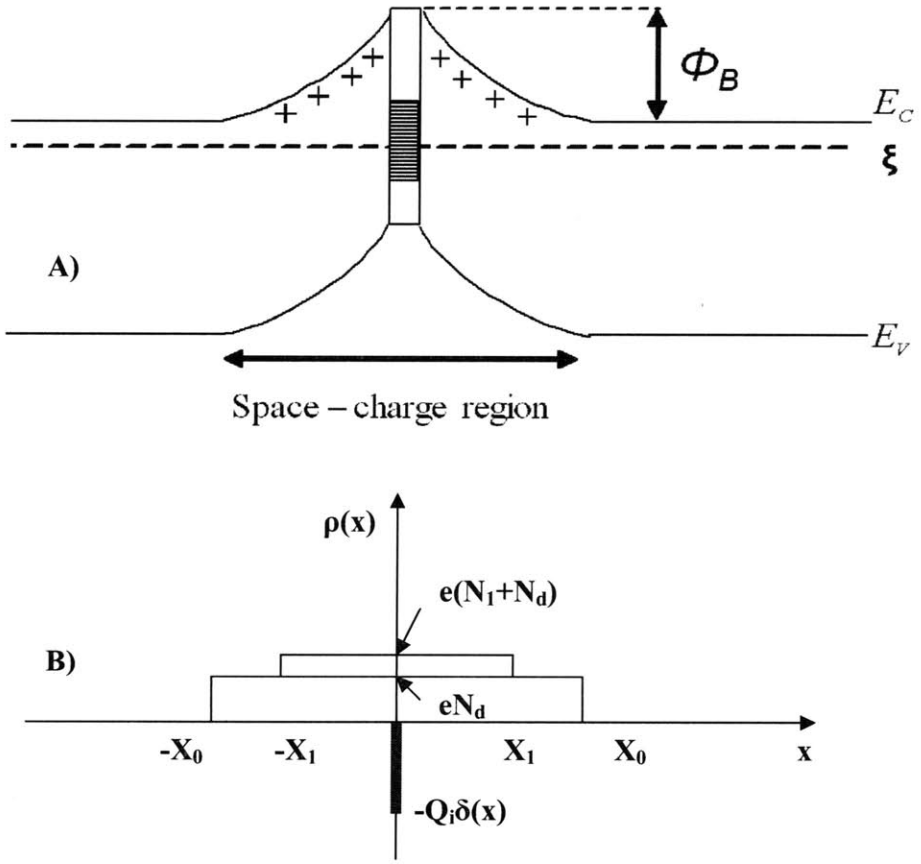

Figure 5.2 (A) Energy-band diagram and (B) charge distribution on a grain interface. One deep bulk trap level is included in addition to shallow defects.

5.1.3 Measurements on Bulk Samples

Because the grain-interface capacitance and conductance can be frequency-dependent with deep trap levels, it is always necessary to conduct ac impedance measurements at high frequencies where $C^*(\omega)$ and $G^*(\omega)$ are saturated. The challenge of such measurements lies in the fact that a typical TE nanocomposite has an electrical conductivity three orders of magnitude higher than that of silicon or oxide polycrystals investigated in the past. When the ac frequency is increased to approach C_0, the self inductance of a sample, L_S, was found to dominate the imaginary part of measured impedance Z, and thus overshadow the interface capacitance contribution. In this situation, $\mathrm{Im}(Z)$ may even become positive instead of an anticipated negative value (Fig. 5.3A).

In principle, the self inductance of a conductor is caused by its surrounding electromagnetic (EM) field and can be eliminated by shielding. With a gap between a conductor and the shield, the self-inductance of a coaxial shielded sample is estimated by [17]

$$L_S = \frac{\mu_0}{2\pi} \ln \frac{D}{d} \quad H/m, \tag{5-11}$$

in which μ_0 is vacuum permeability, D and d represent the cross-section dimensions of the shield and the sample, respectively. Apparently we need to have D close to d to eliminate L_S. At the beginning, a primitive shielding with thin copper pieces was used to produce the result in Fig. 5.3A. The shielding setup was improved later, as shown in the inset of Fig. 5.3A. The sample was held tightly by four copper plates around it, all of which were sprayed with boron nitride to avoid shorting the sample. On the top copper plate, two holes were drilled and voltage-probe wires were spark welded onto the sample through the holes. Currents were injected from both ends of the sample, indicated by the arrows.

Different from typical high-frequency ac shielding with Al foils, in these measurements thick copper plates are required to effectively shield the low-frequency EM field around the sample. For EM waves propagating into a shielding material, their energy decays exponentially by a length scale called the skin depth [17]

$$\delta = \sqrt{\frac{1}{\pi\sigma\mu f}}, \tag{5-12}$$

where σ is again the electrical conductivity, f is the ac frequency, μ is the permeability of the shielding material. For f at 100 kHz, the skin depth is 0.2 mm even in a good conductor like copper, and the skin depth becomes larger as f is reduced. To effectively shield the EM waves, both the top and bottom copper plates in the Fig. 5.3A inset were 6 mm in thickness.

The measurements were carried out on a p-type PbTe nanocomposite sample, which was intentionally chosen for its low electrical conductivity (2016 S/m at 300 K). The ratio between Re(Z) and Im(Z) is plotted in Fig. 5.3B. With the improved shielding, the measured impedance Z shows a reliable trend up to 95 kHz, where the influence of L_s starts to be observed in $\mathrm{Im}(Z)$. In the 95-100 kHz frequency range, the sample self conductance in the improved shielding setup is estimated by $L_s = \Delta\left|\mathrm{Im}(Z)\right| / \Delta\omega$=16 nH, which is a reasonably small value for a well shielded conductor. The improved shielding with copper plates gives much more reasonable results compared with primitive shielding using thin copper pieces. In the latter case, the measured impedance was also not repeatable among different mountings.

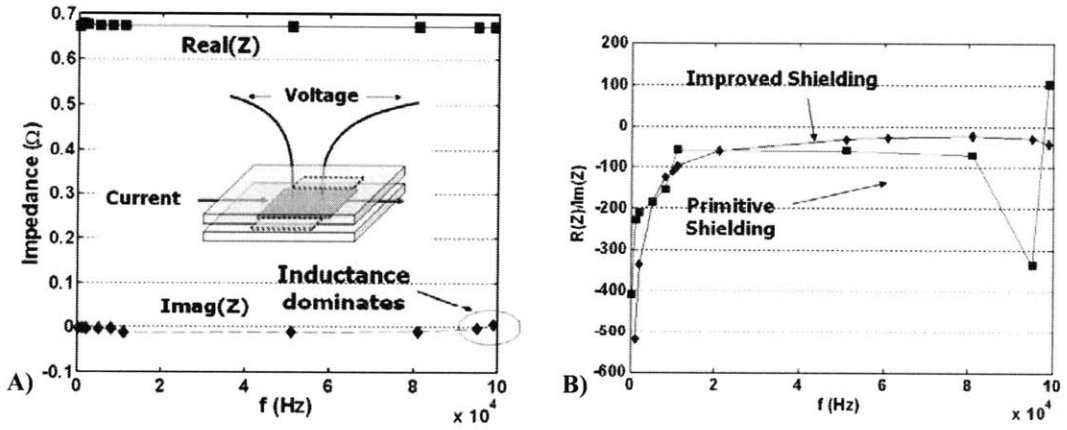

Figure 5.3 A) Real and imaginary parts of the measured impedance Z with a primitive shielding provided by thin copper pieces. The improved experimental setup is drawn in the inset. B) The ratio between the real and imaginary parts of Z. Results from different shielding setups are compared.

5.1.4 Data Analysis with the Brick Layer Model

The measured PbTe sample is a 3D network of grains joined with their interfaces. The brick layer model [18] is employed to analyze the results, where the nanocomposite structure is approximated by packed identical cubes and the measured impedance Z is thus proportional to that for a single grain. The equivalent circuit of a single grain is shown in Fig. 5.4. Because the PbTe grain sizes ~ 1 μm are typically much larger than the depletion region width w, the conduction along grain-boundary sidewalls is not considered here.

Without considering the exact number of grains inside a measured sample, the ratio of $\mathrm{Im}(Z)$ and $\mathrm{Re}(Z)$ is directly compared with the prediction for a single grain in the brick layer model (Fig. 5.4). This ratio is given by

$$|\mathrm{Im}(Z)/\mathrm{Re}(Z)| = \left[\frac{\omega C^*}{G^{*2}+(\omega C^*)^2}\right] \Big/ \left[\frac{G^*}{G^{*2}+(\omega C^*)^2} + R_{GI}A\right]. \tag{5-13}$$

Because $G^*(\omega)$ and $C^*(\omega)$ are evaluated per unit area, here the in-grain resistance R_{GI} is multiplied by the grain cross-section area A for consistency. For this PbTe sample, it was annealed after the first measurement and its thermal conductivity was increased from 0.75 to 1.6 W/m·K, with grain sizes grown up to around 1 μm. We can estimate the R_{GI} value based on the electrical conductivity σ. With L_1 as the sample length, $L_2 \times L_3$ as the sample cross sectional area, and the grain size d=1 μm, then the resistance of this sample is simply

$$R_{sample} = \frac{R_{GI}(L_1/d)}{(L_2/d)(L_3/d)} = \frac{L_1}{L_2 L_3 \sigma}, \tag{5-14}$$

which gives $R_{GI}\ A = R_{GI}d^2 = d/\sigma = 5\times10^{-10}\ \Omega\cdot\mathrm{m}^2$. All parameters used for the p-type PbTe nanocomposite are listed in Table 5.1, and the fitting results are presented in Table 5.2 and Fig. 5.5. Here C_0, $\hat{\tau}_1$, n_1, used in Eqs. (5-4) and (5-5), are treated as fitting parameters. Because the grain interface charges from the deep trap level ($\sim N_1X_1$) are generally much smaller than that from the shallow defects ($\sim N_dX_0$), we can simply neglect the influence of the deep trap level on Φ_B ($\sim N_iX_i^2$) so that the interface

conductance g_0 is determined by C_0 based on Eqs. (5-3) and (5-9). The obtained Φ_B is comparable in magnitude to the bandgap E_g ~0.31 eV at 300 K [19]. More accurate analysis may further consider the dielectric constant variation on grain interfaces [21]. In this case, the dielectric constant can be treated as another fitting parameter. According to the fitted n_1 and $\hat{\tau}_1$ values, $C^*(\omega)$ is reduced by a factor of 4.2 from low to high frequencies and its saturation will take place above 1 MHz·rad. For heavily doped nanocomposites, we may not suffer from the deep trap levels and the need to measure at high frequencies for $C^*(\omega)$ saturation could be eliminated.

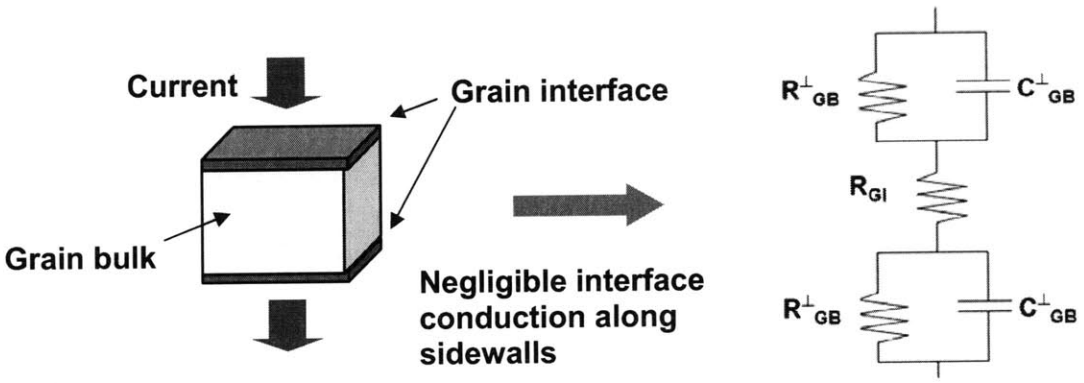

Figure 5.4 Equivalent circuit of a grain in the brick layer model [18]. Here R_{GI}, $R_{GB}{}^{\perp}$, $C_{GB}{}^{\perp}$ are in-grain resistance, grain-interface resistance, and grain-interface capacitance, respectively. Only half of the top and bottom grain boundaries are included in a grain.

Table 5.1 Parameters used for p-type PbTe. Both m_d^* and m_χ^* are given in Ref. 19, with m_0 as the free electron mass. The Fermi level E_f, referred to the valence band edge E_v, is calculated with a single band model based on the hole concentration p and the density of states effective mass m_d^*. The Richardson constant A^* is calculated by Eq. (5-9).

p (cm^{-3})	$\xi - E_v$ (meV)	m_d^* (in m_0)	m_χ^* (in m_0)	A^*	ε_r [20]
2.5×10^{17}	53	0.187	0.05	4.33×10^5	400

Table 5.2 Parameters determined by the theoretical fitting in Fig. 5.5.

R_{GI} A ($\Omega \cdot m^2$)	C_0 (F/m^2)	$\hat{\tau}_1$ (s)	n_1	g_0 (S/m^2)	Φ_B (eV)
5.0×10^{-10}	7×10^{-3}	2.2×10^{-6}	3.2	1.91×10^{5}	0.359

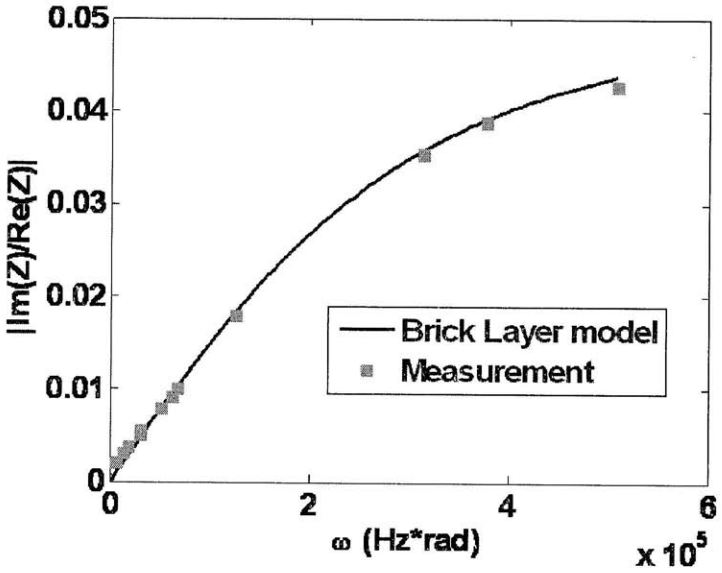

Figure 5.5 Fitting the ratio between the imaginary and real parts of the measured impedance Z.

5.2 Nanopowder Bandgap Measurement

As pointed out in Chap. 1, one challenge in thermoelectrics research is to find out the bandgaps of nanocomposites with various compositions. For electron modeling, the exact bandgap value is critical for the occurrence of bipolar conductions at elevated temperatures [22]. However, it is always challenging to obtain accurate bandgap values via either computations or experiments, especially for narrow-bandgap materials used for TE applications. For example, the bandgap of pure $CoSb_3$ was reported to be from 0.031 to 0.7 eV by either calculations or measurements [23-37], which introduces big uncertainties to theoretical analysis. Typically, the bandgap of a material can be extracted from its light absorption pattern given by transmission measurements, or reflectance measurements using the Kramer-Krönig relation [38]. Transmission

measurements are mostly conducted on ~100 nm thick films, prepared by various deposition techniques or epitaxial growth on a substrate that is transparent to infrared (IR) light [39-42]. For nanocomposites, however, it is difficult to prepare thin films by grinding them down to a uniform thickness on the order of 100 nm. On the other hand, it is easy to prepare nanopowders by ball milling, which is also an essential step in making nanocomposites. As a convenient method for nanocomposite bandgap measurements, transmission measurements on nanopowders with Fourier Transform Infrared Spectroscopy (FTIR) are pursued here. The challenge lies in that the measured transmission is affected not only by nanoparticle absorption, but also by nanoparticle scattering and substrate absorption. Generally speaking, the absorption of a nanoparticle is proportional to its volume V, whereas its scattering strength is proportional to V^2 [43]. For very small particles ($V \rightarrow 0$), it is anticipated that the particle absorption becomes more important compared with scattering effects. In principle, it is possible for us to observe the absorption pattern even with light scattering of particles in the background. For a PbTe nanopowder sample, a reasonable absorption pattern can be extracted, and the bandgap estimated from this pattern is close to the literature value. In the near future, similar tests can also be carried out on $CoSb_3$ nanopowder samples and in this way clarify puzzles about its bandgap.

For transmission measurements, a single-crystal KBr slice around 0.5-1 mm thick is chosen as the substrate because of its high transmissivity in the photon energy range of interest (0.2-0.5 eV). Figure 5.6 presents the energy-dependent transmissivity of a typical KBr slice, in comparison to that for a disc cold pressed from KBr powders. Due to the defects inside a cold pressed disc, its transmissivity significantly declines for energies greater than 0.1 eV, which makes it unsuitable for bandgap measurements. In the literature, bandgap measurements on powders were performed on discs cold pressed from a mixture of the tested powder and KBr powder [44-46]. However, in practice it is challenging to prepare high-quality discs simply by a cold press process, and here the low transmissivity above 0.2 eV will introduce large uncertainties to our measurements. For systematic studies, a comparison between different measurements also becomes difficult due to the limited repeatability of the cold press technique. Keeping these in mind, using a single-crystal substrate for the transmission measurements is more practical.

In all tests, a nanopowder was first dispersed in isopropyl alcohol. A droplet of this solution was sprayed onto a KBr slice so that nanoparticles were sparsely distributed on the slice after the evaporation of the alcohol. Figure 5.7A presents the original transmission of a KBr slice and that after loading Si or PbTe nanopowders onto this slice. Both nanopowders were prepared from ball milling undoped commercial ingots. The particle sizes were typically around 50 nm. Compared with the slice used in Fig. 5.6, the transmission of this KBr slice was reduced at high energies possibly due to its rougher surface. The KBr transmissivity with PbTe nanoparticles was consistently lower than that with Si nanoparticles because more nanoparticles were loaded for the former case.

To check the influence of adding nanoparticles on the KBr transmission, the ratio between the KBr transmissivity with/without nanoparticles is computed (Fig. 5.7B). Above 0.1 eV, the transmission ratio for the Si nanoparticle case becomes independent of the photon energy up to 0.8 eV. Below 0.1 eV, this ratio decreases with increased photon energy mainly due to the significant scattering increase of nanoparticles. For particle sizes much less than the light wavelength λ, the scattering is proportional to λ^{-4} (Rayleigh scattering [43]) and varies significantly in this energy regime. Although phonons in Si absorb photon energies below 0.2 eV (Fig. 5.8) [47,48], this weak effect cannot be clearly observed from these measurements. In contrast, the light absorption by PbTe nanoparticles above their bandgaps would further reduce the KBr transmissivity in addition to the transmissivity reduction caused by nanoparticle scattering, marked by the straight line in Fig. 5.7B.

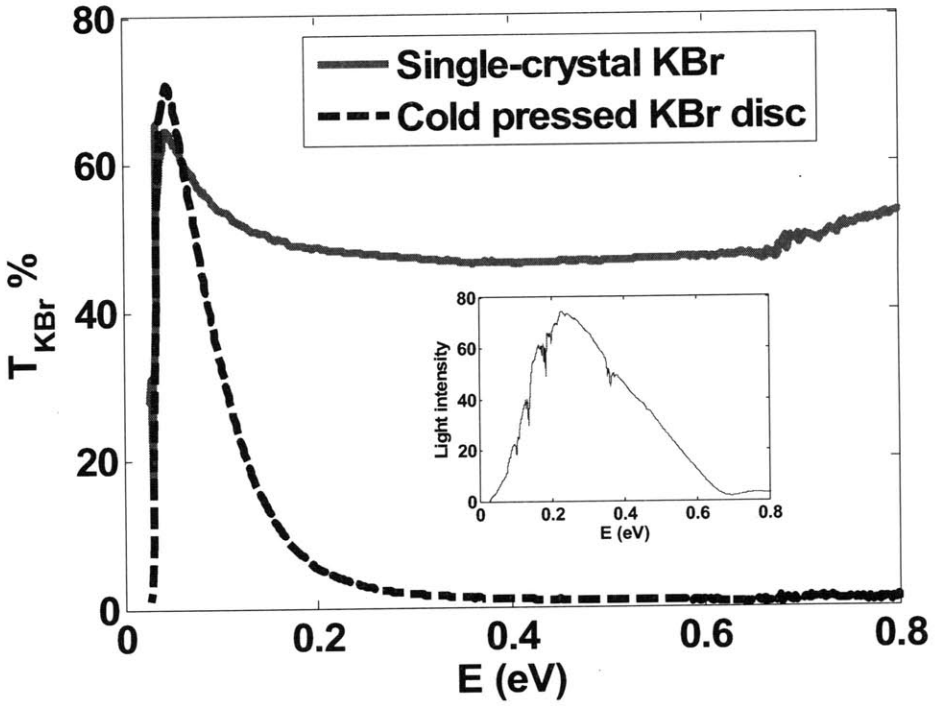

Figure 5.6 Transmissivity of a typical single-crystal KBr slice, compared with that for a cold pressed KBr disc. The transmissivity fluctuations above 0.6 eV can be attributed to the increased inaccuracies of our FTIR system because its light source intensity (see the inset) becomes very weak above 0.6 eV.

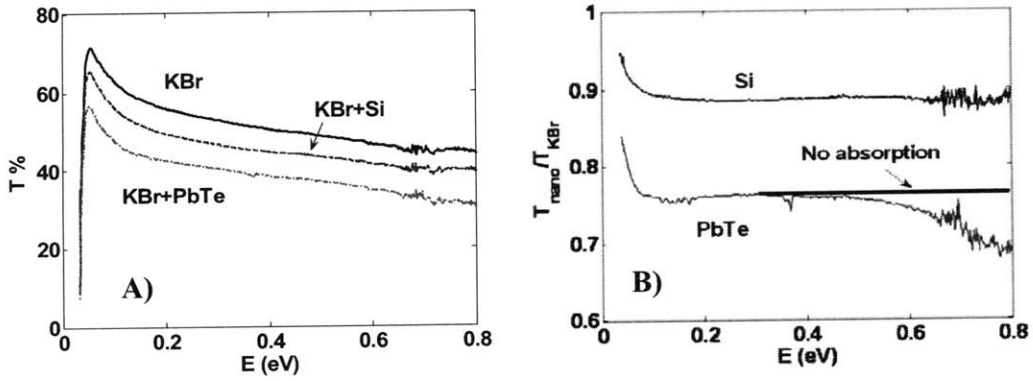

Figure 5.7 A) Transmissivity of a KBr slice with/without nanopowders. With PbTe nanopowder, the transmissivity decays slightly faster for E > 0.4 eV. B) Ratio between KBr transmissivity with/without nanopowders in Fig. 5.7A. Due to light absorption above their bandgaps (0.31 eV for PbTe [19]), PbTe nanopowders would further reduce the transmissivity in addition to the reduction caused by their scatterings, marked by the straight line here.

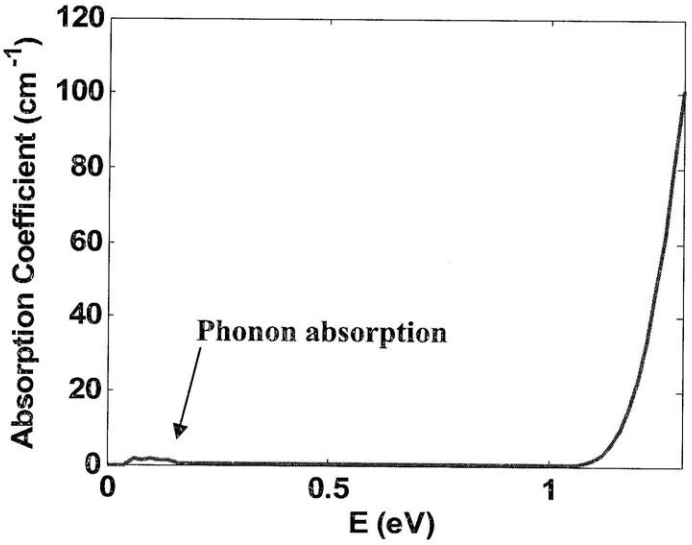

Figure 5.8 Absorption coefficient of bulk Si [47]. In the energy range from 0.04 to 0.2 eV, light is absorbed by phonons inside Si.

For light passing through a thin film, its intensity is reduced by a factor of $\exp(\alpha t)$ [43,48], in which α is the absorption coefficient of the film, t is the film thickness. Here the influence of transmission/reflection on the back and front surfaces of the film is neglected. For a layer of nanoparticles, its absorption can be approximated as that for a thin film, with thickness t replaced by an averaged particle diameter d. For $d \to 0$, the additional light intensity reduction by the particle layer absorption is simply $1-\exp(-\alpha d) \approx \alpha d$. Based on this simplification, the pattern of α can be found by subtracting the calculated PbTe transmissivity ratio in Fig. 5.7B from the value without absorption (straight line in Fig. 5.7B). Figure 5.9 shows the extracted absorption patterns from two independent tests, where PbTe absorption always occurs at around 0.3 eV. In the literature, the band gap of PbTe at 300 K is 0.31 eV [19], which is consistent with the results in Fig. 5.9. The absorption below the bandgap can be attributed to charge carrier absorption that decays with increased photon energy, as interpreted by the classical Drude model [49].

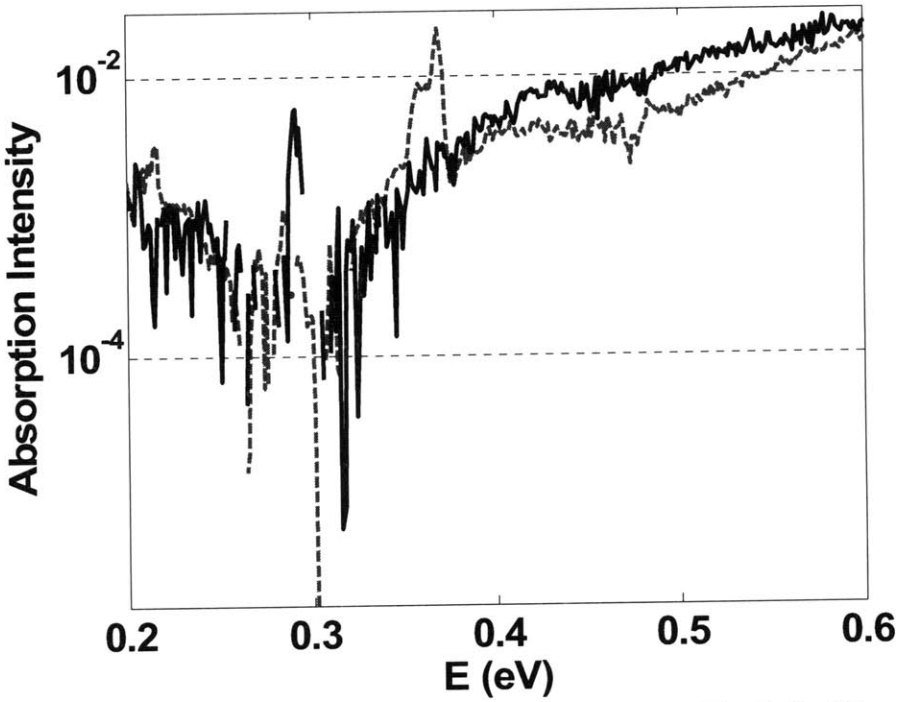

Figure 5.9 Absorption pattern extracted for PbTe nanopowder. The dashed line is for the test in Fig. 5.7B. The solid line is extracted from a separated test with another KBr slice.

Despite the noise in this simple measurement (Fig. 5.9), the bandgap thus determined agrees reasonably well with the literature value. With even smaller grain sizes, our measurements can be more sensitive to particle absorption rather than to the particle scattering. Compared to measurements using cold pressed discs, much less nanopowder is required for our simpler method and the additional step of cold press is also eliminated. This FTIR technique can be used as a general approach to quickly check the bandgaps of various TE nanopowders.

5.3 References

1 B. Poudel, Q. Hao, Y. Ma, Y. C. Lan, A. Minnich, B. Yu, X. Yan, D. Z. Wang, A. Muto, D. Vashaee, X. Y. Chen, J. M. Liu, M. S. Dresselhaus, G. Chen, and Z. F. Ren, *Science* **320**, 634 (2008).

2 A. Minnich, H. Lee, X. W. Wang, G. Joshi, M. S. Dresselhaus, Z. F. Ren, G. Chen, and D. Vashaee, *Phys. Rev. B* **80**, 155327 (2009).

3 C. R. M. Grovenor, *J. Phys. C: Solid State Phys.* **18**, 4079 (1985).

4 J. R. MacDonald, Ed. *Impedance Spectroscopy, Emphasizing Solid Materials and Systems* (John Wiley & Sons, New York, 1987).

[5] M. H. Abdullah and A. N. Yusoff, *J. Mater. Sci.* **32**, 5817 (1997).
[6] S. Upadhyay, D. Kumar, and O. Parkash, *Bull. Mater. Sci.* **19**, 513 (1996).
[7] G. H. Seager, G. E. Pike, *Appl. Phys. Lett.* **35**, 709 (1979).
[8] G. H. Seager, G. E. Pike, *Appl. Phys. Lett.* **37**, 747 (1980).
[9] W. E. Taylor, N. H. Odell, and H. Y. Fan, *Phys. Rev. B* **88**, 867 (1952).
[10] G. E. Pike, *Phys. Rev. B* **30**, 795 (1984).
[11] C. H. Seager, G. E. Pike, and D. S. Ginley, *Phys. Rev. Lett.* **43**, 532 (1979).
[12] D.V. Lang, *J. of Appl. Phys.* **45**, 3023 (1974).
[13] G. Blatter, and F. Greuter, *Phys. Rev. B* **33**, 3952 (1986).
[14] G. Petermann, *Phys. Status. Solidi (A)* **106**, 535 (1988).
[15] S. M. Sze, *Physics of Semiconductor Devices* (John Wiley & Sons Inc., New York, 1981).
[16] Jesus A. del Alamo, *Integrated Microelectronic Devices: Physics and Modeling* (Prentice Hall, New Jersey, 2009).
[17] Jin Au Kong, *Electromagnetic Wave Theory* (EMW Publishing, MA, 2005).
[18] T. V. Dijk and A. J. Burggraaf, *Phys. Status. Solidi (A)* **63**, 229 (1981).
[19] H. Preier, *Appl. Phys.* **20**, 189 (1979).
[20] W. Tennant, *Solid-State Comm.* **20**, 613 (1976).
[21] M. H. Frey, Z. Xu, P. Han, D. A. Payne, *Ferroelectrics* **206**, 337 (1998).
[22] H. J. Goldsmid, *Thermoelectric Refrigeration* (Plenum, New York, 1964).
[23] D. J. Singh and W. E. Pickett, *Phys. Rev. B* **50**, 11235 (1994).
[24] J. O. Sofo and G. D. Mahan, *Phys. Rev. B* **58**, 15620 (1998).
[25] K. Koga, K. Akai, K. Oshiro, and M. Matsuura, *Phys. Rev. B* **71**, 155119 (2005).
[26] E. Z. Kurmaev, A. Moewes, I. R. Shein, L. D. Finkelstein1, A. L. Ivanovskii, and H. Anno, *J. Phys.: Condens. Matter* **16**, 979 (2004).
[27] G. S. Nolas, G. A. Slack, T. Caillat and G. P. Meisner, *J. Appl. Phys.* **79**, 2622 (1996).
[28] E. Arushanov, M. Respaud, H. Rakoto, J. M. Broto and T. Caillat, *Phys. Rev. B* **61**, 4672 (2000).
[29] D. Mandrus, A. Migliori, T. W. Darling, M. F. Hundley, E. J. Peterson, and J. D. Thompson, *Phys. Rev. B* **52**, 4926 (1995).
[30] J. W. Sharp, E. C. Jones, R. K. Williams, P. M. Martin, and B. C. Sales, *J. Appl. Phys.* **78**, 1013 (1995).
[31] K. Matsubara, T. Iyanaga, T. Tsubouchi, K. Kishimoto, and T. Koyanagi, in *13th International Conference on Thermoelectrics*, edited by B. Mathiprakasm and P. Heenan, AIP Conf. Proc. No. 316 (AIP, New York, 1995).
[32] L. D. Dudkin and N. K. Abrikosov, *Fiz. Tverd Tela (Leningrad)* **1**, 31 (1959) [*Sov. Phys. Solid State* **1**, 29 (1956)].
[33] T. Caillat, A. Borshchevsky, and J.-P. Fleurial, *J. Appl. Phys.* **80**, 4442 (1996).
[34] P. Ghosez, M. Veithen, *J. Phys.: Condens. Matter* **19**, 096002 (2007).
[35] Z. G. Mei, J. Yang, Y. Z. Pei, W. Zhang, L. D. Chen, and J. Yang, *Phys. Rev. B* **77**, 045202 (2008).
[36] J. Yang, L. Xi, W. Zhang, L. D. Chen, and J. H. Yang, *J. Electron. Mater.* **38**, 1397 (2009).
[37] L. Bertini and C. Gatti, *J. Chem. Phys.* **121**, 8983 (2004).

[38] Valerio Lucarini, *Kramers-Kronig relations in optical materials research* (Springer, New York, 2005).
[39] K. V. Narasimham, J. C. Joshi, K. N. Chopra, C. Jagadish, and A. L. Dawar, *Infrared Phys.* **23**, 349 (1983).
[40] D. Patidar, K. S. Rathore, N. S. Saxena, Kananbala Sharma, T. P. Sharma, *Chalcogenide Lett.* **5**, 21 (2008).
[41] Shaji Varghese, Mercy Iype, E. J. Mathew and C. S. Menon, *Mater. Lett.* **56**, 1078 (2002).
[42] X. Li, and I. S. Nandhakumar, *Electrochem. Commun.* **10**, 363 (2008).
[43] M. F. Modest, *Radiative Heat Transfer, 2nd edition* (Elsevier Science, California, 2003).
[44] K. E. Stine, *Bechman Infrared Laboratory Manual*, Bechman Instruments Inc., Fullerton, California (1975).
[45] H.-D. Wu, S.-C. Wu, I-D. Wu and F.-C. Chang, *Polymer* **42**, 4719 (2001).
[46] K. H. Kim, C. H. Ho, T.-G. Suh, S. Prakash, and R.F. Bunshah, *J. Mater. Eng.* **13**, 199 (1991).
[47] D. E. Aspens, Chap. 2 in *Properties of Silicon* (INSPEC, IEE, London, UK, 1988).
[48] G. Chen, *Nanoscale Energy Transport and Conversion: A Parallel Treatment of Electrons, Molecules, Phonons, and Photons* (Oxford University Press, New York, 2005).
[49] P. Drude, *Annalen der Physik* **39**, 530 (1890).

Chapter 6. Future Research Directions

Different from previous chapters, this chapter covers additional topics that are related to my current thermoelectric (TE) research. Continued work on these topics can be important for the future development of TE nanocomposites.

6.1 Annealing Effects on ZT of PbTe nanocomposites

One important topic of material science research is to improve materials properties by post processes such as annealing. Unrestricted to BiSbTe nanocomposites as discussed in Chap. 2, annealing effects were also investigated for other TE nanocomposites mainly to improve their thermal stabilities at high temperatures. In previously investigated PbTe, PbSe, and $(PbTe)_x/(PbSe)_{1-x}$ nanocomposites, we found that carrier concentrations were significantly reduced by baking them for hours above 200 °C. Correspondingly, afterwards the room-temperature electrical conductivities can be decreased by a factor of 2-4 and Seebeck coefficients are increased (Fig. 6.1). Such changes may be attributed to carrier concentration reduction caused by grain interface trapping of charge carriers at elevated temperatures, but more investigations are required to confirm this.

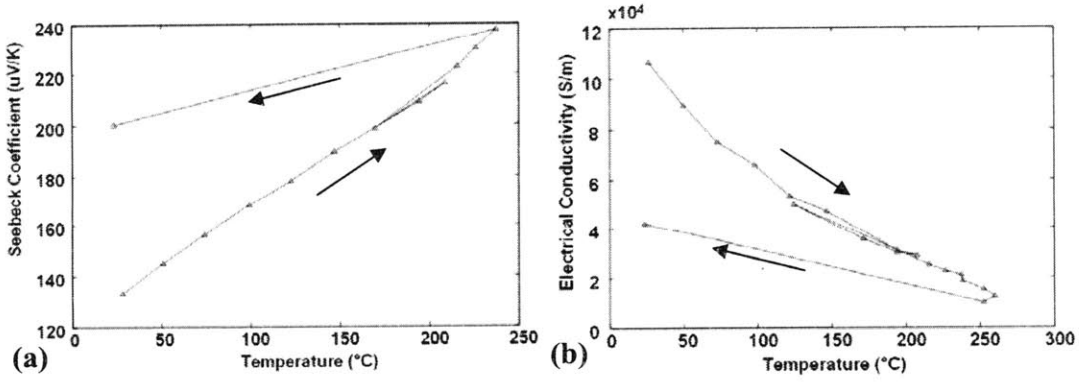

Figure 6.1 Property change of a typical PbSe nanocomposite during high-temperature measurements. The sample stayed at each measurement point for 30 minutes. The time history is indicated by the arrows.

For $CoSb_3$-based nanocomposites, we also found that sample properties may still change during high-temperature measurements. To avoid this, in practice we usually

anneal samples above 500 °C after hot press till their properties saturate at such temperatures.

6.2 N-type Bi_2Te_3-Based Nanocomposites

Despite the high ZT obtained in p-type $Bi_{0.4}Sb_{1.6}Te_3$ nanocomposites, little processing has been made in their n-type counterpart. In bulk Bi_2Te_3-based TE materials, the most widely used composition for n-type samples is $Bi_2Te_{3-y}Se_y$ ($0<y<0.3$) [1,2]. However, the mechanical deformation caused by ball milling introduces many Te vacancies [3] (donors in Bi_2Te_3) that always over-dope n-type nanocomposites, resulting in a much lower power factor than that for an optimized carrier concentration. To check the influence of ball milling, we prepared pure Bi_2Te_3 nanocomposites from elemental chunks, and they were all n-type instead of p-type for bulk Bi_2Te_3. It was clear that ball milling could introduce extra donors into a Bi_2Te_3-based nanocomposite and to even change its type, similar to the function of oxidation in Bi_2Te_3. In comparison, pure Sb_2Te_3 nanocomposites from element chunks were always p-type as expected. The influence of ball milling was weak in our p-type BiSbTe nanocomposites because they were predominantly Sb_2Te_3 in composition. However, it became important for a typical n-type nanocomposite with over 90% Bi_2Te_3 in its composition.

Two issues should be addressed for Te vacancies in n-type nanocomposites. First, we need to understand how they scatter electrons and phonons and thus affect transport properties. More importantly, we should investigate methods to annihilate them, possibly by post annealing or composition adjustment. On the other hand, we can focus on how to further reduce the lattice thermal conductivities by either restricting the grain growth or creating nano-sized pores inside the material. In addition to further shortening the hot press period and using fast cooling after the hot press, the former one can also be achieved by coating nanoparticles with a non-diffusive material before hot press. The latter one was suggested in the literature [4,5] but we should be cautious about possible deterioration in the electrical conductivity due to disordered pores. Such pores can be created by adding evaporative elements into nanocomposites and annealing them after hot press to remove residual evaporative elements.

For a TE device, the averaged $\langle Z \rangle$ in Eq. (3-3) of Chap. 2 is mainly limited by the leg with a lower Z value [2]. Currently, the peak ZT of our best n-type nanocomposites is close to 1.0, which is comparable to state-of-art commercial ingots. To make full use of the ~1.4 peak ZT of our p-type nanocomposite, an n leg with a compatible high ZT is always preferred and more efforts should be dedicated to the development of n-type nanocomposites with superior performance.

6.3 Nanocomposites for Low Temperature Applications

Another important aspect of Bi_2Te_3-based nanocomposites is for low-temperature applications (T<300 K). Because phonons in a bulk sample have longer MFPs at lower temperatures, the grain boundary scattering of phonons is expected to be more important than that above 300 K. And we expect more apparent thermal conductivity reduction in nanocomposites compared with their bulk counterpart materials. Remarkable ZT enhancements are expected if the electrical properties can be maintained. Combined with high-temperature measurements, low-temperature studies could also benefit our physical understanding of various scattering mechanisms of charge carriers. For instance, impurity scattering of charge carriers becomes important at cryogenic temperatures, while acoustic deformation potential scattering is normally the dominant mechanism above room temperature. Theoretical studies across the whole temperature range will help us to better understand the phonon and electron transport inside nanocomposites.

For low-temperature TE samples, $Bi_{2-x}Sb_xTe_3$ ($x<0.5$ here, in contrast with $x>1.5$ for p-type samples) [6] or more complicated compositions, such as $Bi_{1.8}Sb_{0.2}Te_{2.85}Se_{0.15}$ doped with SbI_3 [7], were recommended in addition to $Bi_2Te_{3-y}Se_y$ ($0<y<0.3$). For even lower temperatures, Bi_xSb_{1-x} alloys are widely used [2]. Some future research may be carried out on nanocomposites with these compositions.

6.4 Single Grain Interface Impedance Measurements

Although reasonable results were obtained in the impedance measurements on a bulk PbTe sample in Chap. 5, the data analysis was very coarse in that the nanocomposite structure was simplified as packed identical cubes. In reality, the grain sizes may be

distributed over a wide range and their shapes may also significantly vary inside a nanocomposite [8]. Ideally, we should conduct ac impedance spectroscopy measurements across a single grain interface so that we have much less uncertainties in our analysis.

For a bulk sample, we always find that the self-inductance impedance, $i\omega L_s$, can overshadow interface capacitance signals at the high frequencies required for $C(\omega)$ saturation. Therefore, we explored the possibility of measuring high-resistance thin film samples so that the self-inductance signals could become less important. Figure 6.2 presents a schematic diagram of this experimental setup. A bridge region is fabricated in the middle part of the film by ion beam milling and cutting. The width and thickness of the bridge can be controlled to be comparable to the averaged grain size. By loading the traveling voltage probes right across a grain interface along the bridge, we can conduct dc measurements to find the grain-boundary electrical resistance [9] and ac measurements of its impedance [10]. The interface capacitance can then be completely determined from these results. For dc measurements, voltage probes can also be loaded inside a grain to measure the in-grain resistance R_{gi}. This is important for us to distinguish the resistivity contributions from grain interfaces and grain interior parts. Figure 6.3 shows a scanning electron microscope (SEM) image of a suspended thin film sample with a bridge region in its middle, prepared by Dr. Yucheng Lan at Boston College. Both ends of the sample were fixed onto a Cu grid by electrically nonconductive glue to avoid any shortage. For this test, a $Yb_xCo_4Sb_{12}$ nanocomposite sample with grain sizes ~1 μm was used. The bridge cross section had a dimension around 2 μm (inset of Fig. 6.3) so that we could measure the electron transport across one or a few grains.

Our measurements were conducted under a SEM equipped with four movable electrical probes (Figs. 6.4A, B). However, it was later realized that the electrical contact between the probes and the tested sample could result in unexpected noise detrimental to the proposed measurements. To improve these contacts, we tried to increase the loading force of the probes but the thin-film sample was always damaged even with an underneath supporting substrate. Other attempts of patterning metal lines onto a thin-film sample as electrical probes [10] also encountered the same contact problem, resulting in

very noisy signals. This may be attributed to possible oxidation on the thin film surface and for this reason better surface cleaning before metal deposition is required.

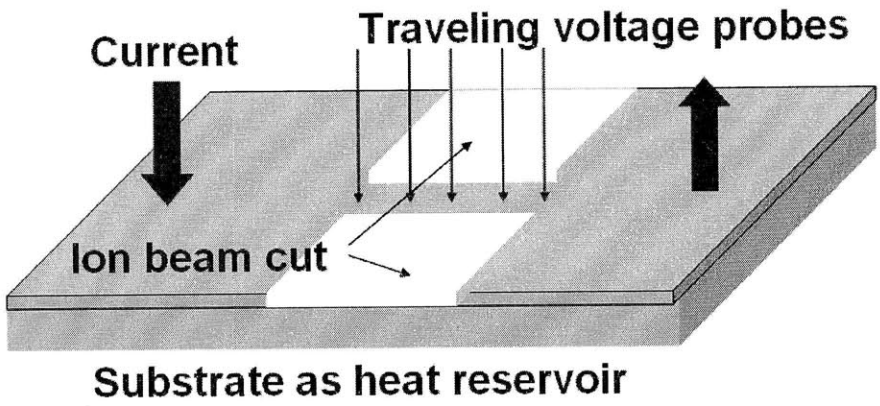

Figure 6.2 Schematic diagram of a traveling voltage probe setup to measure the capacitance and resistance across a single grain interface. In the middle of a thin-film sample, a bridge region with its cross-section dimension comparable to the grain sizes is fabricated by cutting off the blank region with ion beams.

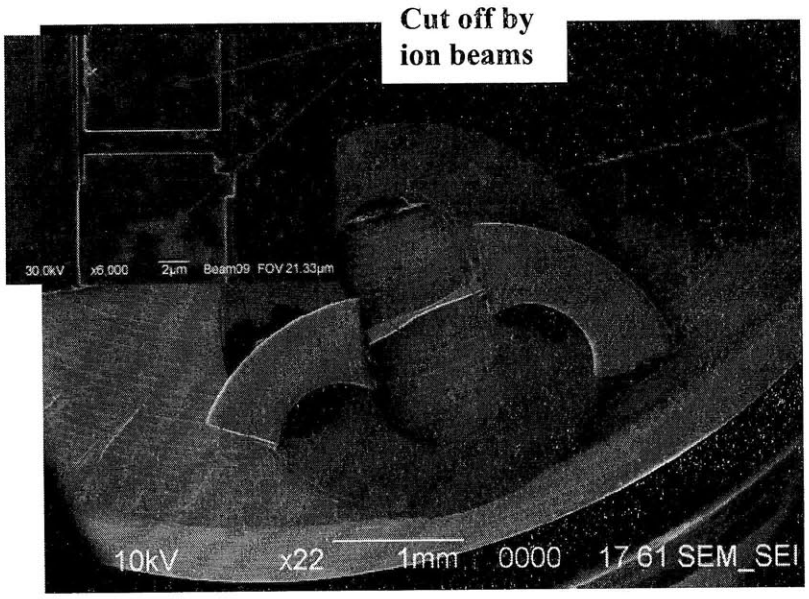

Figure 6.3 An SEM image of the real setup. With ion beams, the middle part of the sample (inset) was first milled down to a few micrometers and then a bridge region was fabricated by removing the material on both sides of the bridge.

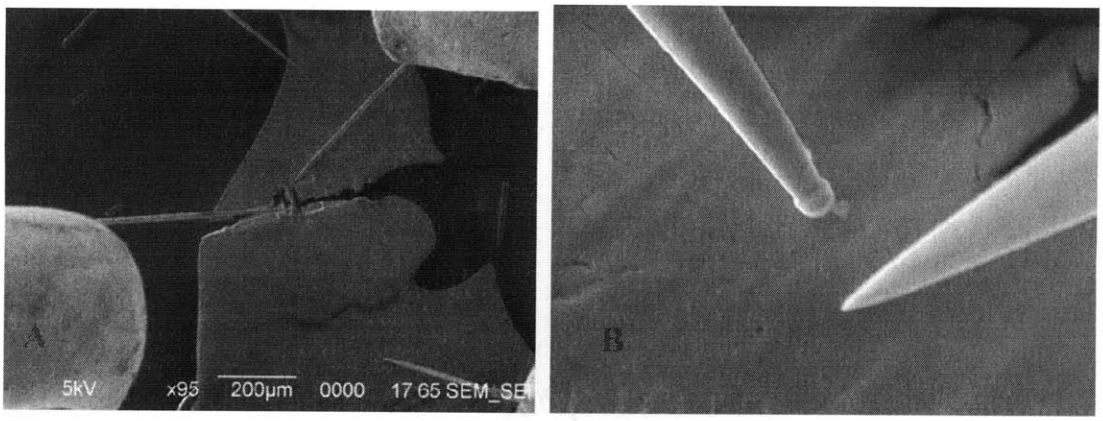

Figure 6.4 A) Four-probe electrical measurements under a SEM. Two voltage probes are loaded right across a bridge region. In ac measurements, periodic Peltier heating/cooling and Joule heating will occur at the current injection locations. Such temperature variations may introduce an additional ac Seebeck voltage across the sample. To avoid its influence on voltage measurements, the current probes were located away from voltage measurement region by ~400 µm. This distance is at least one magnitude longer than the length scale of ac temperature oscillations, $\sqrt{\alpha / f}$, with α as the sample thermal diffusivity and f as the used ac frequency. B) Two tungsten probes loaded onto a sample under a SEM. The radius of the probe tip is ~10 nm.

6.5 Electrostatic Force Spectroscopy

For $CoSb_3$-based nanocomposites with relatively large grain sizes (200 nm-1 µm), it is also possible to employ Electrostatic Force Spectroscopy (EFS) based on an Atomic Force Microscope (AFM) to measure the trapped charges on a single interface [11]. In this case, the local static charge of the scanned surface is related to the electrostatic force between the probe tip and the surface (Fig. 6.5). I collaborated with Dr. Shuo Chen at MIT in this effort. In all measurements, the sample topography is first scanned by an AFM and then the local electrostatic field is mapped with a dc bias applied between the sample and the AFM tip. The contrast between the two will give us information on the surface charge distribution. However, in practice the sample surface roughness needs to be controlled to be less than 1 nm to observe such a contrast. This is difficult to be achieved by either chemical-mechanical polishing or focused ion beam cutting/polishing. In addition, the possible contamination layer on the sample surface after polishing may also weaken the electrostatic force signals. In the preliminary tests, no grain interfaces

could be identified from the contrast between two scanning images. Better surface polishing and cleaning is critical for this study in the future.

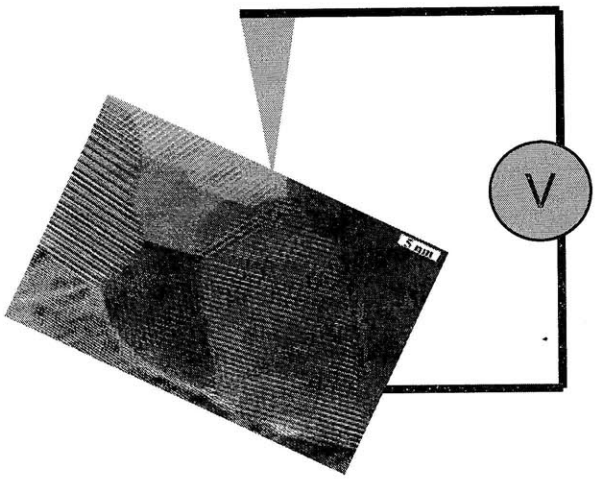

Figure 6.5 Concept of the Electrostatic Force Spectroscopy (EFS) measurement. The scan is performed with/without a dc bias between the tip and the sample. The contrast between the two gives the distribution of interface trap charges.

6.6 Other Recommended Research Directions

In addition to above topics, a few other research directions may also be pursued in the future. Combination between fundamental theories and experimental studies are required for the advancement of these topics:

1) Mechanical Properties of TE Nanocomposites

Over the years, tremendous efforts were dedicated to the superior mechanical properties of various nanocomposites [12-14]. Lattice mismatch between nanoparticles generates residual stresses inside nanocomposites. Combined with the large interface density, defined as interface area per unit volume, the resulting mechanical properties of nanocomposites are expected to be dramatically different from their bulk counterparts. For TE materials, good mechanical properties can be crucial for device fabrication and operation. In this aspect, TE nanocomposites not only provide a higher ZT but also have advantages in manufacture. The improved mechanical properties were repeatedly observed from our experience of cutting TE legs. Compared with a start-of-the-art ingot,

BiSbTe nanocomposites generally possess better tolerance for mechanical damage and are less likely to be broken. In the future, tests on the hardness, thermal expansion, and other mechanical properties should be conducted for nanocomposites, which can also be useful for device design purpose.

2) Phonon Transport across a Grain Interface

For nanocomposites, the Monte Carlo simulation technique enables us to investigate the thermal conductivity spectrum and phonon transmission/reflection spectrum across a grain interface. This provides important guidance for phonon engineering that employs different mechanisms to effectively scatter phonons in particular frequency ranges. The interface thermal resistance can be estimated to compare with measurements using heat pulse propagation across an interface, similar to the work on a bonded silicon wafer [15]. The modeling can also be further related to detailed interface conditions obtained by advanced tools, such as micro-Raman spectroscopy and electron microscopy. Impurities trapped on interfaces, inter-grain diffusion, and grain growth during hot pressing should be well addressed to obtain small grains with large interface thermal resistance. Some of these may also be explored theoretically by methods such as molecular dynamics simulations. In the long term, these interface studies can also incorporate the influence of nanoscale mechanical stresses determined by some advanced techniques [16,17].

3) Thermal Insulation Material

Advanced thermal insulation materials play an important role in thermal energy conservation for buildings, heat storage tanks, and other large-scale systems. Unrestricted to thermoelectrics, nanocomposites are promising candidates for a wide range of applications, including thermal insulation materials with superior mechanical strength. Improvement can be achieved by further reducing grain sizes and modifying grain interfaces. With evaporative elements embedded in nanocomposites, we are also able to create nano- and micro-pores inside samples by high temperature annealing. The thermal conductivities of nanocomposites can be further decreased with these additional pores.

6.7 References

[1] D. M. Rowe, Ed. *CRC Handbook of Thermoelectrics* (CRC, Boca Raton, FL, 1995).

[2] H. J. Goldsmid, *Thermoelectric Refrigeration* (Plenum, New York, 1964).

[3] J.M. Schultz, J.P. McHugh, and W.A. Tiller, *J. Appl. Phys.* **32**, 2443 (1962).

[4] Q. Y. He, S. J. Hu, X. G. Tang, Y. C. Lan, J. Yang, X. W. Wang, Z. F. Ren, Q. Hao, and G. Chen, *Appl. Phys. Lett.* **93**, 042108 (2008).

[5] J.-H. Lee, J. C. Grossman, J. Reed, and G. Galli, *Appl. Phys. Lett.* **91**, 223110 (2007).

[6] B. M. Gol'tsman, V. A. Kudinov, and I. A. Smirnov, *Semiconductor Thermoelectric Bi_2Te_3-based Materials* (Nauka, Moscow, 1972).

[7] W. M. Yim, F..D Rosi, *Solid State Electron.* **15**, 1121 (1972).

[8] B. Poudel, Q. Hao, Y. Ma, Y. C. Lan, A. Minnich, B. Yu, X. Yan, D. Z. Wang, A. Muto, D. Vashaee, X. Y. Chen, J. M. Liu, M. S. Dresselhaus, G. Chen, and Z. F. Ren, *Science* **320**, 634 (2008).

[9] G. H. Seager, T. G. Castner, *J. Appl. Phys.* **49**, 3879 (1978).

[10] R. P. Rodrigues, J.-H. Hwang, and V. P. Dravid, *J. Electroceram* **3**, 245 (1999).

[11] D. Gekhtman, Z. B. Zhang, D. Adderton, M. S. Dresselhaus, and G. Dresselhaus, *Phys. Rev. Lett.* **82**, 3887 (1999).

[12] K.Niihara, *J. Ceram. Soc. Jpn.* **99**, 974 (1991).

[13] H.Gleiter, *Acta Metall. Sin.* **33**, 165 (1997).

[14] H. L. Tan and W. Yang, *Mech. Mater.* **30**, 111 (1998).

[15] Y. Ohsone, G. Wu, J. Dryden, F. Zok, and A. Majumdar, *J. Heat Transfer* **121**, 954 (1999).

[16] R. Hillenbrand, T. Taubner, and F. Keilmann, *Nature* **418**, 159–162 (2002).

[17] A. J. Huber, A. Ziegler, T. Köck, and R. Hillenbrand, *Nature Nanotech.* **4**, 153-157 (2008).